

A Critical Fast Ion Beta in the Madison Symmetric Torus
Reversed Field Pinch

by
William J. Capecchi

Dissertation submitted in partial fulfillment of
the requirements for the degree of

Doctor of Philosophy
(Physics)

at the
UNIVERSITY OF WISCONSIN-MADISON
2017

Date of final oral examination: 10/18/2016

The dissertation is approved by the following members of the Final Oral Committee:

John S. Sarff, Professor, Physics

Jay K. Anderson, Senior Scientist, Physics

David T. Anderson, Professor, Electrical & Computer Engineering

Jan Egedal, Associate Professor, Physics

Paul W. Terry, Professor, Physics

ABSTRACT

The first fast-ion profile measurements have been made in a reversed-field pinch (RFP) plasma. A large population of fast-ions are deposited in the core of the Madison Symmetric Torus (MST) through use of a 1 MW neutral beam injector (NBI) giving rise to a variety of beam-driven instabilities. One such mode, the energetic-particle mode (EPM) has been shown to reduce fast-ion content in MST, evident through drops in signal levels of the advanced neutral particle analyzer (ANPA).

EPs in MST appear as bursts of magnetic fluctuations at a lab frequency of ~ 100 kHz reaching peak amplitude and decaying away within $100 \mu\text{s}$. A burst ensemble of the neutron data does not reveal a drop in neutron emission across a burst, implying the population of fast-ions transported by a burst constitute a small fraction of the total. The burst may also pitch-angle scatter out of the ANPA phase space or be transported to mid-radius where charge-exchange with the background neutrals or fast-ion orbit stochasticity may reduce fast-ion confinement.

Data gathered from the expanded neutron diagnostic suite including a new collimated neutron detector (CiNDe) was used to reconstruct the fast-ion profile in MST and measure critical β_f quantities. Measurements were made in plasma conditions with varying magnetic field strength in order to investigate the interplay between the energetic particle (EP) drive and Alfvén continuum damping. The measured values of $\beta_f(0)$ (7.5% (1.2%) in 300 (500) kA plasmas) are reduced from classical predictions (TRANSP predicts up to 10% core value) due to EPM activity. The frequency, magnitude, and rate of occurrence of the bursts depends on the tearing mode amplitude, Alfvén continuum damping rate, fast-ion profile shape, and resonant orbit dynamics.

Marginal stability was reached in both moderate- (300 kA) and high- (500 kA) current discharges, marked by sustained EPM activity and a saturated global neutron signal during NBI. The difference in profile shape is interpreted to be related to the core-most resonant tearing mode amplitude, as a larger core magnetic island moves the location of steepest

fast-ion gradient further out in radius, resulting in lower confinement of the fast-ions. The reconstructed profile is more strongly peaked at lower current, consistent with a lower measured core-most tearing mode amplitude. A larger dataset at lower current gives enough temporal resolution to investigate the evolution of the fast-ion profile. The suppression of the core-most tearing mode amplitude during NBI results in a rapid and dynamically evolving fast-ion profile at the beginning of the NBI discharge and results in an initially broader profile early evolving into a more strongly peaked profile later in the NBI discharge.

Acknowledgments

“I find it elevating and exhilarating to discover that we live in a universe that permits the evolution of molecular machines as intricate and subtle as we.”

—Carl Sagan

Considerably less time would be needed to name the people I’ve met in my life to whom I do not owe a debt of gratitude for helping me complete this work. I have been lucky in life to have been surrounded by so many loving and supportive people.

First, thanks to Jay Anderson. I’ve learned so much during my time in Madison, due in no small part to your endless patience. Thanks for always having an open door. Thanks to John Sarff, Liang Lin, and Mark Nornberg for their input and expertise, and to the rest of the MST group for their interest and support of my work. Thanks to Bill Zimmerman and Peter Weix, without whom CiNDe would never have been completed.

Thanks to Jon Koliner, Eli Parke, Scott Eilerman, and Rich Magee. You all had a hand in laying the foundation upon which this work is built and were more than happy to help me along my way.

Thanks to the energetic particle group; Jung-ha Kim, Phillip Bonofiglio, Stephanie Sears, and John Boguski. You of all people had to put up with my day-to-day tribulations, and were always ready to offer helpful suggestions.

Thanks to Francesco Volpe, Ken Hammond, and Scott Massida. I am very grateful for having the chance to pursue another research project (and explore another city). My time working with all of you was stimulating and (I hope) fruitful.

To my officemates over the years, thank you for the interesting though often seemingly random conversation. These much needed breaks from my work helped to remind me of the love I have for science even as I sweat over a piece of broken code.

To Dan Carmody, Pete Froehling, Guilhem Ribeill, Zach Simmons, Zack DeLand, Martin Lichtman, and all the rest of wisphysgrad09; my grad school career will always remain one of the best times of my life thanks to the good friends I’ve made here. Thanks for all the amazing memories.

Thanks to Jon Latner, Emily Atkinson, and Spencer Pforsich; I always looked forward to our lunch conversations.

A special thanks to all of you who took care of me on my countrywide Amtrak thesis-writing tour- Jim, Sue, Ada, Anne, Colin, Josie, (Fergus!), Carmody, Bob, Danielle, Dan, Katie, Luca, Elliot, and Peter! That was an amazing adventure and a great way to get this writing off the ground.

A special thanks also to Tim, Jessica, Sue, Randy, Landon, and Miles. I feel truly welcomed by you all. Thanks for going out of your way to support me (and feed and house me) as I finish my dissertation.

To my own family; Thank you to Natalie, Oliver, Leah, and Wesley for bringing joy to my life. Hanging out and playing games with you four is more fun than any uncle could ask for. Thanks to my loving sisters Carrie and Jennie and my brothers-in-law Zack and Steve. Your love and support has been an enormous help to me during grad school and throughout the years. Mom and dad- thank you. My entire life has been filled with love and happiness thanks to your endless encouragement, trust, and support. There is no end to how grateful I am to all you have given to me over the years. Thank you, thank you, thank you.

To my fiancée Stephanie Payne, **thank you**. Your love and support is more than I deserve. I love you, and I'm filled with joy at the prospect of our life together, and many more "mountaintops and autumn forest paths." Thank you for everything.

TABLE OF CONTENTS

<i>Abstract</i>	i
<i>Acknowledgements</i>	iii
<i>Table of Contents</i>	v
<i>List of Tables</i>	vii
<i>List of Figures</i>	viii
1. Background	1
1.1 The Energy Crisis	1
1.2 The Green Movement and Renewable Energies	5
1.3 The Fusion Solution	6
2. Introduction	9
2.1 Outline	9
2.2 MST and Standard Diagnostics	10
2.2.1 The Madison Symmetric Torus	10
2.2.2 Advanced Neutral Particle Analyzer and D-Alpha Array	13
2.3 The MST Neutral Beam Injector	15
2.4 The Alfvén Continuum, Gap Modes, and EPMS	17
2.5 A Short History of EPMS	22
2.6 Summary of key results of thesis	26
3. Neutron Detection	27
3.1 D-D Fusion	28
3.2 Neutron Detection Techniques	29
3.2.1 Scintillation Detectors	30
3.3 MST Global Neutron Diagnostics	30
3.3.1 Detector Specifications	31
3.3.2 Global Neutron Detector Calibrations	33
3.3.3 Summary of Scintillator-Based Neutron Detectors	37
3.4 Collimated Neutron Detector (CiNDe)	37
3.4.1 Modeling	39
3.4.2 Detector Design	41
3.4.3 Pulse Identification	45

4. <i>Fast Ion Dynamics in MST</i>	49
4.1 Magnetic stochasticity and thermal confinement	49
4.2 Fast-ion confinement	50
4.3 Fast-ion q	54
4.4 EPM Growth Conditions	59
4.5 Evidence for EPM-limited fast-ion beta	62
4.6 Summary	63
5. <i>Fast Ion Beta Measurements in MST</i>	65
5.1 Experimental Data	65
5.2 Data Inversion Method	68
5.3 Fast-ion Profiles	80
6. <i>Conclusion</i>	90
6.1 Summary	90
6.2 Future Work	91
6.2.1 Fusion Proton Detector	91
6.2.2 Pulse Shape Discrimination	92
6.2.3 NBI Fueling Mixture	93
6.2.4 Investigation of Mode Structure	93
<i>Appendix</i>	100

LIST OF TABLES

2.1	MST Parameters	11
2.2	NBI Parameters	17
3.1	Neutron and gamma mean-free-paths through materials at 2.45 MeV	41
5.1	Dataset parameters	66
5.2	Chord geometries	67
5.3	Profile gradients	84

LIST OF FIGURES

1.1	World energy consumption broken down by type, showing the drastic rise in production from the Industrial Revolution to present day [1]	2
1.2	IPCC report graphic showing global trends in temperature anomalies, surface temperature, sea ice extent and sea level change, and land precipitation . . .	4
1.3	Per capita energy consumption has drastically increased as our societies have become more technologically advanced	4
1.4	Average binding energy per nucleon vs. atomic number	7
2.1	The RFP magnetic topology. A toroidal field of similar amplitude to the poloidal field reverses direction near the edge.	11
2.2	MST vacuum vessel and relevant diagnostics. NBI, CiNDe, ANPA, and global neutron detector locations are shown with appropriate injection/viewing geometries.	12
2.3	Typical MST discharge signals. (a) Plasma current and neutral beam power (b) Volume-averaged and edge-valued toroidal magnetic field (c) Line-averaged electron density (d) Core-most resonant tearing mode amplitude (d) Total MST neutron flux	12
2.4	Typical q profile for MST with magnetic island locations ($n = 5-15$) and approximate widths overlaid. Note high density of islands at larger radius. .	14
2.5	TRANSP modeling of beam deposition from MST's 1 MW neutral beam injector predicts a large core-localized population of high-pitch ions.	16
2.6	The tangential 1 MW neutral beam injector on MST produces a large population of core-localized high-pitch ions.	17
2.7	The $m = 0, 1$ $n = 5$ Alfvén continuum for MST equilibrium values computed from 300 kA $F = 0$ discharge. Coupling between the $m = 0, n = 5$ mode (dashed red) and $m = 1, n = 5$ mode (dashed blue) opens a gap in the continuum around $r \approx 32$ cm (black).	20
2.8	Spectrogram depicting typical $n = 5$ bursting modes. Strong $n = 5$ tearing mode activity is shown and represents a good approximation for the core rotation frequency.	25
3.1	Fusion reactivity rates for various fusion processes. The high velocity of MST beam ions relative to bulk means D-D reactivity is very sensitive to beam energy.	28
3.2	Absorption coefficient versus energy for Lead	32
3.3	The initial beam current ramp up (a) leads to an increasing number of fast-ions and fusion rate (b) in MST	34

3.4	Calibrations based on a beam-blip type method for (a) NLF using mixed fuel (5% deuterium) NBI discharges and for (b) NMF and NHF using full deuterium discharges.	35
3.5	NLF comparison to neutron ball. (a) integrated signal versus dose gives scaling, calculated for blue points to avoid saturated anode signal. (b) flattop averages indicate upper detector operating limit of 2.5 V	36
3.6	NMF and NHF integrated measurements versus neutron ball dose rates. Both detectors show good linear behavior over entire achievable MST flux range. .	37
3.7	CAD model of final design of collimated neutron detector (CiNDe). Three detachable stages (a) allows for easier movement around machine area. A 5.1 cm diameter and 92 cm bore (b) defines the plasma viewing volume which is scanned across the poloidal cross section of the machine by adjusting the inclination of the baseplate using a dual worm-screw jack system (c).	38
3.8	MCNP simulation showing neutron energy spectrum after PE slab transit versus slab thickness	40
3.9	Directional sensitivity versus scintillator dimensions. Dashed lines show lines of constant signal level	41
3.10	Neutron and gamma mean-free-paths versus energy for various materials. . .	42
3.11	Energy transfer ratio versus recoil scattering angle.	42
3.12	CiNDe: Exploded view of CAD model (left) and photo of diagnostic in place beneath MST (right).	44
3.13	Construction of the lowest stage of CiNDe. An array of HDPE cylinders provides the bulk of the shielding. The gaps between cylinders and walls were filled with paraffin wax. Inset: IR image following wax pour.	44
3.14	Gamma transmission through 5 cm MST vessel versus energy.	45
3.15	Exploded view of CiNDe's neutron detector stack. The PMT/Scintillator are situated within a stack of cylindrical lead bricks to reduce gamma signal levels and set atop a HDPE spacer to reduce neutron backscatter from the surrounding lab space. Cables are fed through the top of the stack and out below the removable CiNDe stages.	45
3.16	Raw CiNDe signal at various zoom levels. Large count rate as expected during NBI, but well below level where pulse pile-up is a concern.	46
4.1	Orbit topology in MST reveals low orbit loss and prevalence of co-passing NBI orbits.	51
4.2	Beam-blip experiment showing fast-ion confinement times of roughly 20 ms [2]	52
4.3	Beam-blip experiment with 1 MW NBI reveals near classical confinement of co-injected ions[3]	53
4.4	Modeling depicting $n = 5$ QSH state	53
4.5	Fast-ion confinement times plotted against the $n=5$ fluctuation amplitude showing degradation of fast-ion confinement to thermal levels in QSH plasma. Red points are for co-injected ions, blue for counter-injection	54
4.6	A simulated magnetic field line (black) and a fast-ion guiding center trajectory (red). Drift motion causes deviation from the field line while particle stays on flux surface	55

4.7	Typical q -profile showing the safety factor in black. The fast-ion q is also plotted for co-injection (red) and counter-injection (blue). Also noted are the locations of rational surfaces	56
4.8	q_f profiles for 25 keV DNBI into 300 and 500 kA plasmas. Smaller shift from q_{mag} due to stronger $ B $ at higher plasma current. Also shown the approximate fast-ion island widths overlap at mid-radius.	56
4.9	NBI beam center as viewed from above MST (left) and as a poloidal cross section (right). Beam injection entry and particle ionization location are shown.	58
4.10	Fast-ion orbits following co-, counter-, and perpendicular-injection from the same initial position. Velocities for co- and counter-injection are determined by NBI beam geometries.	59
4.11	(a) Landau (and Inverse) damping on a velocity distribution showing wave damping and (transient) wave drive. (b) Axially peaked EP distribution function results in wave drive due to gradient in the toroidal angular momentum.	60
4.12	Orbits modeled from various ionization sites along the NBI geometry (a) show resonance with a 60-80 kHz EPM around mid-radius (b). Scanning the EPM frequency and radial location results in “hot spots” of resonance (c) where net energy transferred to the wave grows in time (d).	62
4.13	Full deuterium beam shows EPM signal saturation. (a) 40, 30, and 20 A NBI into 300 kA plasmas results in (b) $n = 5$ EPM activity, with mode onset delayed at lower beam power. After onset of EPM activity, however, (c) neutron flux saturates, breaking with TRANSP predictions (dashed line). . .	64
5.1	Viewing chord geometries for 300 kA (left) and 500 kA (right) dataset. Blue lines depict CiNDe line-of-sight and gray sectors represent the extent of the viewing volume.	66
5.2	Data analysis for core-viewing chord (0 cm impact parameter) for 300 kA dataset. Comparing CiNDe count rate to global neutron rate (a) and core-most tearing mode amplitude (b). Burst times plotted in (c) are ensembled for CiNDe and global neutron data in (d).	68
5.3	Chord 1 (3.5 cm impact parameter) analysis for 300 kA dataset	69
5.4	Chord 2 (7 cm impact parameter) analysis for 300 kA dataset	69
5.5	Chord 3 (10.5 cm impact parameter) analysis for 300 kA dataset	70
5.6	Chord 4 (14 cm impact parameter) analysis for 300 kA dataset	70
5.7	Data analysis for core-viewing chord (0 cm impact parameter) for 500 kA dataset. Comparing CiNDe count rate to global neutron rate (a) and core-most tearing mode amplitude (b). Burst times plotted in (c) are ensembled for CiNDe and global neutron data in (d).	71
5.8	Chord 1 (5 cm impact parameter) analysis for 500 kA dataset	71
5.9	Chord 2 (10 cm impact parameter) analysis for 500 kA dataset	72
5.10	Chord 3 (15 cm impact parameter) analysis for 500 kA dataset	72
5.11	CiNDe pulse count rates for core-viewing chord and background for the 300 kA dataset. Both signals are normalized to their respective global neutron detector signals to account for slightly varying plasma conditions.	73

5.12	Net count rates for the five (four) chords for the 300 kA (500 kA) dataset. A clear reduction in neutron emissivity is seen with increasing distance from the core, becoming effectively zero at ~ 15 cm.	74
5.13	TRANSP average fast-ion energy vs time at four radii from $r = 0-0.2$ m shows near constancy with radius.	75
5.14	ANPA spectrogram for 300 and 500 kA datasets. Injection near 25 keV connects through a broad profile to the lower energy channels.	75
5.15	ANPA fast-ion energy distributions for 300 (black) and 500 kA (red) plasmas, and comparison to TRANSP modeling at 300 kA (blue).	75
5.16	Gaussian profile parameter optimization for the 300 kA dataset. A clear minimization exists in $y_0 - \sigma$ parameter space and results in good agreement between the predicted and experimentally measured count rates.	77
5.17	Three profile shapes considered to determine sensitivity of results.	78
5.18	Optimization for the 300 kA late dataset linear and flat profiles.	78
5.19	Comparison of the resulting β_f for the 300 kA late dataset following parameter optimization for the three tested profiles shown in Figure 5.17.	79
5.20	Gaussian profile parameter optimization for the 500 kA dataset.	79
5.21	300 kA Dataset averages of $n = 5$ EPM activity (a) and core-tearing activity (b). Optimization of profile parameters to match experimental values (c) results in n_f profiles shown in (d) early and late in the discharge.	81
5.22	500 kA Dataset averages of $n = 5$ EPM activity (a) and core-tearing activity (b). Optimization of profile parameters to match experimental values (c) results in n_f profiles shown in (d) early and late in the discharge.	82
5.23	Reconstructed fast-ion profiles, normalized to the bulk ion density n_f/n_i (top) and β_f (bottom) profiles for the two datasets early and late in the discharge.	83
5.24	A side-by-side comparison of the ensembled $n = 5$ and $n = 4$ activity for both datasets shows a predominance of $n = 5$ activity.	83
5.25	Burst ensemble for (a) 300 kA and (b) 500 kA dataset. Mode amplitude versus time (c) shows more abrupt bursting behavior at higher current.	85
5.26	Representative Alfvén continua of the two datasets.	85
5.27	Fast-ion (red) and magnetic (blue) pressure profiles and corresponding scale lengths.	87
5.28	Comparison of modeled (TRANSP) and experimental β_f profiles. A reduction in core β_f is consistent with EPM activity driving fast-ion transport.	88
5.29	The deuterium beam power scan revisited from Section 4.5. Various beam currents (a) result in different saturation levels of the neutron flux (b). The ensembled $n = 5$ tearing mode activity also shows a reduced effect on the tearing mode reduction at lower beam current (c). q_{mag} (black) and q_f (red) with approximate island widths (d) sets the diffusive boundary at which fast-ion islands overlap. Modeling a diffusive region outside this radius and a gradient limited profile inside this radius leads to varied n_f profiles (e).	89

1. BACKGROUND

At the largest scale this work takes place within a field of research that is not only about the development a new renewable source of energy, but one that once shown to be feasible, will reshape the course of human history and quite possibly the ultimate fate of this planet. The details of this research do not convey the urgency of the larger problem being addressed in the field of plasma fusion research. Nor, typically, does anything maintain a wide perspective when viewed at the granular level. Therefore it is this opening chapter that will serve to illustrate what has ultimately motivated this project.

To say that my contribution to this field is small is still an embarrassingly large overstatement. However, it is the loftiness of the aims of fusion energy and not the importance of my work that merit beginning from the largest scale, starting with a description of the energy situation and the current threats to the earth. It is my hope that this will provide the needed context and background for this thesis so that even when we're deep into the details, the overarching importance of the work being done in this field will not be forgotten.

1.1 The Energy Crisis

The energy currently utilized to sustain and drive life on Earth can be traced back almost exclusively to the sun. The sun provides the direct energy used in photosynthesis feeding both plants and ultimately all animals on Earth, causes wind through differential heating of the earth's surface, and drives the water cycle. All of these processes can and have been harnessed to create sources of energy (photovoltaic cells, wind farms, hydroelectric power, etc.). Without the sun, none of these mechanisms would exist, nor would life as we know it. But there are other means of producing energy, such as the radioactive decay of heavy nuclei or the residual heat leftover from the earth's formation. Nuclear fission reactors utilize the

radioactive decay process to create electricity, and geothermal heating has risen in recent years as a more environmentally friendly way to heat certain spaces. As the energy demands of the world continue to grow, meeting this need will ultimately rest upon developing the most effective use of what exists around us.

Due to the industrialization and technological advancement that has taken place in the last century the earth has seen a drastic increase in energy consumption. The US Energy Information Administration reports that the world generated 21,532 TWh of electricity in 2012 compared to 8,018 in 1980 [1]. Looking further back we observe a drastic increase coincident with the industrial revolution, continuing through to today (Figure 1.1). As our civilization grows and advances so do our energy needs. These needs are met through all of the ways that we know how to make energy, and vary in terms of access to raw materials, cost of production, environmental impacts, safety, and reliability.

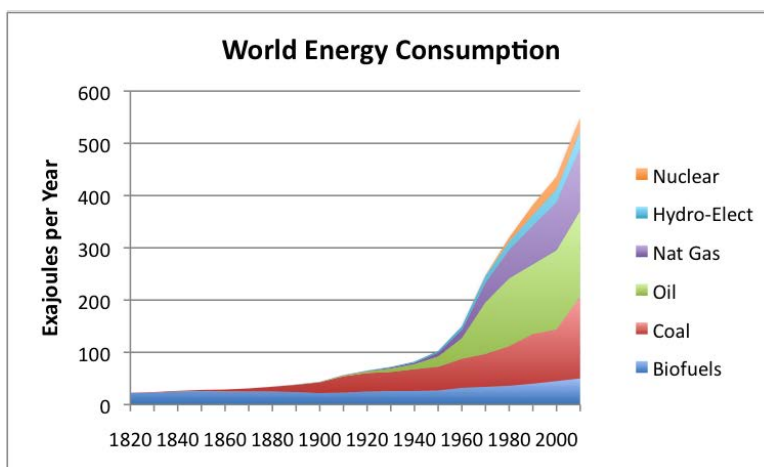


Fig. 1.1: World energy consumption broken down by type, showing the drastic rise in production from the Industrial Revolution to present day [1]

The IEA estimates that in 2007, 86.4% of the world's energy came from natural gas, oil, and coal. These sources, collectively known as fossil fuels, exist as a result of natural processes over hundreds of millions of years. Under certain conditions ancient plant and animal life would die, decompose, and become buried under layers of earth, sometimes beneath ancient seas that eventually dried up and receded. Over millions of years the matter decomposed into organic materials and became fossil fuels. The type of fossil fuel depends upon the type of organic matter as well as the geologic processes and temperatures to which it was exposed.

Oil and natural gas result from organisms that lived in the water becoming buried under ocean and river sediments. Heat, pressure, and bacteria combined to compress the material, creating oil in most areas, but continuing to produce natural gas in deeper, hotter regions. Coal is a byproduct of the remains of dead trees and ferns that were subjected to similar geologic forces.

Why is this information important? For two reasons. First, from an environmental perspective, the fact that fossil fuels are ultimately derived from dead plants means that they contain large amounts of carbon (anthracite coal is in fact almost pure carbon). The burning of fossil fuels releases around 21.3 billion tonnes of CO_2 per year, while the earth can only absorb roughly half that amount [1]. This leads to a large annual expulsion of CO_2 , a harmful greenhouse gas, into the atmosphere. Much has been written on the topic of anthropogenic global warming, and the reader is referred to the IPCC [4] for an extensive report on the status of climate science. Figure 1.2 clearly shows temperatures and sea levels are rising while ice and snow levels are diminishing, posing serious threats to the planet. Second, from a demand perspective, an understanding of the timescale needed for the production of fossil fuels reveals how unsuitable it is as a long term energy option. A look at Figure 1.1 shows that our need for energy is increasing rapidly. This is not only due to the increase in world population from around 1 billion in the early 1800s to over 7 billion today, but also an increase in per-capita energy use as societies become increasingly advanced (Figure 1.3). Although the processes that create fossil fuels are still at work, the demand far outstrips the creation, so much so that fossil fuel creation is not even factored into consumption projections. Our supply of fossil fuels is indeed finite, and although estimates vary, the theory that fossil fuel use will generally follow a bell curve (known as Hubbert's Peak theory) is generally accepted, and whether or not the peak of this curve has already passed is currently being debated. Fossil fuel, which provides over 80% of the world's energy, is both unhealthy for the environment and quickly running out.

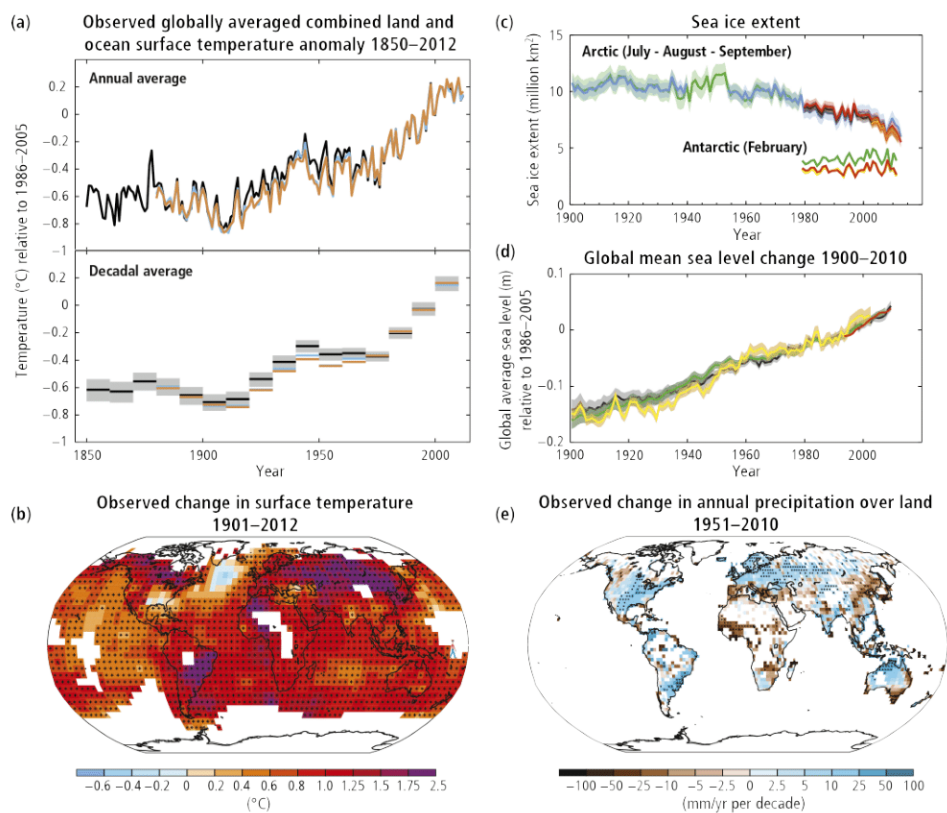


Fig. 1.2: IPCC report graphic showing global trends in temperature anomalies, surface temperature, sea ice extent and sea level change, and land precipitation

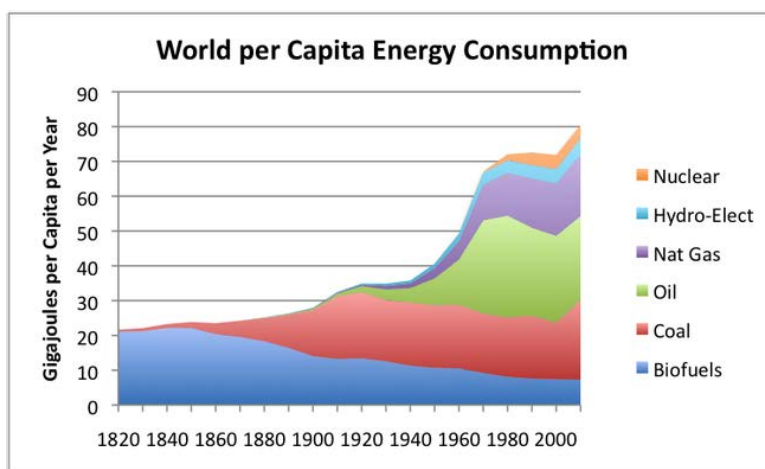


Fig. 1.3: Per capita energy consumption has drastically increased as our societies have become more technologically advanced

1.2 *The Green Movement and Renewable Energies*

Born out of the increasing understanding of the earth's climate, the movement towards environmentally friendly and renewable sources of energy has resulted in the development of many new technologies, intended to offset and ultimately replace the existing harmful forms of energy production. The most common and well developed methods of producing "green" energy are wind, solar, and hydroelectric. While their contribution to the global energy demand is increasing, there are some difficulties with these technologies that prevent them from offering a solution to our energy needs.

Solar energy is the most direct form of energy production, capturing energy directly from the sun through photovoltaics (solar cells), concentrated solar power, or solar water heating. In its 2000 World Energy Assessment, the United Nations Development Programme estimated that the annual solar energy potential was several times the annual world energy consumption. The principal difficulty of solar energy is that the production is often offset from its consumption. Energy is produced during the day while lighting demands, as well as heating in colder climates, peak during the night. Although energy storage technology is improving, solar technology at this time is not a suitable replacement for the backbone energy production provided by the fossil-fuel industry.

Facing similar problems are wind and hydroelectric power. While these technologies do not suffer from the problem of production being high while consumption is low and vice versa, the main issue is that of transmission. Wind and hydroelectric power are bound geographically- wind farms to hilltops and other windy corridors, hydroelectric to rivers and streams. Despite having over 50,000 large dams in over half the world's rivers the energy produced through hydroelectricity is not nearly enough to satisfy the demand. Power generated by this means also poses ecological threats, preventing spawning migration of fish, reducing biodiversity in rivers, encouraging poor water quality, and though debated may also be contributing to climate change through methane emissions of reservoirs. There is in fact a growing environmental movement to start tearing down dams (see for example the documentary "Dam Nation"). Wind farms have sprung up around the world in recent years, but much like solar and hydroelectricity, can't provide a viable alternative to our existing

energy economy. While being a clean, cost-effective, domestic, and renewable source of energy, the locations best suited for wind-energy generation are often furthest from cities where the energy is needed.

Many other technologies are involved in the move towards a sustainable and environmentally friendly energy future. Energy storage methods, bio-fuels, photosynthetic materials, green building practices, even energy efficient lightbulbs all contribute to an ever changing energy landscape. However, due to the pressing needs presented by the changing climate and the difficulty faced by many of the leading renewable energy technologies, a green alternative for backbone power supply is needed. You may not be surprised, but I have one in mind.

1.3 The Fusion Solution

Fusion energy has been a research goal worldwide since the early 1950s. It is in many ways similar to the nuclear process involved in the fission industry. In both cases energy is produced through the manipulation of matter on the sub-atomic level, and both face issues of confinement. Fusion refers to the process of combining elements to create heavier nuclei whereas fission is the process of splitting a nucleus into smaller (and usually unstable) elements. Energy is released both by putting together light elements and splitting heavier ones as there is a peak in the curve of net binding energy per nucleon at iron (Figure 1.4). The binding energy is a measure of how much energy is required to split a nucleus into its constituent protons and neutrons. This is a positive quantity for all elements and is the difference between the attractive nuclear forces and the repulsive electric forces (protons repelling other nearby protons). From light elements up to iron this quantity increases as the increase in nuclear attraction outweighs that of electric repulsion. Beyond iron however, this balance reverses, and the net binding energy per nucleon begins to decrease. As a consequence a hydrogen and deuterium nucleus are more massive separately than when combined to form He-3 (Helium nucleus with 2 protons and 1 neutron), the difference in mass being their difference in binding energies. Similarly a uranium atom is more massive than the (higher binding energy) byproducts resulting from its splitting. It is this difference in mass that is released as energy in a fusion or fission reaction.

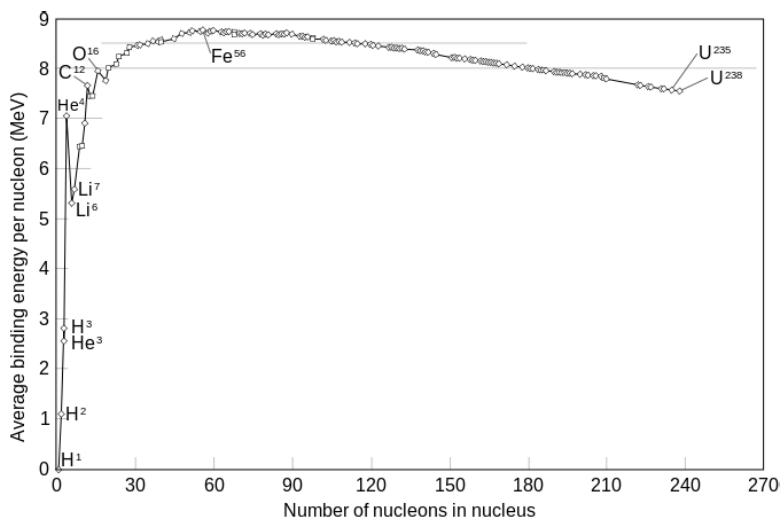


Fig. 1.4: Average binding energy per nucleon vs. atomic number

Fission reactors suffer from radioactive waste, meltdown scenarios, and the hassle of producing fissile material. A successful fusion reactor by contrast, would produce waste with a much shorter half-life (or if utilizing aneutronic advanced fueling scenarios almost none at all), would have no threat of meltdown, and would make use of the most abundant element in the universe, making it the ultimate green and renewable energy source. Not only is it environmentally friendly, but fusion power plants are easily integrable into the existing power grid, able to adjust output to meet demand, and can be built near locations where demand is high avoiding the issues of energy storage and transport that currently limit implementation of other renewable solutions.

Some of the most pressing challenges in fusion research are confinement and transport. In order to achieve a fusion reaction, two light nuclei must come in close enough proximity for the nuclear force to overcome the electromagnetic repulsion, at which point the nuclei will snap together and release the difference in binding energies. To increase the likelihood of such an occurrence the nuclei in the fuel must be either very close together (very dense), moving very fast (high temperature), or both. In laboratory plasmas temperatures of tens of thousands or even millions of degrees are not uncommon. These high temperatures exceed the utility of material walls.

Inertial confinement techniques avoid the container problem by simply not having one. A frozen pellet of deuterium is compressed by meticulously timed and crafted lasers simul-

taneously impacting the pellet. The heat from the shock wave and high density from the implosion causes the core of the pellet to fuse. The resulting energy released from the fusion in the core causes the pellet to explode. This method faces many technological challenges due to the precision required by the laser system and the lack of a clear cycling or energy removal strategy, and no net energy gain has been achieved through this technique.

Magnetic confinement is another means of combating the containment problem. When a gas is super-heated, the gas enters the plasma state wherein electrons become disassociated with the atoms in the gas creating a quasi-neutral mass of ions and electrons. The Lorentz force causes charged particles to then travel in helical orbits around magnetic field lines, restricting their movement perpendicular to the field but allowing unrestricted motion parallel to it. The aurora is an example of this phenomenon- charged particles from the solar wind hit the earth's magnetic field and are diverted to the polar regions where they collide and ionize different atmospheric atoms, causing the emission of the familiar greens, reds, and blues. Making use of an ion's affinity for sticking to field lines, magnetic confinement geometries are typically toroidal vessels where the magnetic field lines wrap around and connect back to themselves in an effort to keep the particles away from the vessel wall.

While the initial magnetic field can be prescribed by the experimenter, the plasma itself generates electric and magnetic fields as its constituent ions and electrons move around the machine. This makes the plasma-confining magnetic field geometry dynamically evolving. As the research in this field has borne out, as soon as one instability is understood and controlled, another seems to emerge. In addition to cross-field transport due to the perturbed magnetic field (\tilde{b}) of instabilities, particles drift off of magnetic field lines due to non-uniformities, and collisionality in dense plasmas can enhance particle and energy transport out of the machine.

Despite these difficulties, great progress has been made on the frontier of fusion in a magnetically confined plasma. Many universities, national labs, and a growing number of private industry companies are contributing to the growing body of knowledge and improving our understanding of how to achieve fusion in a laboratory scenario. As we move into an uncertain future facing environmental problems from climate change and an ever increasingly scarce fossil fuel supply, laboratory plasma fusion shows the promise of being a clean, safe, renewable, and viable replacement as the backbone energy-providing technology.

2. INTRODUCTION

2.1 Outline

Particle behavior and confinement is an important aspect of any magnetic confinement fusion reactor. In order to sustain a “burning” plasma, the high energy charged fusion products must be confined long enough to transfer their energy back into the plasma so as to perpetuate further fusion reactions. The toroidal magnetic geometry found in tokamaks and most other magnetic confinement devices induces drifts due to curvature and non-uniformity and the presence of large numbers of particles causes confinement degradation through large scale plasma waves and collisionality, potentially damaging the containment vessel itself. Two main categories of fast-particle-driven instabilities are important; so called gap modes (which are weakly damped normal modes of the plasma), and continuum modes which are strongly damped, strongly driven modes on the shear Alfvén continuum.

This thesis is a set of new measurements and orbit modeling which, when considered together with previous results, help answer the question of what limits the fast-ion content in the core of the NBI-heated RFP. The RFP and neutral beam heating of it (for which the MST is the only experiment in the world) and standard diagnostics are introduced in 2.2-2.3 below. A discussion of fast-ion driven Alfvénic mode activity, largely responsible for the transport of energetic ions, and previous measurements of a critical fast-ion pressure in other devices is found in 2.4-2.5. A summary of the new results in this thesis is in 2.6.

Chapter 3 is a detailed description of the fusion neutron diagnostics developed to measure the fast-ion density profile. Chapter 4 describes the motion of fast ions in the RFP equilibrium field and includes discussion of fast-ion confinement, the rapid buildup of an energetic population, and a resulting destabilization which leads to a saturated fast-ion content. Chapter 5 compares measurements from multiple plasma conditions to explain the

limiting behavior. The stability to the EPM represents an upper bound on fast-ion content in a magnetically confined plasma; a measure of the fast pressure profile at marginal stability is made for the first time in the RFP. Final thoughts and a discussion of future work are found in Chapter 6.

2.2 *MST and Standard Diagnostics*

2.2.1 *The Madison Symmetric Torus*

The Madison Symmetric Torus is a toroidal magnetic confinement experiment capable of producing reversed-field pinch plasmas. These are characterized by a reversal in the direction of the toroidal magnetic field near the edge. The most common toroidal device, the tokamak, uses external coils to produce a large toroidal field in the plasma. In an RFP, the toroidal field is not driven externally, but allowed to arise naturally by currents within the plasma. Thus a large externally imposed B_ϕ and relatively modest I_p for the tokamak, compared with comparable B_ϕ and B_θ in MST leads to significantly different q-profiles, a feature with implications on mode stability and fast-ion dynamics. Typical magnetic field profiles are shown in Figure 2.1. MST is one of only a handful of RFPs currently in operation, alongside RFX-mod [5] in Padua Italy, EXTRAP-T2R [6] in Stockholm Sweden, RELAX [7] in Japan, and most recently KTX [8] in China. The RFP, with a very high current density and naturally high β is a fusion energy concept that can be driven to ignition by ohmic heating alone, with no need for complicated and vulnerable RF or NBI heating systems. Thus RFPs provide an alternative regime for studying plasmas and for discovering a way forward to fusion.

The MST vacuum vessel as well as the diagnostics relevant for this work (those discussed here and in 3.4) are shown in Figure 2.2. The plasma parameters of MST are specified in Table 2.1 and typical MST discharge signals are illustrated in Figure 2.3. The line-integrated electron density climbs rapidly during ionization at the onset of the discharge, then stabilizes. The toroidal plasma current ramps up during the first 15 ms to its flat-top value before ramping back down towards the end of the discharge. During the 20-30 ms flat-top period the plasma is in its metastable state where the major evolution of the magnetic

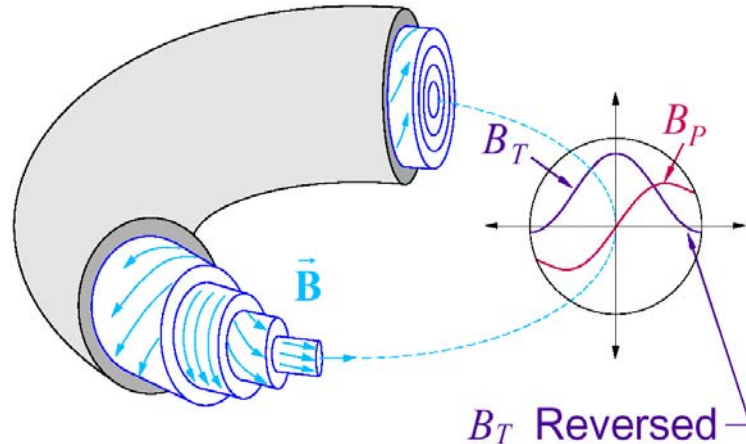


Fig. 2.1: The RFP magnetic topology. A toroidal field of similar amplitude to the poloidal field reverses direction near the edge.

field is determined by the sawtooth cycle, seen as the large spikes in many of the operation signals. Most experiments are conducted during this time period.

Parameter	Abbreviation	Typical Value	Range (\pm)
Plasma Current (MA)	I_p	0.4	0.2
Axial Toroidal Field (T)	$B_{phi}(0)$	0.4	0.2
Axial Safety Factor	$q(0)$.2	.03
Edge Safety Factor	$q(a)$	-0.15	0.15
Electron Density (m^{-3})	\bar{n}_e	1.0×10^{19}	0.7×10^{19}
Electron Temperature (keV)	T_e	1.0	1.0
Discharge Length (ms)	–	60	30

Tab. 2.1: MST Parameters

Sawtooth events are times of global magnetic reconnection within the plasma and are named after their characteristic shape on most diagnostic waveforms. These events are a relaxation of the peaked parallel current density profile, resulting from both preferential core drive (applied toroidal induction E_ϕ aligns with B in the core) and a lower plasma resistivity. The tearing instability is driven by ∇J_\parallel creating a broad spectrum of modes resonant in the

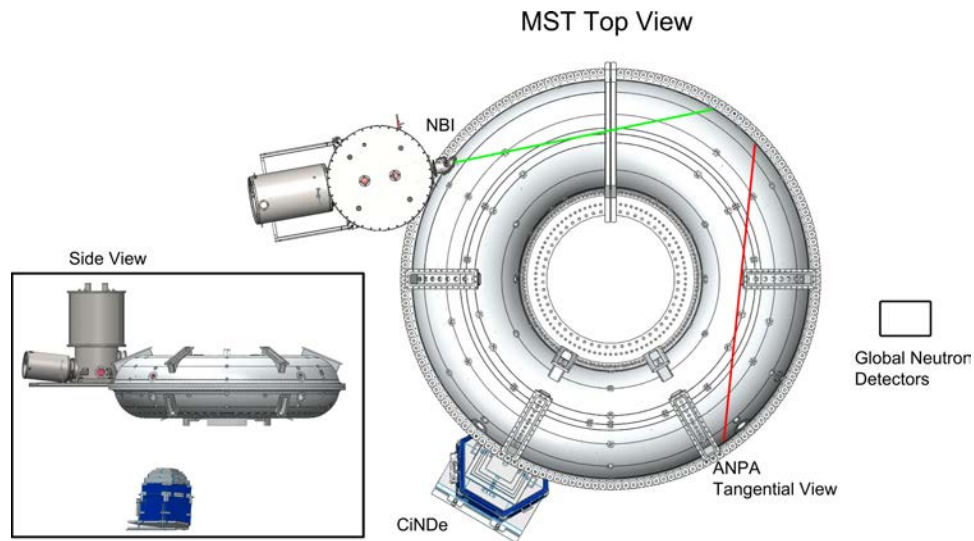


Fig. 2.2: MST vacuum vessel and relevant diagnostics. NBI, CiNDe, ANPA, and global neutron detector locations are shown with appropriate injection/viewing geometries.

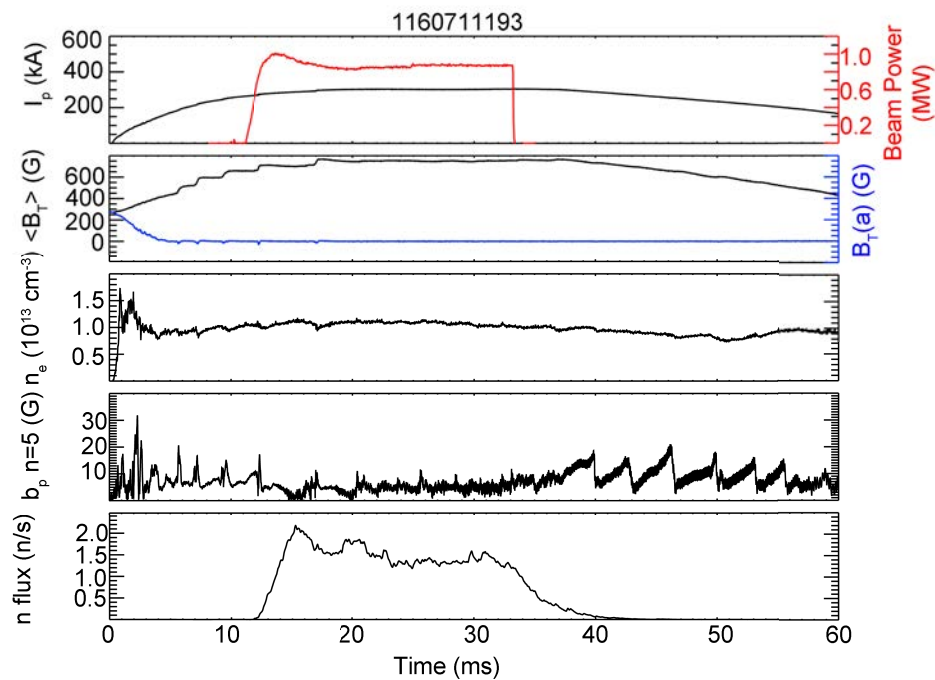


Fig. 2.3: Typical MST discharge signals. (a) Plasma current and neutral beam power (b) Volume-averaged and edge-valued toroidal magnetic field (c) Line-averaged electron density (d) Core-most resonant tearing mode amplitude (e) Total MST neutron flux

plasma at locations where the wave vector of the mode is perpendicular to the magnetic field

$$\mathbf{k} \cdot \mathbf{B} = 0 \quad (2.1)$$

$$\mathbf{k} \cdot \mathbf{B} = \frac{m}{r}B_\theta + \frac{n}{R}B_\phi = 0 \quad (2.2)$$

$$\Rightarrow \frac{-rB_\phi}{RB_\theta} = \frac{m}{n} = q(r) \quad (2.3)$$

Where we have introduced the safety factor $q = RB_\phi/rB_\theta$, and shown that the condition for resonance is met where q is a rational number $q = m/n$. These modes generate a $\langle \tilde{v} \times \tilde{b} \rangle$ emf that rapidly flattens the current. Magnetic fluctuation levels then quickly subside and the applied toroidal induction begins the process again. This is analogous to the beam-sourced fast ion pressure which drives periodic bursts of Alfvénic activity that flatten the pressure gradient.

Finite resistivity in the plasma allows the growth of island structures at q -rational surfaces in the plasma (Figure 2.4). As these modes grow, they may overlap creating a region of stochasticity (discussed further in Section 4.1). At a sawtooth event, $m = 1$ modes present in the interior of the plasma may nonlinearly couple with $m = 0$ modes near the plasma reversal surface enabling rapid relaxation and large drops in stored magnetic energy. This coupling may be limited, and the resulting strength of the sawtooth reduced, by removing the $m = 0$ mode rational surface from the plasma. In MST this is achieved by operating with a reversal parameter, defined as $F = B_T(a)/\langle B_T \rangle$, equal to zero. This is controlled by the toroidal field (TF) system, a second iron core transformer that drives current poloidally in the shell. During a discharge, an initial toroidal field at the wall quickly goes to zero as the plasma self-evolves, at which point the TF system circuit is opened, preventing current from flowing and holding $B_\phi(a) = 0$ (and thus $F = 0$). Minimization of the sawtooth relaxation effects by choosing a zero boundary toroidal magnetic field allows a more careful study of the energetic particle pressure dynamics. Therefore only $F = 0$ plasmas were studied.

2.2.2 Advanced Neutral Particle Analyzer and D-Alpha Array

The advanced neutral particle analyzer (ANPA) on MST provides information on the distribution of high energy (10-35 keV) ions along the detectors line-of-sight. Built in collab-

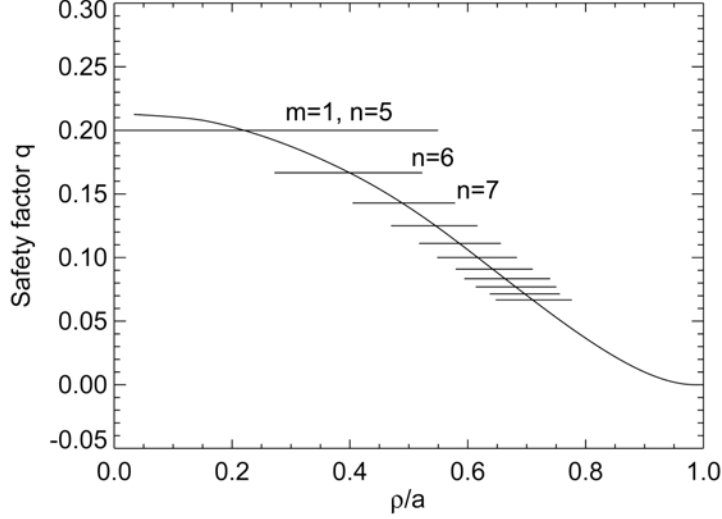


Fig. 2.4: Typical q profile for MST with magnetic island locations ($n = 5-15$) and approximate widths overlaid. Note high density of islands at larger radius.

oration with the Budker Institute, it was installed and has been in operation since 2011 [9]. Ions in the plasma can neutralize via charge exchange with background neutrals and exit the plasma in a straight line. A fraction of fast ions will neutralize with the appropriate pitch ($v_{\parallel}/|v|$) and be collected. Incoming neutrals are stripped by passing through a 10 nm thick carbon foil which, if biased, gives the newly ionized neutral additional energy, effectively shifting the energy range of the detectors downward. The ANPA is an “ $\mathbf{E} \parallel \mathbf{B}$ ” design wherein a magnetic field separates the ions by energy and an electric field (parallel to the magnetic field) separates the ions by mass. The particles are then collected into two arrays of 10 channeltrons; one array each for hydrogen and deuterium [10].

Physical placement of the ANPA on different MST ports leads to distinct lines of sight and sampling of the fast-ion distribution. A radial orientation of the ANPA will collect lower-pitch ions while a tangential viewing geometry will detect a convolution of core-localized high-pitch ions and edge low-pitch ions. Accounting for the reionization fraction (f_r), the ANPA receives a flux of

$$\Gamma_{meas} = \int_L n_0 n_{fi} \langle \sigma v \rangle_{cx} \delta(\gamma - \gamma_c) (1 - f_r) dl d\gamma \quad (2.4)$$

where n_0 is the neutral density, n_{fi} is the fast-ion density, $\langle \sigma v \rangle_{cx}$ is the charge exchange cross

section, and is integrated along the detector line of sight. Proper measurement of the fast-ion density thus requires knowledge of the background neutral density which is estimated through D_α emission.

H-alpha is a spectral line of the Balmer series corresponding to a neutral hydrogen's electron falling from the 3rd to 2nd lowest energy level. The light from this transition is emitted isotropically at $\lambda = 656.28$ nm for hydrogen. For deuterium (MST's main fueling gas) emission is at $\lambda = 656.1$ nm and is referred to as D-alpha (D_α). The intensity of emission is given by

$$\gamma_{D_\alpha} = n_e n_0 \langle \sigma v \rangle_{excitation} \quad (2.5)$$

where n_e is the electron density, n_0 is the neutral density, and $\langle \sigma v \rangle_{excitation}$ is the electron impact excitation rate. MST has a 16 photodiode array that detects D_α light and uses equation 2.5 to calculate the chord-averaged neutral density of deuterium. This can be inverted to find the 2D background neutral density profile, but because MST's neutral density is much higher near the edge ($\sim 10^{18} m^{-3}$) than in the core ($\sim 10^{15} m^{-3}$), standard Abel inversion results in extremely large uncertainties. In practice, as the neutral density changes throughout a discharge, the D_α signals are used to normalize and provide a relative calibration between ANPA energy channels.

Lacking an absolute calibration and being sensitive primarily to high-pitch ions in the core, the ANPA cannot provide complete information on the fast-ion distribution but does provide information on the energy distribution which is essential to the calculation of the fast-ion beta profile.

2.3 The MST Neutral Beam Injector

Neutral beam injection became a prevalent control tool in the 1970s [11]. High energy neutral particles are injected into the plasma volume where they ionize and transfer their energy to the bulk plasma. This has become a very useful tool not only for plasma heating and current drive, but also for probing important physics.

In 2009 a 1 MW (40 A, 25 keV) neutral beam injector (NBI) was installed on MST. It has a tangential injection geometry, as seen in Figure 2.6 which results in a large core-localized

and high pitch population of ions. Typical beam parameter are summarized in Table 2.2. Prior to this work the beam was typically fueled with 95% hydrogen and doped with 5% deuterium to produce a measurable neutron signal as a proxy for fast-ion content through beam-target fusion. In the presence of EP instabilities, only particles resonant with the fluctuations are transported. Due to the species dependence of their resonance conditions, we therefore expect (and have observed, see Section 4.5) deuterium fast ions (and therefore neutron signal) to behave independently of the hydrogen fast ions, even in the presence of hydrogen-driven EPs. For this reason we use 100% deuterium fuel for these experiments in order to use the D-D fusion neutron flux as a real indicator of the fast-ion content.

The neutral beam enters the plasma at a 45° horizontal angle from the wall and 6° below horizontal with a 3.35° divergence from a porthole 19° poloidally above the outboard midplane. Most of the beam neutrals (typically $\sim 90\%$) become fast-ions in MST through electron impact, ion impact, and ion charge exchange with the background plasma.

A 25 keV deuterium ion has a speed of $\sim 1.55 \times 10^6$ m/s (2.2×10^6 for a hydrogen ion). Due to the tangential injection geometry and plasma density profile, most of the beam neutrals ionize near the core, where their velocity is highly parallel to the local magnetic field. This (along with good confinement) creates a large population of core-localized high pitch fast ions in MST. Calculations done using the TRANSP code [12] model neutral beam deposition resulting in the fast-ion distribution shown in Figure 2.5. TRANSP modeling is

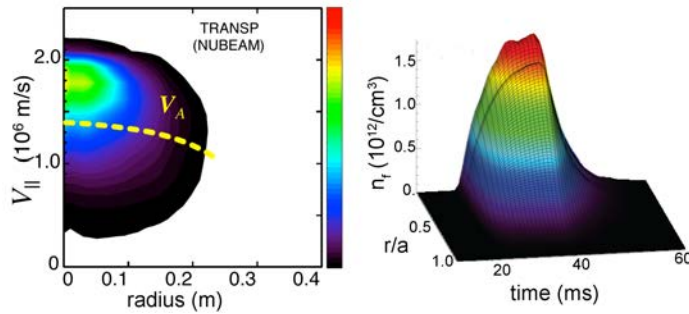


Fig. 2.5: TRANSP modeling of beam deposition from MST's 1 MW neutral beam injector predicts a large core-localized population of high-pitch ions.

restricted to regions of positive B_ϕ as it uses toroidal flux as a radial coordinate, which is only a small correction for the $F = 0$ plasmas studied herein (even in $F = 0$ plasmas a few centimeters are truncated from the edge of the plasma as B_ϕ gets small but before it

Parameter	Typical Value
Beam Energy	25 keV
Beam Power	1 MW
Pulse Length	20 ms
Composition	100% D
Energy Fraction (E:E/2:E/3:E/18)	86%:10%:2%:2%

Tab. 2.2: NBI Parameters

reaches zero). Calculations for NBI in MST consider only classical fast-ion transport, which is a major omission as EPMS are shown here to limit the fast-ion content. Thus TRANSP modeling benchmarks experimental results only before the onset of these modes.

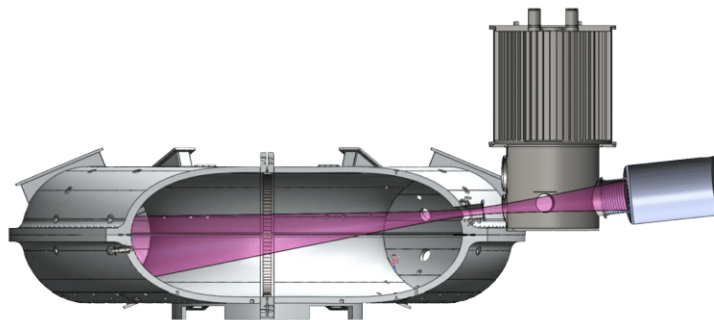


Fig. 2.6: The tangential 1 MW neutral beam injector on MST produces a large population of core-localized high-pitch ions.

2.4 The Alfvén Continuum, Gap Modes, and EPMS

Alfvén waves were first theoretically posited by Hannes Alfvén (after whom the waves are named) in 1942, just before the first laboratory plasma experiments would take shape in the late 40’s. By considering a conducting liquid in a constant magnetic field, he calculated the velocity of a transverse wave in the liquid and suggested that they may play some role in astrophysical plasmas- specifically in sun spot motion. These transverse waves of the magnetic field are often compared to a wave on a guitar string. For a guitar, the tension, linear density, and length determine the resulting wave velocity and frequency. In a plasma where the field line is being “plucked,” the magnetic field strength provides the tension and the plasma the inertial mass. On a toroidal surface however, it is more

helpful to consider these waves as a two dimensional wave, more akin to the vibration on a drum than a guitar string. The combination of magnetic field strength, plasma density, and periodicity constraints set by the “drum” determine the mode velocity and frequency. We can characterize these waves mathematically, starting by combining Faraday’s Law and Ampère’s Law to get the general wave equation;

$$\nabla \times \mathbf{E} = -\frac{\partial \mathbf{B}}{\partial t} \quad (2.6)$$

$$\nabla \times \mathbf{B} = \mu_0 \left(\mathbf{J} + \epsilon_0 \frac{\partial \mathbf{E}}{\partial t} \right) \quad (2.7)$$

$$\nabla \times \nabla \times \mathbf{E} = -\mu_0 \left(\frac{\partial \mathbf{J}}{\partial t} + \epsilon_0 \frac{\partial^2 \mathbf{E}}{\partial t^2} \right) \quad (2.8)$$

In order to describe the wave behavior we transform to the perturbed quantities by making the substitutions $\mathbf{E} \rightarrow \tilde{\mathbf{E}}$ and $\mathbf{J} \rightarrow \tilde{\mathbf{j}}$. Assuming fluctuations of the form $\propto e^{i(\mathbf{k}\cdot\mathbf{x}-\omega t)}$ and linearizing, Equation 2.8 becomes

$$-\mathbf{k} \left(\mathbf{k} \cdot \tilde{\mathbf{E}} \right) + k^2 \tilde{\mathbf{E}} = \frac{\omega^2}{c^2} \tilde{\mathbf{E}} + \frac{i\omega}{\epsilon_0 c^2} \tilde{\mathbf{j}} \quad (2.9)$$

For a transverse wave with motion parallel to \mathbf{B} we note that $\mathbf{k} \parallel \mathbf{B}_0$ and $\mathbf{k} \perp \tilde{\mathbf{E}} \perp \tilde{\mathbf{B}}$. Using $\tilde{\mathbf{j}} = q_i n_0 \tilde{v}_i$ and noting $\mathbf{k} \cdot \tilde{\mathbf{E}} = 0$, the component along $\tilde{\mathbf{E}}$ becomes

$$\epsilon_0 (\omega^2 - c^2 k_{\parallel}^2) \tilde{E} = -i\omega n_0 e \tilde{v}_i \quad (2.10)$$

Decomposing the ion equation of motion into components parallel and perpendicular to $\tilde{\mathbf{E}}$ and linearizing we can determine \tilde{v}_i . We make the convention $\tilde{\mathbf{E}} = \tilde{E} \hat{x}$ and proceed as

follows;

$$m_i \frac{\partial \tilde{\mathbf{v}}_i}{\partial t} = e \left(\tilde{\mathbf{E}} + \tilde{\mathbf{v}}_i \times \mathbf{B}_0 \right) \quad (2.11)$$

$$\hat{x} : -i\omega m \tilde{v}_x = e \tilde{E} + e \tilde{v}_y B_0 \quad (2.12)$$

$$\hat{y} : -i\omega m \tilde{v}_y = -e \tilde{v}_x B_0 \quad (2.13)$$

$$\tilde{v}_x \left(1 - \frac{e^2 B_0^2}{m^2 \omega^2} \right) = \frac{ie \tilde{E}}{m\omega} \quad (2.14)$$

$$\tilde{v}_x = \frac{ie}{m\omega} \left(1 - \frac{\Omega_c^2}{\omega^2} \right)^{-1} \tilde{E} \quad (2.15)$$

where $\Omega_c = eB_0/m$ is the ion cyclotron frequency. Substituting this into Equation 2.10,

$$\epsilon_0 (\omega^2 - c^2 k_{\parallel}^2) = \frac{n_0 e^2}{m} \left(1 - \frac{\Omega_c^2}{\omega^2} \right)^{-1} \quad (2.16)$$

$$\omega^2 - c^2 k_{\parallel}^2 = -\frac{n_0 \omega^2}{\epsilon_0 B^2} \quad (2.17)$$

$$\omega^2 - c^2 k_{\parallel}^2 = -\frac{\omega^2 c^2}{v_A^2} \quad (2.18)$$

$$\omega^2 \left(1 + \frac{c^2}{v_A^2} \right) = c^2 k_{\parallel}^2 \quad (2.19)$$

$$\omega = k_{\parallel} v_A \quad (2.20)$$

where we have utilized $\omega \ll \Omega_c$, the definition of the Alfvén velocity $v_A = B/\sqrt{\mu_0 n_0 m}$, and $v_A \ll c$.

In a cylindrical geometry, with the picture of a 2D “drum” surface in mind, we impose the periodicity constraints $m\lambda_{\theta} = 2\pi r$ and $n\lambda_{\phi} = L$ where r is the cylinder radius and L the length. Wrapping the cylinder into a torus makes the periodicity $L = 2\pi R$ where R is the major radius of the torus. Then using $k = 2\pi/\lambda$ we can write out the periodicity condition

for an Alfvén wave in a torus with mode numbers m, n

$$k_{\parallel} = \frac{\mathbf{k} \cdot \mathbf{B}}{|\mathbf{B}|} = \frac{(k_{\phi} B_{\phi} + k_{\theta} B_{\theta})}{|\mathbf{B}|} \quad (2.21)$$

$$= \left(\frac{n B_{\phi}}{R} + \frac{m B_{\theta}}{r} \right) \frac{1}{|\mathbf{B}|} \quad (2.22)$$

$$= \left(n + \frac{m R B_{\theta}}{r B_{\phi}} \right) \frac{B_{\phi}}{R |\mathbf{B}|} \quad (2.23)$$

$$= \left(n - \frac{m}{q} \right) \frac{B_{\phi}}{R |\mathbf{B}|} \quad (2.24)$$

Since both k_{\parallel} and v_A are functions of radius this gives us the familiar Alfvén continuum shown in Figure 2.7.

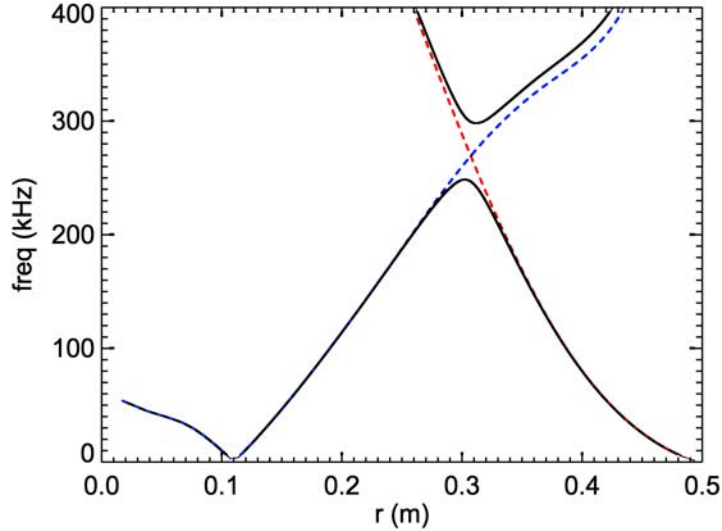


Fig. 2.7: The $m = 0, 1$ $n = 5$ Alfvén continuum for MST equilibrium values computed from 300 kA $F = 0$ discharge. Coupling between the $m = 0, n = 5$ mode (dashed red) and $m = 1, n = 5$ mode (dashed blue) opens a gap in the continuum around $r \approx 32$ cm (black).

We proceed with a discussion of the Alfvén continuum guided by the most recent review of the topic [13]. The dispersion relation expressed in Equation 2.20 shows that because the group velocity equals the phase velocity ($\partial\omega/\partial k = \omega/k = v_A$) then in a uniform plasma the wave would be dispersionless. However, as can be seen in Figure 2.7 the phase velocity has a large shear in the radial direction. Due to the finite width of these transverse waves, this means that parts of the wave at different radii would have different velocities and the wave packet would quickly disperse. The associated damping of the wave is associated with the

phase velocity gradient, $\gamma \propto \frac{d}{dr}(k_{\parallel}v_A)$.

Despite the large continuum damping, there are gaps in the Alfvén continuum where modes may be excited with modest driving. This is a common wave phenomenon that is a result of any periodic modulation of the index of refraction. In a torus, the curvature of the device results in a stronger toroidal field on the inboard side than on the outboard side, resulting in a periodicity in the Alfvén speed along a helical field line as it rotates around the geometric center of the torus. This is responsible for opening a gap in the Alfvén continuum known as the toroidicity-induced Alfvén eigenmode (TAE) centered at $f_{TAE} = v_A B_{\phi} / (4\pi q R |B|)$ with a width that is determined by the magnitude of the variation in B from the inboard to outboard side of the machine. Physically this gap opens up due to the coupling of the two adjacent m -number modes. For example, Figure 2.7 depicts the coupling between the (0,5) and the (1,5) mode due to the inclusion of the toroidal geometry (the TAE gap). An MSTFit reconstruction provides the necessary plasma profiles to compute the cylindrical Alfvén continuum, and an approximation was used to include mode coupling due to toroidicity [14]. In this case the $m=0$ wave is propagating in the opposite direction to the $m = 1$ mode and at the location where these frequencies cross in the cylindrical case, the two waves mix and the crossing is avoided.

The importance of these gaps is that they present a region of the plasma with a relatively large radial extent in which the wave damping is low so that a small amount of drive from say, an external antenna, may create a mode structure with substantial amplitude. This is in contrast to attempting to excite a mode at a frequency and radial location on the continuum. In these places the damping is large and the wave interacts strongly with the background plasma and the amplitude remains small. It is these two differing regions that give rise to the two categories into which SAWs typically fall, Alfvén eigenmodes (AEs- gap modes) and energetic particle modes (EPMs- continuum modes). AEs are given labels that relate them to the cause of the gap, such as the toroidicity-induced Alfvén eigenmode (TAE) or ellipticity-induced Alfvén eigenmode (EAE). AEs do degrade fast-ion content by enhancing transport, but the destabilization of these modes is governed by mode-particle resonances at specific locations in the plasma and do not always occur (the TAE depicted in Figure 2.7 for example, has never been observed in MST- see Section 4.4). EPMs on the other hand, are

excitations of Alfvén waves that occur on the continuum where damping is high. The mode amplitude grows only when the energetic particle drive outweighs this continuum damping and in contrast to the AE, the frequency of the mode is largely determined by the orbit characteristics of the energetic ions.

It is the different causes of mode activity that causes us to be interested in the EPM. AEs exist at certain frequencies and locations in the plasma, governed by the geometry (magnetic and physical) of the device. As such, these modes may or may not be excited. In principle, an experimenter could achieve an arbitrarily high fast-ion beta by only introducing particles that are non-resonant with the AEs. EPMs have their own criteria for destabilization (as discussed in section 4.4), but as we will see, since they are destabilized at high drive they are unavoidable when exploring the limits of fast-ion content in a device.

2.5 *A Short History of EPMs*

The first observation of fast-ion induced MHD activity and loss was made in the Poloidal Divertor Experiment (PDX) in 1982. With its 8 MW neutral beam injection system consisting of four perpendicular injection beams, strong magnetohydrodynamic activity was observed that resulted in a loss of 20-40% of the beam heating power [15]. Dubbed the “fishbone” instability due to its characteristic signal on the Mirnov coils, theoretical work soon followed that suggested the mode was a result of energetic particles destabilizing an internal kink mode and showed that a resonance between the mode rotation and the toroidal precession of the beam ions should eject the resonant ions [16, 17]. When the machine was converted in 1983 to the Princeton Beta Experiment (PBX) two of the neutral beams were reoriented to a tangential injection geometry. Shortly thereafter two new types of bursting mode activity were observed, both of which correlated with drops in D-D fusion neutron emission and bursts of charge-exchange neutral flux indicating a rapid transport of beam ions from the core [18].

Motivated by the unsatisfactory explanations of the observed mode activity, Liu Chen laid the theoretical foundation in 1994 for energetic particle modes by including both the finite size of the particle orbits and treating the energetic particle population non-perturbatively

[19]. In what has become a widely cited work, a new class of MHD modes with frequencies in the range of typical fast-ion transit, bounce, and precession frequencies are predicted. The theory updated the understanding of the fishbone instability.

Adding to the theoretical framework, a beam driven mode was identified by Cheng in 1995 (with supporting theoretical work by Briguglio [20], and Santoro [21]) called the resonant TAE (RTAE) that is “a beam-like mode with its frequency determined mainly by the wave-particle resonance condition” [22]. This theoretical framework emerged alongside the first experimental observations of EPMS. In 1995, Heidbrink described a “chirping” mode in DIII-D that required “large fast-ion beta, and low ratio of beam speed to Alfvén speed” [23]. By 2000, Zonca and Chen had developed analytic dispersion relations that not only predicted the frequency chirping observed in many devices, but predicted radial localization of the EPM due to strong spatial gradients in the energetic particle profile [24]. In 2001, large drops in neutron emission rate and loss of energetic ions was associated with what was at the time labeled an abrupt large amplitude event (ALE) associated with beam ions in JT-60U [25]. In a previous paper where these modes were referred to as bursting modes, they were found to be destabilized for a volume averaged fast-ion beta of $\langle\beta_{fi}\rangle \geq 0.2\%$ [26]. Based on the strength of the modes for a peaked versus hollow beam ion pressure profile they were led to infer “the high pressure or the high pressure gradient of fast ions in the central region, or both are considered to be responsible for the burst mode excitation.” In Wendelstein W7-AS a survey of MHD instabilities was reported in 2001. Although limited in fast-ion beta by the available neutral beam power, bursting modes with chirping frequencies were observed when the fast-ion beta became comparable to the thermal electron beta ($\beta_{fi} \leq 1\%$ in the core) [27]. NSTX observed a strong resonant fishbone interaction at the trapped particle bounce frequency [28]. A few years of further investigation showed an apparent threshold in EPM (and TAE) activity above a core beta ratio of 30% ($\beta_{fi}(0)/\beta_{tot}(0) > 0.3$) [29].

In this thesis, we argue that EPM stability represents the upper bound on fast-ion pressure. Weakly damped Alfvén eigenmodes can be destabilized with lower drive, but steps can be taken to mitigate their effects or avoid them altogether. This is an active topic today (as an example: Suppressing Alfvén eigenmodes by q profile engineering to improve fast-ion confinement [30]). For a more chronicled story, consider seminal energetic ion studies in the

DIII-D tokamak. The ability to run over a large range of reduced magnetic field, a wide range of shaping and current profiles, and with high power NBI allows studies of several crucial stability parameters. Toroidicity-induced Alfvén eigenmodes (TAEs) were first identified in the tokamak in both TFTR [31] and DIII-D where they reported a β_f up to 2% (volume averaged pressure normalized to edge magnetic field) by classical calculation (MCGO) [32]. Further studies found the stability limit to be $\beta_f \sim 1\%$ [33] for L-mode limiter discharges. In that work, techniques to increase the damping and hence the stability of the TAE were identified including increased pressure ($\beta_{thermal}$) and shaping techniques. In subsequent higher beta discharges (normalized beta $\beta_N \sim 3.5$, where $\beta_N \equiv \beta_t a B_t / I_p$ and β_t is the toroidal beta), the TAE was suppressed as they neared the ideal MHD stability limit, but another mode- the beta-induced eigenmode (BAE) appeared around half of the TAE frequency, caused by “a compressional response of the plasma to shear Alfvén waves in the presence of finite pressure and curvature” which also limited fast-ion content [34]. By moving to a more stable double null divertor discharge and operating at high B and low n_e , β_f became a significant fraction of the total β ($\gtrsim 1/3$) and a chirping mode was observed [23]. The volume averaged β_f limit for the EPM was $\beta_f \gtrsim 1\%$ but occurred for fast-ion parallel speed substantially less than v_A . Called the “chirp” instability due to the rapid drop in frequency during the burst, the theoretical framework followed predicting not only the chirping character of the mode but also a radial localization of the EPM due to strong energetic-particle gradients [24], an effect seen when they were first discovered. A critical fast-ion pressure appears to be reached at which point the mode grows and, due to enhanced fast-ion transport, the fast pressure profile relaxes.

Unlike an AE, the characteristics of an EPM are determined by the MHD properties of the background plasma *and* the EP distribution. As such, once the drive overcomes the continuum damping and the mode grows, the EP distribution can change rapidly, altering the characteristic frequency of the mode. The Berk-Breizman (BB) model [35], which predicts the nonlinear dynamics of the resonant particles using only four characteristic frequencies, has been quite effective in reproducing EPM effects experimentally observed. Chirping as well as periodic bursting behavior can all be explained in terms of the linear growth rate γ_L of the kinetic drive, the damping γ_d of the background plasma, the bounce frequency ω_b of

the resonant fast ions, and the rate ν_{eff} that particles leave and enter the resonance region. While in relative infancy, fast-ion effects on the RFP are similarly being studied. Modes in the TAE gap of EXTRAP-T2R were observed [36] arising naturally (without EP drive), as were lower frequency global- and reversed-shear Alfvén eigenmodes (GAEs and RSAEs) in RFX-mod [37]. While MST has a strong NBI for excitation of modes, the TAE, GAE, and expected beta-induced Alfvén eigenmode (BAE) have not been excited [38]. Magnetic islands can lead to a periodic distortion of the Alfvén speed and open a gap in the shear Alfvén spectrum [39, 40], and depending on the topology of a core-localized resistive kink, a similar HAE gap may be present [41]. Alongside a growing taxonomy of AEs in MST, strong EPM activity occurs during NBI. Figure 2.8 gives an example of the bursting mode character typically seen in MST, showing an $n = 5$ spectrogram for a 300 kA $F = 0$ discharge using deuterium NBI firing at 10-30 ms. EPM activity, hereafter interchangeably referred to as bursting modes, appears as semi-periodic discrete bursts of high frequency magnetic activity.

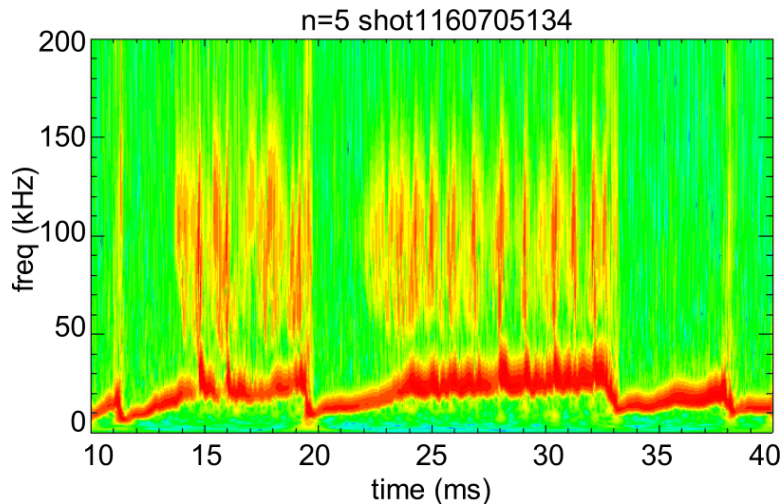


Fig. 2.8: Spectrogram depicting typical $n = 5$ bursting modes. Strong $n = 5$ tearing mode activity is shown and represents a good approximation for the core rotation frequency.

The excitation of AEs depends strongly on many factors resulting in a wide variety of modes observed in different devices, and each type of mode activity is associated with transport or loss of fast ions, causing a reduction in β_f . Even in the absence of AE activity β_f is limited due to the onset of EPM activity when the EP drive associated with a large $\nabla\beta_f$ overcomes the damping rate determined by the plasma’s MHD parameters.

2.6 Summary of key results of thesis

The purpose of this thesis is to investigate the interactions between the fast-ion population in MST and energetic-particle mode activity. In particular we are interested in seeking answers to the following questions: (1) What does the fast-ion density profile look like in MST? How does it change with EPM activity? (2) What is the mechanism for driving EPM activity? Can a threshold be identified characterizing the EPM stability?

To address the first question, the neutron detection suite for MST was improved. New neutron detectors capable of accurate flux measurements over the entire achievable range in MST were developed and calibrated using a beam-blip method [42]. A collimated neutron detector was constructed to measure the fusion reaction rate as a function of radius. The fast-ion density (n_f) and fast-ion beta (β_f) were computed using the ANPA diagnostic for fast-ion energy resolution ($f(E)$) and inversion of chord integrated neutron emissivity ($\Gamma = \int n_f n_i \langle \sigma v \rangle dl$). The measured fast-ion profile shows a core-localized population, consistent with classical predictions. No EPM induced transport was measured, however, pointing either towards expulsion of a very small population of fast ions from the core or of pitch angle scattering of fast-ions which results in the experimentally observed drop in ANPA signal without an associated drop in neutron emission.

The second question was investigated by comparing β_f profiles at various $|B|$, where it was found that EPM activity in the RFP is largely dependent upon a number of competing factors. With strong EP drive and reduced core-tearing mode amplitude, NBI readily populates a region of phase space that drives EPM activity. At plasma conditions of higher magnetic field, a higher core-tearing mode amplitude and weaker drive (due to sub-Alfvén beam ions) results in a much reduced gradient in the fast-ion beta profile and subsequently much weaker EPM activity. A critical gradient of $\nabla\beta_f = 0.5\%/cm$ was identified by studying profiles at marginal stability.

3. NEUTRON DETECTION

Effective measurement of the n_f profile is crucial for detailed studies of fast ion and EPM physics. One way to achieve this is by using a suite of neutron detectors to map the neutron emission within the device. Fusion reactions occur regularly in NBI-heated MST discharges and because the fusion reactivity (Figure 3.1) is such a sensitive function of relative speed, most of these reactions occur between beam and bulk ions. Therefore the neutron rate is correlated to the fast-ion distribution through other measurable quantities.

$$\Gamma_{MST} \simeq \Gamma_{bt} = \int f_f(E) n_i \sigma v dE dV \quad (3.1)$$

where σ is the fusion reaction cross-section at the fast-ion velocity v , and $\int f_f(E) dE = n_f$. In both D-D and D-T fusion reactions a neutron can be released and, having no charge, freely exits the plasma and passes relatively unimpeded through the vessel wall. This feature makes neutron detection diagnostically attractive as neutrons can carry information (as well as MeVs of energy) directly out of the plasma without the need for either window or vacuum port, but this also implies that they are difficult to detect. Neutron detection faces numerous experimental challenges, including large background signal levels, high detection rates, and widely varying detector behavior with neutron energy. In MST, an unavoidable and large unwanted count rate arises from high energy photons created through the bombardment of the aluminum vacuum vessel by fusion protons.

Three neutron detection diagnostics are used to measure fast-ion dynamics in MST. Two are global neutron flux measurements of varying sensitivity, the higher sensitivity for mixed fuel NBI or any thermal fusion measurements and the lower for the high flux environment of full deuterium beam NBI. The third neutron diagnostic is the collimated neutron detector where effective shielding provides a well-defined viewing volume. This chapter covers the

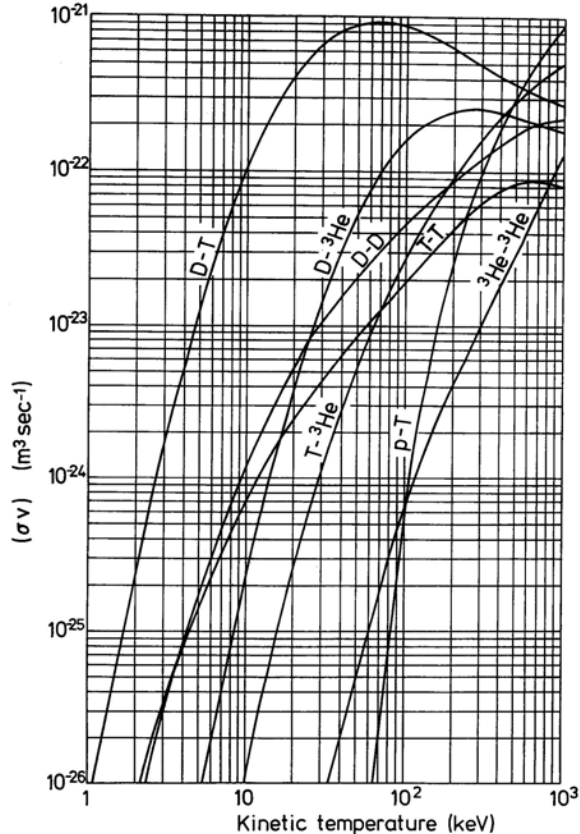
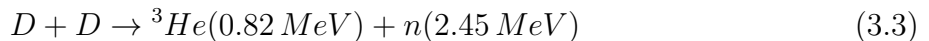


Fig. 3.1: Fusion reactivity rates for various fusion processes. The high velocity of MST beam ions relative to bulk means D-D reactivity is very sensitive to beam energy.

basics of neutron detection and calibration techniques as they apply to MSTs needs.

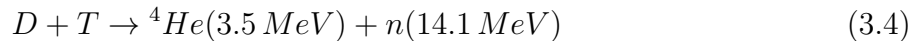
3.1 D-D Fusion

The D-D reaction has two branches, which occur with roughly equal probability. (The $D(d,p)T$ has a slightly higher cross-section up to around 15 keV in the center of mass frame above which the $D(d,n)^3He$ reaction becomes slightly more likely [43]).



While the $D(d,p)T$ reaction does not produce a neutron it does produce a triton. In the presence of both deuterium and tritium, a high energy neutron can be created through the

reaction



The 1 MeV triton resulting from D-D fusion is promptly lost in MST's magnetic field. Therefore high energy neutrons resulting from D-T fusion in MST are exceptionally rare and can be neglected [44].

3.2 Neutron Detection Techniques

Neutrons are uncharged and therefore detected indirectly through their interaction with various nuclei. There are two basic classes of available detectors. First, a neutron may scatter off a nucleus, transferring a portion of its kinetic energy. With enough energy transfer, the recoiling nucleus can ionize the surrounding material. This detection technique is only efficient for high energy neutrons interacting with low mass ions and in practice only hydrogen and helium are used. This is the detection method used for MST. The second detection method relies on the neutron having a nuclear reaction. The resulting byproducts such as protons, alpha particles, gamma rays, or fission fragments are then detected. A moderating layer slows the neutrons to increase the relevant cross sections, degrading the temporal resolution making it a less attractive candidate for flux measurement purposes. This method has a high thermal detection efficiency and is often used to measure total flux (dose) in situations where neutron radiation effects on human safety are important.

A wide range of detectors exist in these two categories offering different detection efficiency for high or low energy neutrons, gamma ray sensitivity, cost, etc. In MST, neutron fluxes of up to around 10^{11} s^{-1} are achieved but there also exists a large background of high energy photons created through processes like electron bremsstrahlung (up to $\sim 100 \text{ keV}$), fusion proton induced gammas, and neutron radiative capture. Low energy gammas can be shielded quite effectively with a minimal thickness of lead but the other higher energy mechanisms must be considered. The 3 MeV fusion protons are unconfined by MST's magnetic fields and strike the aluminum vessel wall creating a gamma spectrum up to 10 MeV [45]. Detection of these gammas is related to the neutron flux, but the information is difficult to correlate to the original fusion event. Not only is it temporally decoupled due to the emission

occurring after the original fusion event, it is also spatially uncorrelated as it relates to where the proton collided with the vessel wall instead of where it was born. For a good discussion of neutron detectors the reader is referred to Crane [46].

3.2.1 Scintillation Detectors

MST utilizes a combination of liquid and plastic scintillator detectors to measure neutron flux. Scintillators are often used for fast-neutron detection because of their fast response time (on the order of nanoseconds) and modest cost. A disadvantage is that detection probabilities of neutrons and gamma rays are comparable.

Within the scintillator material, fast neutrons elastically scatter off the nuclei (mostly hydrogen and carbon). In such a collision, the recoiling nucleus will gain an energy:

$$E_R = \frac{4A}{(A+1)^2} \cos^2 \theta E_n \quad (3.5)$$

where A is the atomic mass, θ is the scattering angle of the recoiling nucleus, and E_n is the incident neutron energy. The most efficient transfer of energy therefore occurs for hydrogen where up to 100% of the neutron energy can be transferred. The energy of the recoiling proton is transferred to the surrounding scintillator material, creating an ionization trail that excites fluorescent molecules (most commonly anthracite) which emit photons. The light is collected by a photomultiplier converting it to an electrical pulse.

3.3 MST Global Neutron Diagnostics

Two detectors measure time resolved neutron flux for different operating regimes. Under normal operation with either no neutral beam injection or injection using the deuterium doped hydrogen fuel, a higher sensitivity detector is used (named NLF for “neutron low flux”). At high flux levels the anode current of the PMT for this detector saturates. A second neutron diagnostic has been constructed as part of this research to accurately measure the higher flux levels of full deuterium NBI operation. A pair of scintillator-PMT detectors provide a stable measurement with a linear response over the achievable flux range. The pair of detectors are NMF and NHF (for “medium” and “high flux”), but unless otherwise stated,

a mention of NHF refers to the average of the two. Both NLF and NHF are positioned on the machine midplane about one meter from the vacuum vessel within the same gamma-blocking lead enclosure.

A third tool for measuring neutrons on MST is a ThermoFisher Scientific ASP2(e)/NRD BF_3 “neutron ball” which gives a dosage reading for each discharge. The detector is enriched with ^{10}B in its fill gas (which has a much higher cross section than the more naturally abundant ^{11}B) to improve detection efficiency. As boron has a very low cross section for high energy neutrons, the detector is surrounded by a 23 cm layer of high density polyethylene (HDPE) to slow the neutrons. Detection occurs when a thermal neutron ($E \leq 0.025 eV$) is captured in the reaction:



The resulting recoiling 7Li nucleus and alpha particle travel in opposite directions, depositing their energy into the gas by creating ion pairs. The ionization is collected in the detector as a pulse. This is then converted into a dose measurement to ensure safe radiation levels around the machine. This conversion is a proportionality constant determined in part by the neutron energy and potential damage to living tissue and contains many questionable assumptions, but as specified provides a means of calibrating the two neutron detectors as will be discussed in section 3.3.2 and the Appendix.

3.3.1 Detector Specifications

NLF has a cylindrical Bicron-408 plastic scintillator of 12.7 cm diameter and 12.7 cm length. It’s a polymerized base of polyvinyltoluene doped with anthracene as the fluor molecule with a density of $n_H = 5.23 \times 10^{22} cm^{-3}$ (1:1.104 :: H:C) and maximum emission at $\lambda = 425 nm$. NHF also uses an anthracene doped polyvinyltoluene scintillator with similar properties, cut to dimensions of 4.0 cm diameter and 2.54 cm length. At an energy of 2.45 MeV, neutron collisions with hydrogen have a cross section of 2.5 barns resulting in a mean-free-path of $\lambda_{H-mfp} \approx 7 cm$. The larger volume of the NLF scintillator (and the operating limits of the PMT used) account for the higher sensitivity.

Optical grease is applied to the scintillator/photocathode surface to increase coupling of

the photons to the PMT, and the sides of the NLF scintillator were painted with 3 layers of white reflective paint (Saint-Gobain BC-620) and the bottom covered in aluminum foil. The NHF scintillators have aluminum foil around the sides and bottom.

Light is converted to a detectable signal in the PMT as the scintillation photons strike the photocathode initiating an electron cascade through a series of dynodes held at increasing potentials. The PMT for NLF is a 1.3 cm diameter 10 stage Electron Tubes 9390B. The photocathode is a blue-green sensitive bialkali with peak quantum efficiency of 28% at $\lambda \approx 400 \text{ nm}$. The voltage gain (at a supply voltage of 800 V) is $\sim 10^5$. For NHF, a pair of Hamamatsu R580 PMTs are used. This is a 3.8 cm diameter 10 stage bialkali photocathode PMT with a quantum efficiency of 27% at $\lambda \approx 420 \text{ nm}$, and a gain of 7.9×10^5 at an operating voltage of 1500 V. The dark current in both PMT types is on the order of nanoamps. The bias supply voltage is 800 V, 1100 V, and 1000 V for NLF, NMF, and NHF respectively.

The current pulse from the anode of the PMTs is run through a passive RC integrating circuit with $RC = 30 \mu\text{s}$ for NLF, and $RC = 106, 82 \mu\text{s}$ for NMF and NHF respectively. The signals are then digitized at 100 kHz and written to `\mraw_misc::nlf`, `\mraw_misc::nmf`, and `\mraw_misc::nhf`.

All three PMTs have mu-metal layers to provide magnetic shielding and are in a $\frac{1}{4}$ " steel enclosure for electrostatic shielding. An additional 4" of lead surrounds the detectors providing 4π radiation protection against MST plasmas' significant high energy photon levels (both x-rays and γ -rays). Even in the presence of high photon energy radiation the lead reduces the gamma flux by around 99.97%. NLF and NHF are both operated in current

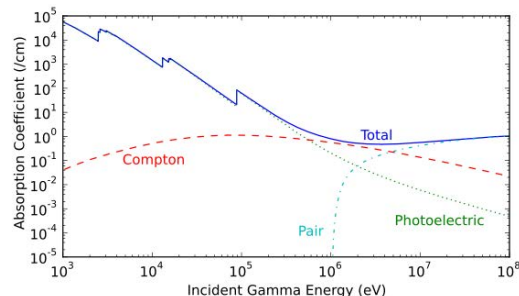


Fig. 3.2: Absorption coefficient versus energy for Lead

mode, where the signal level is proportional to the neutron flux¹.

3.3.2 Global Neutron Detector Calibrations

Neutron detectors are notoriously difficult to calibrate. Energy resolution is lost (or at least difficult to retain) between the neutron collision and conversion to scintillation photons, and neutron source strengths are inherently imprecise. The detection efficiency is also strongly dependent upon the neutron energy, and scatter and secondary radiation detection are ubiquitous. While lead does very little to change the neutron energy, it is still a fairly effective neutron diffusor so the inclusion of a 4" lead shield further complicates the process.

NLF has been in use for a number of years and as such, has undergone several calibrations. Calibration using a small neutron source (7×10^9) [2], an NBI beam-blip experiment (7.4×10^9) and an estimate based upon detector quantities (1.1×10^{10}) [44] give reasonably good agreement and result in a working calibration factor of $cf_{MST} = 7 \times 10^9$ neutrons/sec/Volt where the MST subscript implies a conversion to total MST flux (instead of flux detected or flux at the detector).

In order to obtain a calibration factor for NHF, the beam-blip experiment is mimicked by analyzing the first few milliseconds of neutral beam injection. Keeping the time window short ensures that the assumption of monoenergetic beam ions is still reasonable and also prevents the beam ion population from growing large enough to perturb the plasma equilibrium quantities. The detector output voltage is compared to the computed MST flux. An accurate prediction of the neutron flux requires knowledge of the fast-ion source to the plasma.

Around a 56% fraction of the measured ion current is realized as fast ions in the plasma after accounting for neutralization in the beam cell (87%), the full energy fraction component (90%), and the ionization fraction (although sensitive to beam energy, plasma temperature and density, around 70%). The total fast-ion content is computed by the time-average of

¹ While it is possible to operate in counting mode, this requires the time between pulses to be much longer than the pulse width. Due to the long RC times and high flux environment, both detectors are well beyond the counting mode regime. The pulse height of an individual neutron interaction is determined by the recoil proton energy which is a random fraction of the neutron energy determined by the scattering angle (or impact parameter in the hard-sphere collision analogy). The pile-up of these pulses allows each detectors signal to be interpreted as a neutron flux using a single calibration factor per detector.

the beam current through the ramp up phase (Figure 3.3)

$$N_{fi} = \frac{\langle I_{NBI} \rangle f_{conv} \tau_{win}}{e} \quad (3.7)$$

$$\Gamma_{neut} = \sigma_{DD} v_{fi} N_{fi} n_i \quad (3.8)$$

where N_{fi} is the total fast-ion content, $\langle I_{NBI} \rangle$ is the average NBI current during the beam-blip, f_{conv} is the conversion fraction giving the percent of the ion current that become fast-ions in the plasma, and τ_{win} is the time window duration. These fast particles are monoenergetic

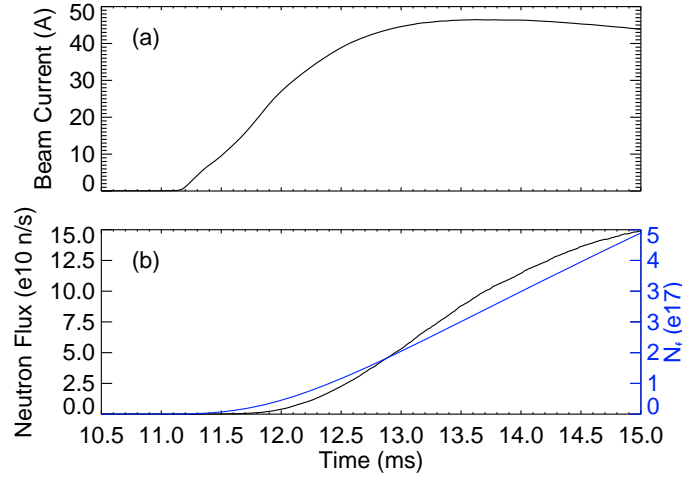


Fig. 3.3: The initial beam current ramp up (a) leads to an increasing number of fast-ions and fusion rate (b) in MST

and have a confinement and slowing down time much longer than the experiment. The flux is computed using the D-D fusion cross section σ_{DD} , evaluated at the fast-ion velocity v_{fi} , and depends on the fast-ion content as well as the bulk ion density n_i . The bulk ion density profile is relatively flat in the core, but a large uncertainty persists due to an unmeasured Z_{eff} . The main impurities in MST are carbon, boron, oxygen, nitrogen, and aluminum, the concentrations of which have large impacts on Z_{eff} . Here we use $Z_{eff} = 3 \pm 1$ and an impurity content such that $n_i/n_e = 0.8 \pm .15$ which covers the range of values typically used in MST. It is worth noting that the computed flux levels are a negligible fraction of the total fast-ion content so consideration of fast-ion losses due to fusion during the time window can

be ignored.

A calibration factor for each detector is computed by comparing the total neutron flux and the detector voltage at the end of a chosen time window. A calibration of NLF using this technique is included to benchmark this method against previous calibrations. Shown in Figure 3.4 are the results of this analysis. A fit to this data gives calibration factors for the three detectors

$$cf_{NLF} = 6.6 \pm 1.2 \times 10^9 \text{ s}^{-1} \text{ V}^{-1} \quad (3.9)$$

$$cf_{NMF} = 1.9 \pm 0.4 \times 10^{10} \text{ s}^{-1} \text{ V}^{-1} \quad (3.10)$$

$$cf_{NHF} = 3.0 \pm 0.6 \times 10^{10} \text{ s}^{-1} \text{ V}^{-1} \quad (3.11)$$

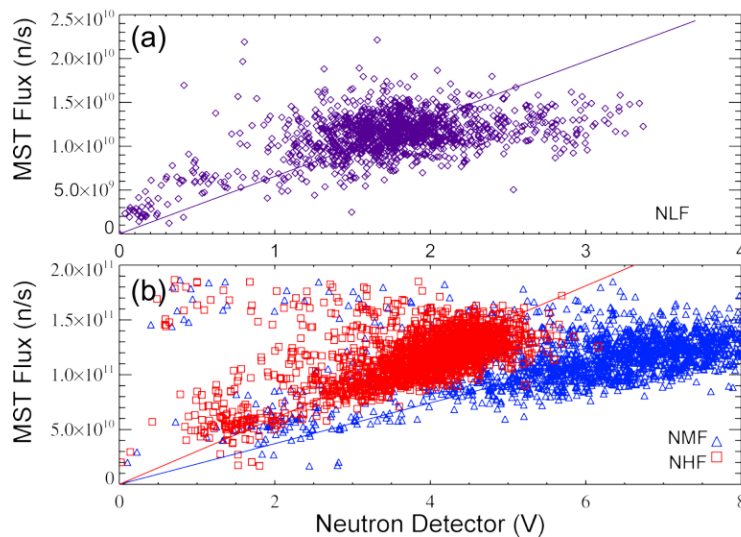


Fig. 3.4: Calibrations based on a beam-blip type method for (a) NLF using mixed fuel (5% deuterium) NBI discharges and for (b) NMF and NHF using full deuterium discharges.

The inherent difficulty in calibrating neutron detectors motivates multiple, independent calibrations. The BF_3 “neutron ball” enables an independent absolute calibration subject to a handful of assumptions, and the result is subject to the accuracy of the neutron ball’s own calibration, $0.552 \mu\text{rem}/\text{count}$, last performed May 15, 2015 at Thermo-Fisher Scientific. The calibration technique and details about count rate to dose conversion are given in the Appendix.

Shown in Figures 3.5a and 3.6 are the integrated detector signals versus neutron ball readings. For NLF, an initial linear response soon saturates at higher flux levels due to anode current limitations. NLF is reliable only below a flux level of $1.7 \times 10^{10} n/s$ (where $n/s = \text{neutrons/sec}$). Linear fits, using the dose to count rate approximation in the Appendix result in calibrations for each detector of

$$cf_{NLF} = 2.56 \times 10^9 \frac{n/s}{V} \quad (3.12)$$

$$cf_{NMF} = 1.33 \times 10^{10} \frac{n/s}{V} \quad (3.13)$$

$$cf_{NHF} = 1.82 \times 10^{10} \frac{n/s}{V} \quad (3.14)$$

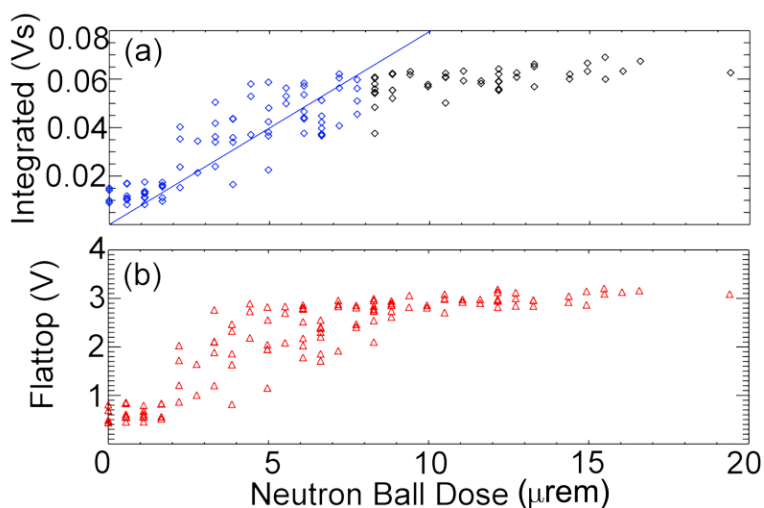


Fig. 3.5: NLF comparison to neutron ball. (a) integrated signal versus dose gives scaling, calculated for blue points to avoid saturated anode signal. (b) flattop averages indicate upper detector operating limit of 2.5 V

Given the reasonable agreement between the calibrations found for NLF between the calculated beam-blip analysis, neutron ball, and prior attempts at calibration, it is justifiable to assume that the calibrations found for NMF and NHF using the beam-blip calculation are also valid and we proceed using these results. In order to determine an upper operating limit for NLF it is helpful to compare the average flattop voltage of the neutron signal to the neutron ball dose. As shown in Figure 3.5b, saturation of the signal occurs rather abruptly above a voltage of around 2.5 V. Utilizing the calibration for NLF this corresponds to an

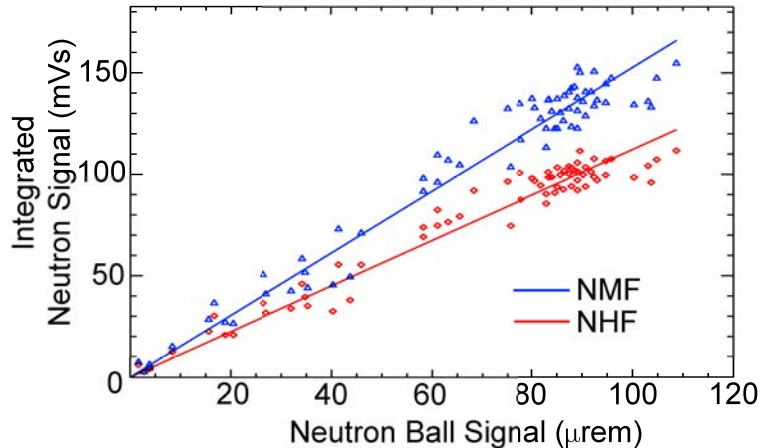


Fig. 3.6: NMF and NHF integrated measurements versus neutron ball dose rates. Both detectors show good linear behavior over entire achievable MST flux range.

upper operating flux level of $1.7 \times 10^{10} n/s$. NMF and NHF have upper operating limits of 1.9×10^{11} and $3.0 \times 10^{11} n/s$ respectively, based on a 10 V data recording limit.

3.3.3 Summary of Scintillator-Based Neutron Detectors

Two diagnostics have been established to measure both the lower flux regime (no NBI or mixed-fuel NBI), and the higher flux levels produced by deuterium NBI. These detectors are all scintillator-PMT setups which have the fast time response and low cost necessary to be viable flux diagnostics. The lower flux detector is calibrated to $6.6 \pm 1.2 \times 10^9 n/s/V$ with an upper operating flux limit of $1.7 \times 10^{10} n/s$. The calibration factors of the two detectors that comprise the higher flux diagnostic are $1.9 \pm 0.4 \times 10^{10} \frac{n/s}{V}$ and $3.0 \pm 0.6 \times 10^{10} n/s/V$ for NMF and NHF respectively with upper operating flux limits of $1.9 \times 10^{11} n/s$ and $3.0 \times 10^{11} n/s$. Both detectors for the high flux diagnostic were shown to have good linear behavior over the achievable range of flux levels.

3.4 Collimated Neutron Detector (CiNDe)

This thesis relies on measurement of the fast-ion density profile through a spatially resolved neutron detection diagnostic. The final design of a directionally insensitive detector embedded within a neutron shield with a viewing aperture is shown in Figure 3.7.

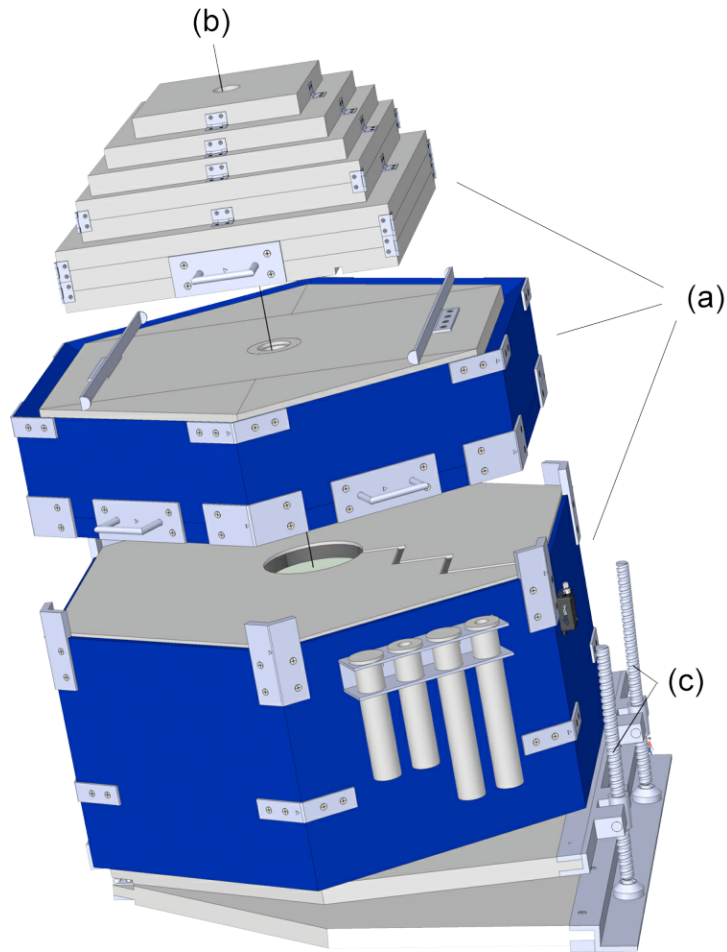


Fig. 3.7: CAD model of final design of collimated neutron detector (CiNDe). Three detachable stages (a) allows for easier movement around machine area. A 5.1 cm diameter and 92 cm bore (b) defines the plasma viewing volume which is scanned across the poloidal cross section of the machine by adjusting the inclination of the baseplate using a dual worm-screw jack system (c).

3.4.1 Modeling

Neutrons have no charge and therefore do not experience Coulomb forces as they travel through matter. Interactions, especially at high energy, are dominated by elastic scattering allowing them to travel long distances unimpeded. While this characteristic removes the need of a port hole to make neutron flux measurements, it necessarily means that shielding to provide a defined viewing volume is quite burdensome.

One of the concerns in neutron shielding is the energy distribution of the impeding flux. Neutrons in polyethylene have a mean free path of roughly 5 cm at 2.45 MeV, but this falls off rapidly with energy as the scattering and absorptive cross sections become larger. A Monte Carlo type code called MCNP [47] was used to model the neutron transmission through a slab of PE, as shown in Figure 3.8. The results show that as the shielding thickness is increased the number of uncollided neutrons drops while a population builds at the lowest energy with a relatively flat profile between the two extremes. This makes intuitive sense if we consider a population of collimated neutrons traveling through numerous layers of shielding. Initially a monoenergetic group, their mean-free-path determines that a certain percentage of them will have a collision in the first layer. Considering only singular collisions with hydrogen, we have a population still at full energy and another population that has between 0-100% of their initial energy depending on their random scattering angle, producing a flat energy distribution from 0-2.45 MeV. Passing through the next layer of shielding, the same process repeats; for the population at full energy, some remain uncollided while others scatter and contribute to the flat energy profile. For the population that has already had one collision, their probabilities of having another in the subsequent layer vary, with those at lower energy having higher probabilities of colliding again. Therefore the number of thermal neutrons grows, connected to an ever reducing number of full-energy neutrons by a relatively flat distribution. The inclusion of carbon along with other nuclear interaction mechanisms complicates the picture, but this simple picture is sufficient to explain the behavior seen in Figure 3.8. Beyond a shielding thickness of ~ 30 cm the unwanted background neutron flux is dominated by thermal neutrons.

Some optimization of the scintillator is possible to further enhance the neutron signal

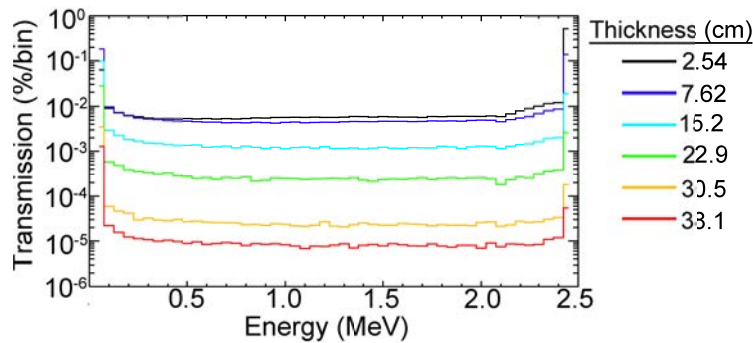


Fig. 3.8: MCNP simulation showing neutron energy spectrum after PE slab transit versus slab thickness

from the plasma viewing volume over the background neutron flux. A scintillator long along the direction of preferred neutron detection provides a larger likelihood of incurring a reaction. However, a longer scintillator also provides a larger perpendicular cross section thereby increasing the likelihood of detection of shield-penetrating neutrons as well. To address this, a Monte Carlo type neutron following code was developed (similar to MCNP) to optimize the scintillator design characteristics. The code uses a model of appropriately weighted abundances of carbon and hydrogen and the appropriate cross sections for elastic scattering and absorptive processes obtained from the Evaluated Nuclear Data File [48]. The scintillator in use is polyvinyl toluene ($C_{27}H_{30}$) doped with anthracene ($C_{14}H_{10}$). The energy transferred to the scintillator (i.e. lost by the neutron) was taken to be a good proxy for the signal level expected. The goal is to identify scintillator geometries that would make it more likely for a neutron originating from along the scintillator axis to be detected than for one entering the scintillator from a direction perpendicular to the axis.

A simulation measuring the average energy deposited in the scintillator for axial vs. shield-penetrating neutrons for various scintillator geometries is shown in Figure 3.9 where $Directionality = \log \left[\frac{\langle E_{dep} \rangle^{axial}}{\langle E_{dep} \rangle^{radial}} \right]$, the ratio of the average energy deposited per neutron in the axial or radial direction, with higher values associated with a scintillator more sensitive to neutrons originating along the axis. Directionality can be improved by reducing the diameter (at the expense of overall signal) or increasing the scintillator length. Optimization of the dimensions is performed within the constraints of the open volume inside the shielding. A 3.8 cm diameter, 15.24 cm long Saint Gobain BC-501A liquid scintillator with a type MAB-1

cell was chosen for its fast neutron detection properties.

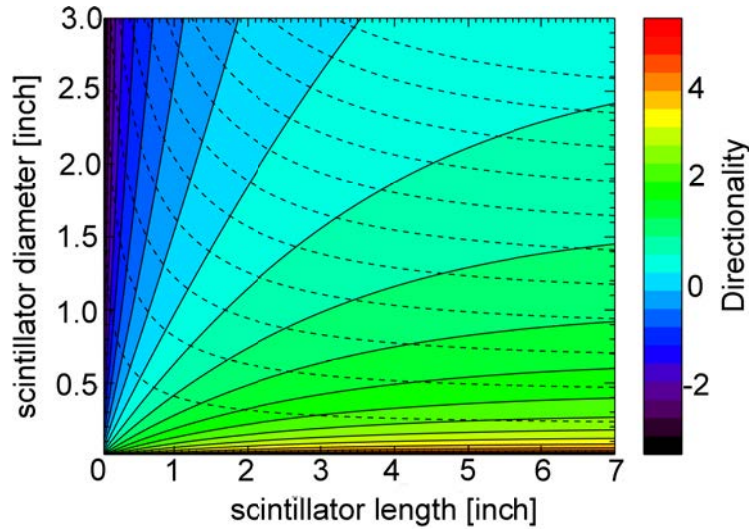


Fig. 3.9: Directional sensitivity versus scintillator dimensions. Dashed lines show lines of constant signal level

3.4.2 Detector Design

In the design of an effective collimated neutron detector, two key aspects must be considered. First, the detector must have adequate time and energy response to operate appropriately in the expected radiation field. Second, adequate shielding must be in place around the detector to define a plasma viewing volume. This viewing volume must be of proper size to allow for a measure of the neutron emissivity to be made while still keeping the detector signal at a reasonable level above the background. This background radiation consists of fusion neutrons outside of the plasma viewing volume as well as a large gamma radiation field. Shown in Figure 3.10 and summarized in Table 3.1 are the cross sections and mean-free-paths of the two types of radiation through relevant materials.

Range (cm)	Polyvinyl Toluene (scintillator)		
	Aluminum	Lead	
n	7.95	4.22	3.72
γ	8.56	1.91	23.1

Tab. 3.1: Neutron and gamma mean-free-paths through materials at 2.45 MeV

Consider first the neutron shielding. In order to obtain a spatially resolved neutron

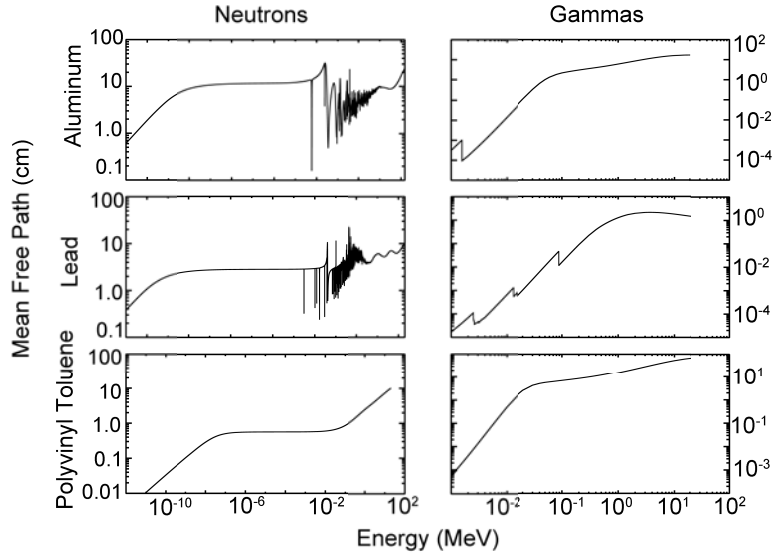


Fig. 3.10: Neutron and gamma mean-free-paths versus energy for various materials.

emission measurement, sensitivity must be reduced to neutrons originating from outside the plasma region of interest. Energy is transferred through elastic collisions to the recoiling nucleus as in Equation 3.5 which is plotted in Figure 3.11 for hydrogen and carbon. Collision with hydrogen includes transfer up to 100% of the neutron’s energy (compared to a maximum of 28.4% for ^{12}C), so given a random scattering angle a neutron will transfer 50% of its energy per collision on average. The implication is that 2.45 MeV D-D fusion neutrons will require 27 collisions on average to drop to “thermal” levels ($\lesssim 0.025$ eV).

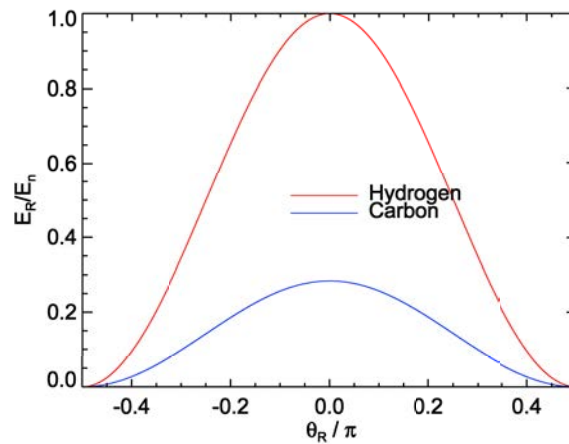


Fig. 3.11: Energy transfer ratio versus recoil scattering angle.

To provide the necessary thickness of shielding while maintaining mobility, CiNDe was

constructed in three separate stages as shown in Figures 3.7,3.12. The bottom stage consists of a hexagonal array of eighteen 46×19 cm diameter HDPE cylinders enclosed by 3.8 cm thick HDPE walls with gaps filled with paraffin wax (Figure 3.13). The center cylinder was removed and replaced by a copper sheath to provide a central cavity in which to house the neutron detector. This cylindrical array was mounted on a base plate of two HDPE plates hinged together on one edge and featuring a dual worm-screw jack on the side opposite the hinge. The jack allows the three stages to be inclined up to 15° thereby altering the plasma viewing volume defined by the collimating bore of the top two stages. The bottom of the lower baseplate is outfitted with seven ball transfers which provides a low profile means of moving CiNDe around the MST machine area.

The top two stages are a pyramid stack and hexagonal stack of HDPE with a 5 cm bore through the center. Each stage is outfitted with pairs of handles providing access to the detector region through removal of the stages. The depth (55 cm) and bore diameter (5 cm) define a 1.6° cone half angle for the device. CiNDe was positioned as far underneath the MST vessel as the presence of other diagnostics would allow and the scan of the poloidal cross section was achieved by altering the baseplate inclination alone (see Figure 2.2). Neutrons that are emitted from the plasma volume can scatter off the concrete floor of the MST machine area and register in the detector if directed towards the underside of CiNDe while inclined. To counteract this, a 7.5 cm HDPE disk was placed at the bottom of the central cavity. This was found to be sufficient to reduce backscatter signal to negligible levels.

The next thing to consider is the gamma radiation field of the detector. As discussed above, the proton branch of the fusion chain releases 3.01 MeV protons which promptly strike the wall and release gammas isotropically. These gammas are somewhat attenuated by the 5 cm aluminum vacuum vessel (Figure 3.14), but a certain percentage persist, especially those at higher energies. Another source of gamma radiation to the detector is that of neutron capture. As neutrons slow in the shielding material their cross-sections for elastic scattering decrease while other cross-sections grow. Neutrons themselves are unstable and will eventually beta-decay into a proton, releasing an electron and electron antineutrino in the process. The free neutron half-life however, is on the order of 15 minutes. This means that as a neutron scatters around in the shielding material, it will do so until it eventually

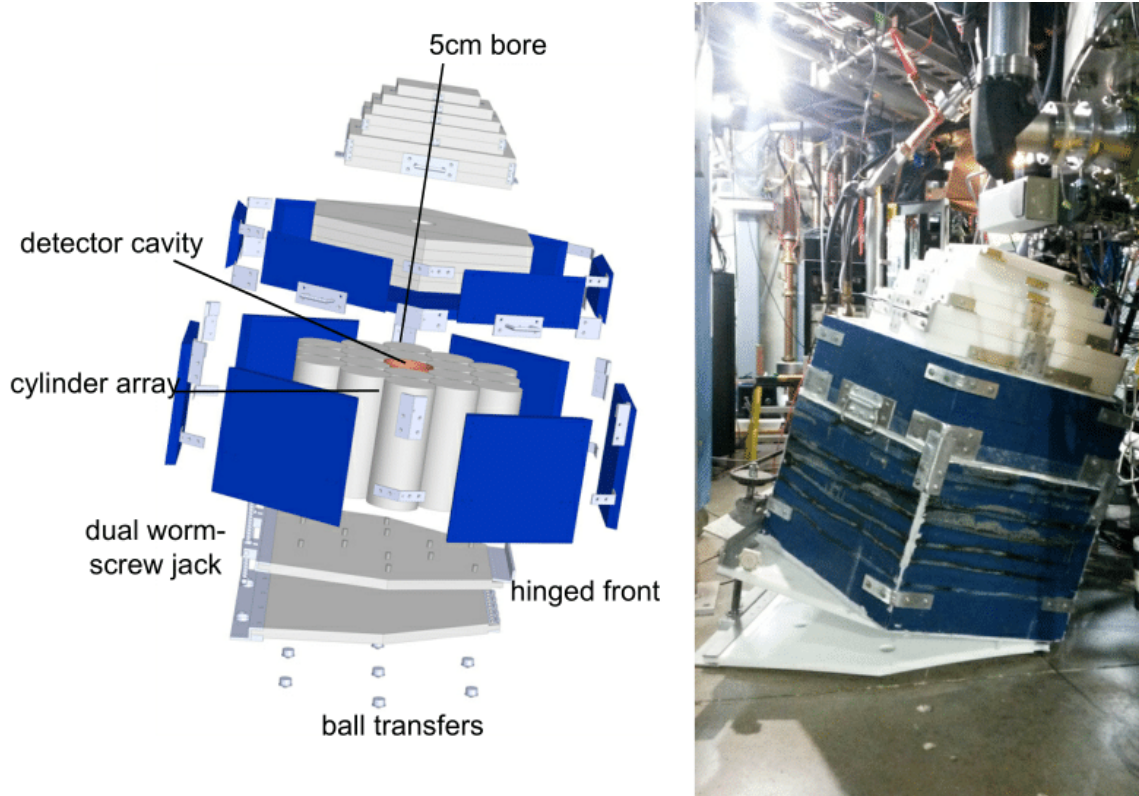


Fig. 3.12: CiNDe: Exploded view of CAD model (left) and photo of diagnostic in place beneath MST (right).

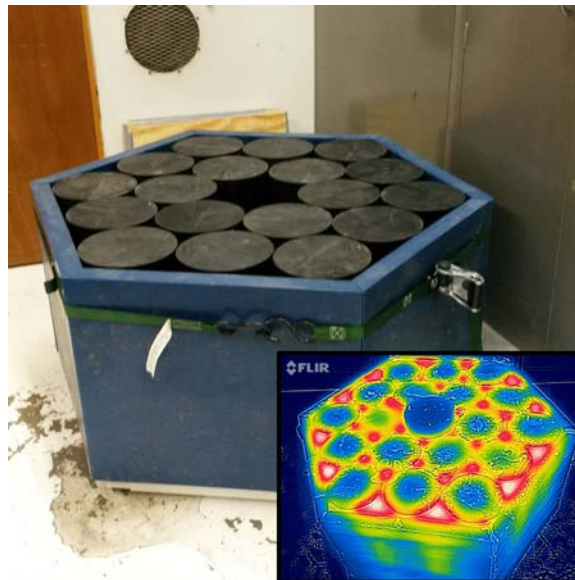


Fig. 3.13: Construction of the lowest stage of CiNDe. An array of HDPE cylinders provides the bulk of the shielding. The gaps between cylinders and walls were filled with paraffin wax. Inset: IR image following wax pour.

combines with a nucleus. In the case of capture by hydrogen, this results in the emission of a 2.224 MeV gamma [49]. To limit the influence of this background on the detector signal level, cylindrical lead bricks were cast having an outer diameter of ~ 18.4 cm with a central hole roughly 5 cm diameter to accommodate the PMT/scintillator detector (Figure 3.15).

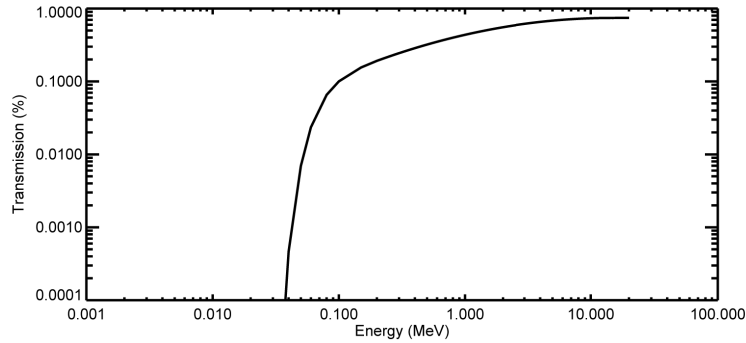


Fig. 3.14: Gamma transmission through 5 cm MST vessel versus energy.

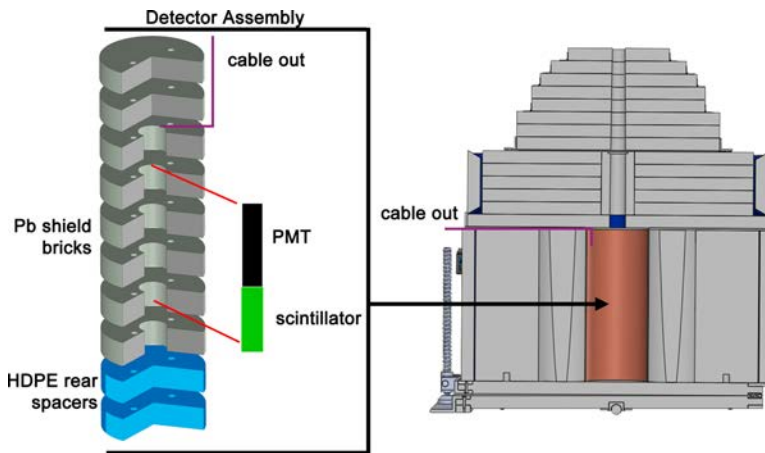


Fig. 3.15: Exploded view of CiNDe's neutron detector stack. The PMT/Scintillator are situated within a stack of cylindrical lead bricks to reduce gamma signal levels and set atop a HDPE spacer to reduce neutron backscatter from the surrounding lab space. Cables are fed through the top of the stack and out below the removable CiNDe stages.

3.4.3 Pulse Identification

A signal is detected and recorded by the following process: A fast-ion fuses with a bulk ion in the plasma, emitting a neutron (half of the time and in a random direction). The

2.45 MeV neutron passes directly through the Al vessel 53% of the time². If the fusion event occurred within the CiNDe viewing volume and the neutron was directed towards the scintillator, the neutron will pass down the CiNDe collimator bore and enter the scintillator.

Shown in Figure 3.16 is representative raw data taken as part of the datasets discussed in Chapter 5. A DC offset of 1 V was included to limit saturation of the preamplifier around ± 1.3 V. The PMT was operated with a bias setting that ensured pulse pile-up occurred as a negligible fraction of the recorded pulses. As can be seen in Figure 3.16, ample spacing typically exists between pulses.

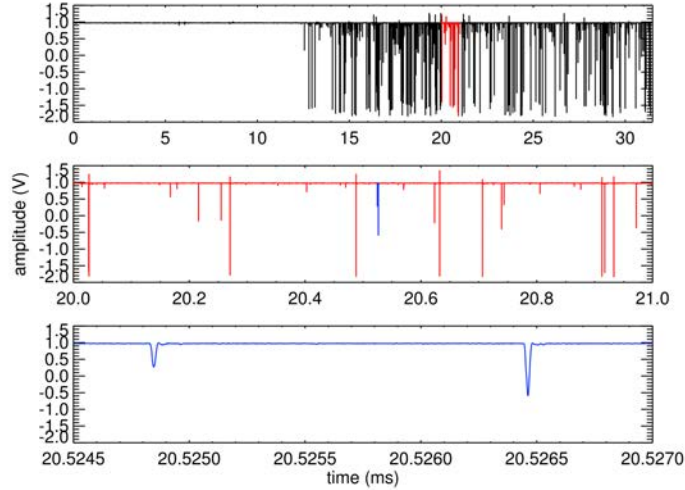


Fig. 3.16: Raw CiNDe signal at various zoom levels. Large count rate as expected during NBI, but well below level where pulse pile-up is a concern.

A pulse-finding algorithm, based on the “automatic multiscale-based peak detection” (AMPD) method [50], identifies the time stamp of each count for further analysis. Given a time series D , a large 2D matrix \mathbf{M} is created where the element M_{ij} corresponds to the i^{th} datapoint and value based on the time window width $2j$.

$$M_{ij} = \begin{cases} 0 & \text{if } D_{i\pm j} < D_i \\ 1 & \text{otherwise} \end{cases} \quad (3.15)$$

² From Table 3.1 a 2.45 MeV neutron has a mean-free-path in aluminum of $\lambda_{mfp} = 7.95$ cm. The uncollided percentage after passing through 5 cm of Al is then $\Gamma/\Gamma_0 = \exp(-5/7.95) = 0.53$

If W is the number of time windows considered for an N element data series, \mathbf{M} becomes an $N \times W$ matrix. For each time window $w \leq W$ the local maxima are determined by summing columns of M creating an array γ_w such that $\gamma_i = \sum M_{i,0:w}$. The local maxima for this time window is then given by the indices where $\gamma_w = 0$. An optimum time window is then identified based on which time window gives the largest number of local maxima. This algorithm provides a robust way to identify semi-periodic pulses in noisy datasets, but in practice is very computationally intensive. A maximum time window of 50 ns was chosen for CiNDe data analysis as it resulted in both effective peak identification and reasonably fast computation times.

Background signal reduction using pulse-shape discrimination was being investigated during the accumulation of data presented in Chapter 5. For this reason, a PMT bias setting of 600 V was used to prevent an appreciable fraction of the pulses from saturating the preamplifier, thus preserving pulse shape. Concurrently, a ^{137}Cs gamma radiation source was used to investigate pulse amplitudes at various PMT bias settings (^{137}Cs has a strong emission peak at 700 keV). It was found that for a bias setting of 800 V, the 700 keV peak coincided with a pulse amplitude of $\lesssim 1$ V. After resolving to use differencing techniques to determine the neutron emission rate, the need for pulse shape analysis was removed and only pulse identification was necessary. Therefore later data was collected with a PMT bias voltage of 800 V. This allowed for pulse *amplitude* discrimination wherein pulses below 2 V (attributed to low energy γ s and thermal neutrons) were removed.

Differencing techniques are used to measure CiNDe neutron count rates. For this measurement technique, we consider four radiation quantities; background neutrons, background gammas, target volume neutrons, and target volume gammas (where “target volume” refers to CiNDe’s volume). To eliminate target volume gammas from the signal, a 5×5 cm diameter lead slug is placed at the bottom of the collimator bore directly adjacent to the detector. To measure the background count rate (background neutrons + background gammas), a 5 cm diameter HDPE bore plug is inserted into CiNDe (filling the collimator volume) and a large number of discharges are recorded building a “closed-bore” dataset. The bore plug is then removed and an “open-bore” dataset (background neutrons + background gammas + target volume neutrons) is built with the same plasma parameters. The difference in measured

count rates gives the target volume neutron count rate. While this technique demands large datasets to produce reliable count rate differences, it has been successful in producing the first fast-ion profiles in MST, shown in detail in Chapter 5.

4. FAST ION DYNAMICS IN MST

Considerably different dynamics are observed in the bulk and fast-ion populations of MST plasmas. In this chapter we begin in Section 4.1 with a brief overview of magnetic stochasticity in MST and how it relates to thermal particle confinement. Section 4.2 then summarizes what is known about fast-ion confinement in MST for various injection geometries. Perhaps surprisingly, the fast ions are only weakly affected by the chaotic underlying magnetic field and instead approach the limit of classical confinement, explained in Section 4.3 using the concept of a fast-ion q . The conditions for EPM growth are discussed in Section 4.4. Full orbit tracing in the RFP magnetic field illustrates the in-surface guiding center drift and helps identify particles resonant with observed Alfvénic perturbations. The evidence for an EPM-limited fast ion content is in Section 4.5 before a summary in Section 4.6.

4.1 *Magnetic stochasticity and thermal confinement*

The equilibrium magnetic field can be written as $B = (0, B_\theta, B_\phi)$ where θ and ϕ respectively refer to the poloidal and toroidal directions. While this is useful for a general description of the plasma, stochastic fields exist due to time-varying perturbations caused by multiple closely spaced tearing modes, driven by gradients in J_\parallel . We can write these perturbations generally as a Fourier series

$$\tilde{B}(r, t) = \sum_k \tilde{B}_k(r) e^{i(\mathbf{k} \cdot \mathbf{r} - \omega t)} \quad (4.1)$$

with the wave vector \mathbf{k} defined using the poloidal and toroidal mode numbers m and n as $\mathbf{k} = (k_r, m/r, n/R)$. These perturbations can grow at q -rational surfaces where the wave vector is perpendicular to the equilibrium magnetic field (Eq. 2.3). At these radial locations, standing-wave like perturbations can grow giving rise to so-called “magnetic islands.” An example

representative of the plasmas studied herein is shown in Figure 2.4 where the $(m, n) = (1, 5)$ is the core-most resonant tearing mode. The radial width of the dominant $m = 1$ islands that form can be approximated as [51]

$$w_{1,n} = 4\sqrt{\frac{\tilde{b}_{rn}}{B_\theta(r_s)} \frac{r_s}{nq'(r_s)}} \quad (4.2)$$

and depends upon the magnitude of the radial magnetic field fluctuation \tilde{b} as well as the shear in the field line pitch at the rational surface $q'(r_s)$. Overlaid on Figure 2.4 are the approximate island widths at the rational surfaces which reveals large overlap of the islands. The field lines in these regions can break and reconnect, destroying any original well-ordered flux surfaces and causing them to become stochastic [52]. This presents conditions for rapid particle and energy transport resulting in typical MST thermal confinement times of approximately 1 ms [53].

4.2 Fast-ion confinement

The MST neutral beam injector is routinely operated at an injection energy of $E_f = 25$ keV, introducing deuterium neutrals into the vacuum chamber at speeds of $v_f = 1.55 \times 10^6$ m/s. Ionizing with the background plasma either through ion or electron impact or charge exchange, this newly formed fast-ion population experiences near classical confinement despite the underlying stochastic magnetic field.

Once ionized within the plasma, an ion will be subjected to Lorentz forces that result in the ion gyro-orbit motion around the magnetic field lines. The Larmor radius measures the size of these gyro-orbits

$$\mathbf{F} = q\mathbf{v} \times \mathbf{B} = \frac{mv_\perp^2}{r} \hat{r} \quad (4.3)$$

$$r_L = \frac{mv_\perp}{qB} \quad (4.4)$$

Due to the dependence on v_\perp , the ion velocity perpendicular to the field, Larmor radii vary widely depending on the ion's initial pitch ($v_\parallel/|v|$) and local magnetic field strength.

Typical orbit sizes for beam ions range from 1-2 cm near the core where the field is strongest (~ 0.4 T), to upwards of 15 cm near the edge. The ions follow helical orbits around the machine, interacting with the background plasma through Coulomb collisions and, in the absence of loss, gradually thermalize. Typical MST parameters result in a fast-ion slowing down time of around 20 ms.

Substantial guiding center drifts result in fast ions in the plasma that execute a wide variety of orbit types depending upon their pitch. Perpendicularly oriented neutral beams result in very low pitch fast ions as the radial beam velocity is nearly perpendicular to the magnetic field along the entire beam path, resulting in “trapped” particle orbits that precess around the machine. By contrast, neutral beams that inject tangentially to the magnetic field (like MST’s) often result in large populations of high pitch fast ions due to a large amount of beam ionization occurring near the core where the beam velocity and magnetic field are nearly parallel, producing a large population of “passing” fast ions on helical orbits. It is known that in tokamaks there exist large loss regions in particle phase-space due to prompt loss as well as large ion drift velocities [54]. The analysis of orbits in MST reveals much smaller loss regions, due primarily to orbits striking the vessel wall within a gyro-orbit [55] (Figure 4.1).

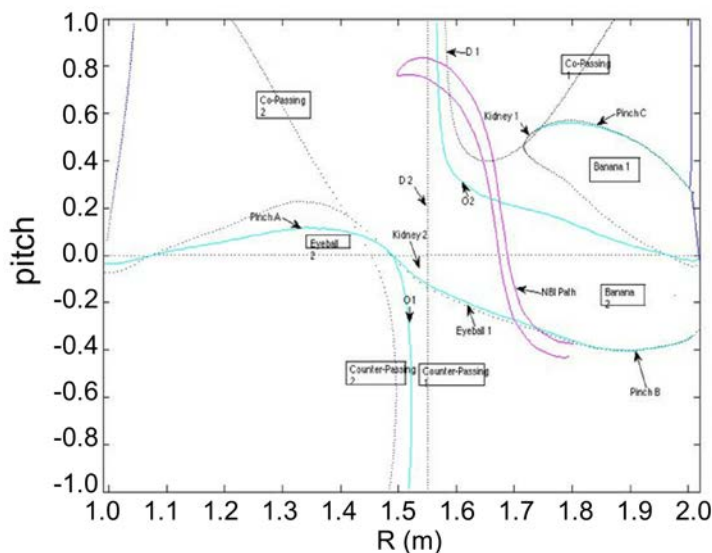


Fig. 4.1: Orbit topology in MST reveals low orbit loss and prevalence of co-passing NBI orbits.

The first measurement of fast-ion confinement time in MST was done in 2006 using a

20 keV Deuterium neutral beam (prior to the installation of the 1 MW NBI system installed in 2009 used in this thesis). Using a beam-blip technique to introduce a non-perturbative population parallel to the plasma current, the fast-ion confinement time was measured by monitoring the decay rate of the neutron flux [2]. Figure 4.2 highlights the results of this study. During the NBI-on phase shown in gray, a linear increase in neutron emission reflects the growing fast-ion population in the core. After beam shut-off the fast-ions experience a confinement time of roughly $\tau_f = 20$ ms, near the classical limit as shown by the $\tau = \infty$ curve. This experiment was repeated for a counter-injection geometry by reversing the plasma current, and also for radial neutral beam injection by using the diagnostic neutral beam system. The result of these studies give a fast-ion confinement time of 4 ms for counter-injection and 18 ms for radial injection. Subsequent studies of fast-ion confinement done via beam-blip experiments with the 1 MW NBI confirm long confinement times for co-injected particles over a wide range of MST operating parameters [3], as shown in Figure 4.3.

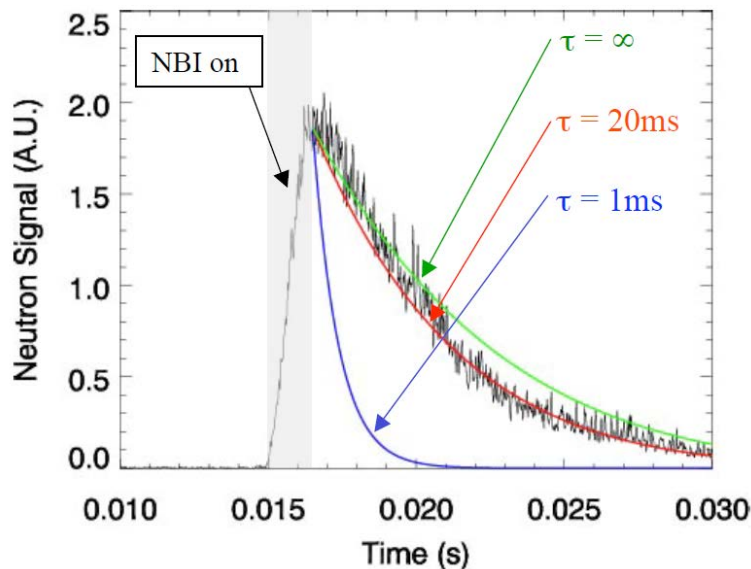


Fig. 4.2: Beam-blip experiment showing fast-ion confinement times of roughly 20 ms [2]

In certain discharges, MST plasmas spontaneously self-organize into a 3D state known as quasi-single helicity (QSH) [56] wherein the magnetic topology of the core becomes helical in nature as depicted in Figure 4.4. Transition to this state is revealed by a sudden dominance of one mode and a reduction in strength of the other edge-measured magnetic modes. Again using a beam-blip method, fast-ion confinement times were measured throughout discharges

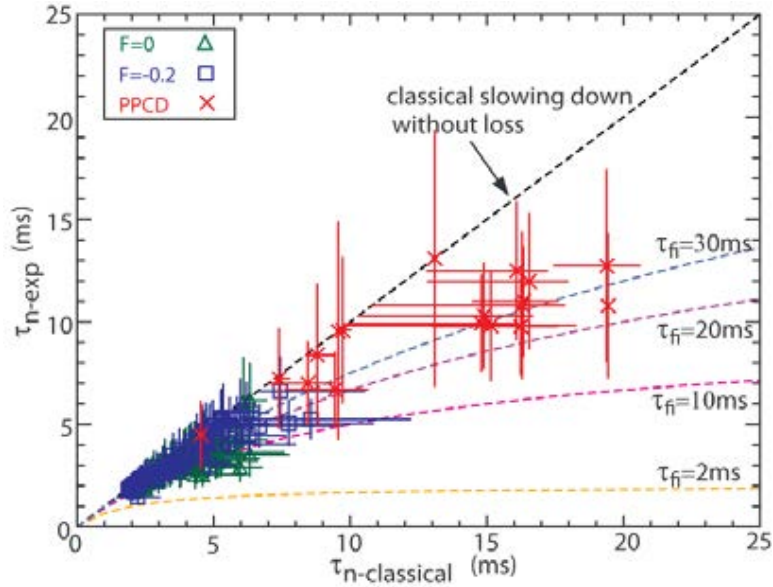


Fig. 4.3: Beam-blip experiment with 1 MW NBI reveals near classical confinement of co-injected ions[3]

where the plasma snapped into and out of the QSH state. As shown in Figure 4.5, as the plasma enters the QSH state (represented here by a higher $n = 5$ fluctuation amplitude) the co-injected fast-ion confinement time degrades from upwards of 20 ms down to near the levels of counter-injected ions. This lower confinement time is also reflected in ANPA measurements that show a rapid drop in signal at the onset of QSH [57].

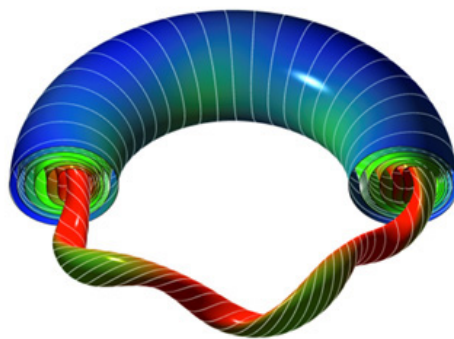


Fig. 4.4: Modeling depicting $n = 5$ QSH state

The specifics of QSH and the transitions in and out of this state are not the focus of this research, but a consideration of this phenomenon is relevant. It has been shown that NBI lowers the core-most resonant tearing mode amplitude and tends to suppress transitions

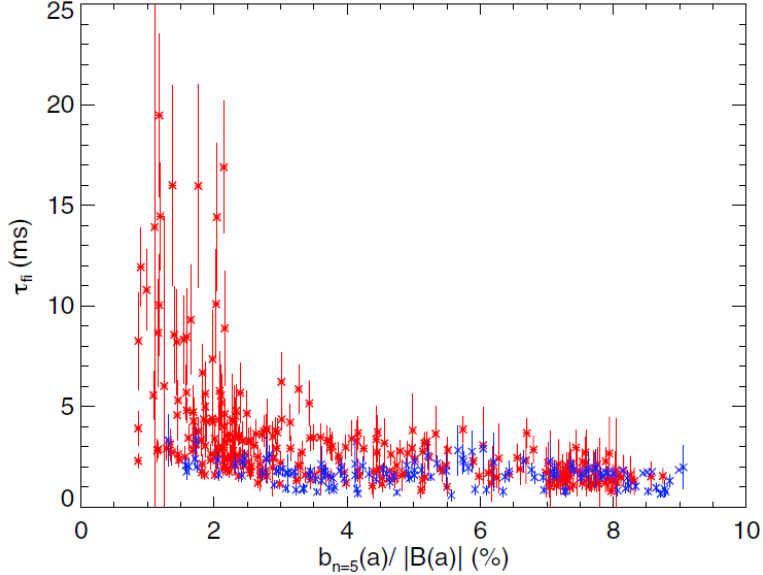


Fig. 4.5: Fast-ion confinement times plotted against the $n=5$ fluctuation amplitude showing degradation of fast-ion confinement to thermal levels in QSH plasma. Red points are for co-injected ions, blue for counter-injection

to QSH [57]. Two competing processes influence the fast-ion distribution in experiment. First, a large tearing mode tends to reduce fast-ion confinement (full transition to QSH not necessary). Conversely, a large fast-ion population tends to suppress the core tearing activity.

4.3 Fast-ion q

Consider the major sources of drift motion in MST, the ∇B and curvature drifts (the $E \times B$ drift has a much smaller effect on the orbital motion). In tokamaks, the magnetic field has a $B \propto R^{-1}$ character, leading to vertical drift vectors. Particles may average out this drift during the orbital motion, but the drift has the effect of moving particles between flux surfaces. In MST, however, the magnetic field gradient and curvature vector are dominantly in the minor radial direction leading to drift orbits that keep particle motion *on* a flux surface¹. This is visualized in Figure 4.6 where a portion of the MST vessel is shown for scale, and a magnetic field line on the $q = 1/5$ rational surface is shown in black at a radial

¹ This is not the case for QSH where a large helical perturbation leads to ∇B and curvature deviating from a flux surface leading to the poor confinement observed

location of $r/a \cong 0.2$. The fast-ion guiding center follows the red curve, deviating from the magnetic field line due to the ∇B and curvature drift motion while staying on the same flux surface.

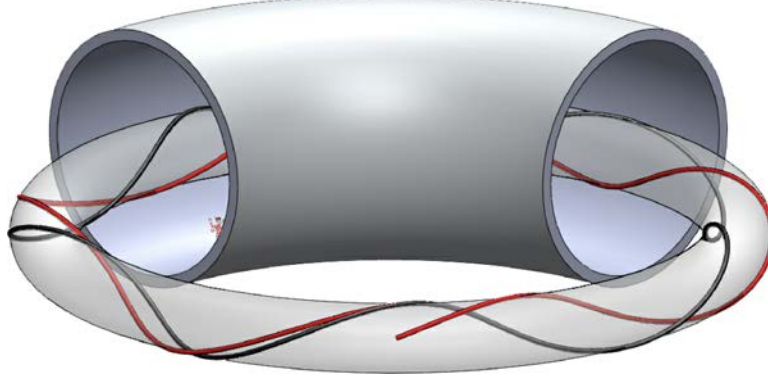


Fig. 4.6: A simulated magnetic field line (black) and a fast-ion guiding center trajectory (red). Drift motion causes deviation from the field line while particle stays on flux surface

An understanding of this deviation can be obtained through the notion of a fast-ion q . Whereas q_{mag} gives the pitch of the magnetic field line using the ratio of the toroidal to poloidal magnetic fields, fast-ion q gives the pitch of the fast-ion guiding center velocity and is defined analogously as

$$q_f = \frac{\omega_\phi}{\omega_\theta} = \frac{rv_\phi}{Rv_\theta} \quad (4.5)$$

where v_ϕ and v_θ are the toroidal and poloidal components of the guiding center velocity. The relationship between q_{fi} and q_{mag} is roughly [2]

$$q_f \cong q_{mag} + \frac{s_{\parallel}}{b_\theta^2} \rho \frac{2(1 - \mu\Omega)b_\theta^2 - r\mu\Omega'}{2R\sqrt{1 - \mu\Omega}} \quad (4.6)$$

where $s_{\parallel} = \frac{\mathbf{v} \cdot \mathbf{B}}{|\mathbf{v} \cdot \mathbf{B}|} = \pm 1$ is the sign of the direction of the parallel velocity (positive for co-injection), $b_\theta = B_\theta/|B|$ is the normalized poloidal component of the magnetic field, $\rho = v/\Omega$, $\mu = \frac{E_\perp}{E_0\Omega}$, $\Omega = \frac{eB}{m}$ is the cyclotron frequency, and Ω' is the radial derivative of the cyclotron frequency. $q_f \approx q_{mag}$ is recovered in the low energy limit. An example of a typical q -profile is shown in Figure 4.7 with the shifted q_f profiles also plotted for co- and counter-injection cases. Figure 4.8 highlights the effects of different plasma conditions on the shift from magnetic- q . The lower ratio of fast-ion to magnetic energy at higher current leads to a

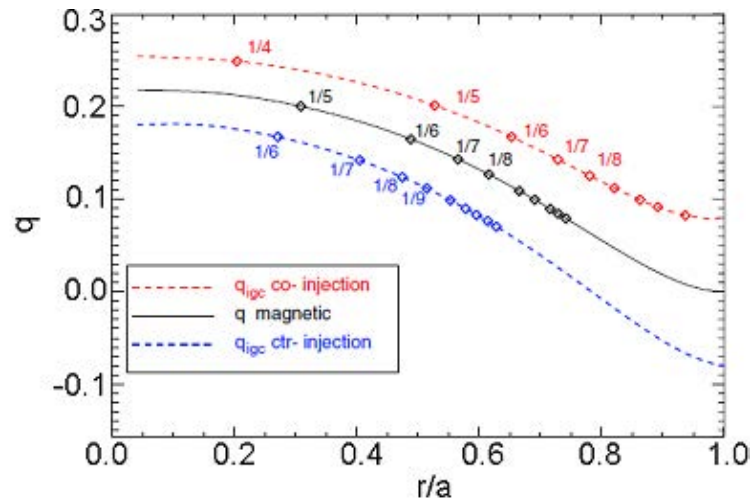


Fig. 4.7: Typical q -profile showing the safety factor in black. The fast-ion q is also plotted for co-injection (red) and counter-injection (blue). Also noted are the locations of rational surfaces

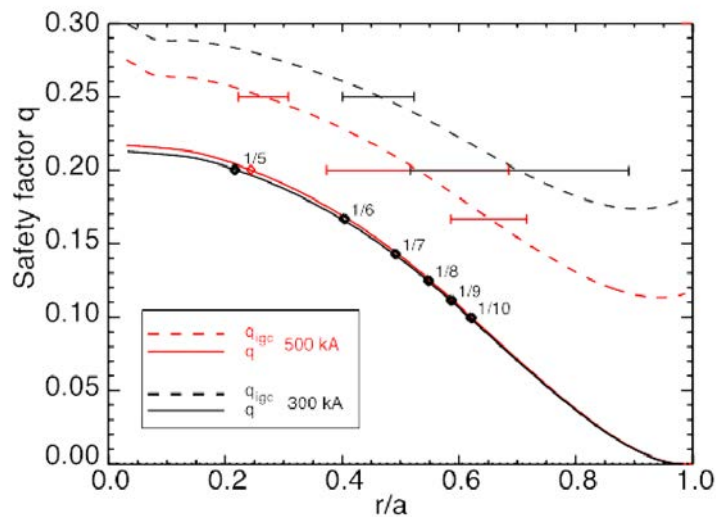


Fig. 4.8: q_f profiles for 25 keV DNBI into 300 and 500 kA plasmas. Smaller shift from q_{mag} due to stronger $|B|$ at higher plasma current. Also shown the approximate fast-ion island widths overlap at mid-radius.

reduction in the displacement of q_f from q_{mag} .

With this picture, the different confinement characteristics of fast-ions becomes clearer. In the co-injection case, the fast-ion q profile is shifted upwards away from q_{mag} . Consider a fast ion in the core of the MST plasma, where the closest resonant tearing mode is (1, 5). The radial magnetic perturbations are large, but the fast-ion orbit has a significantly different rotational transform so that the fast-ion does not resonate with the mode. Instead, the fast-ions that do exhibit an $n = 5$ rotational transform are located further out in radius (around $r/a \cong 0.5$ in Figure 4.7) where the $n = 5$ radial magnetic perturbations are weaker. Additionally, the core-most fast-ion rational surface in this example is the (1, 4) mode, but since the magnetic q profile peaks around 0.22 on axis, the (1, 4) magnetic island is absent from the plasma altogether. This leads to very low levels of magnetic fluctuation along a particle orbit and near classical confinement of co-injected fast ions in the core.

Understanding the dynamics of counter-injected beam ions warrants two observations. First, at the point of ionization beam ions are bent *outward* by the magnetic field where they are bent *inward* toward the core in the co-injection case. This leads to a higher initial loss fraction due to both prompt loss (ions striking the wall within a gyro-orbit) and a higher probability of charge-exchange loss due to the neutral density being higher near the edge. Secondly, the fact that the fast-ion rotational transform is shifted away from q_{mag} still has the effect of shifting fast-ions away from locations where they resonate with the local magnetic perturbation. Observing again Figure 4.7, the (1, 6) rational surface is located at $r/a \cong 0.48$ while the fast-ions with (1, 6) type orbits are located around $r/a \cong 0.26$. Unlike the co-injected case however, there is no fast-ion orbit that does not have an associated magnetic resonance within the plasma as was the case for the (1, 4) co-injected fast ion. This explains the measurement that counter-injected beam ions have a ~ 4 ms confinement time which is above thermal, but lower than the co-injected case.

The details of the fast-ion orbital motion are important when considering the drive of Alfvénic modes. Full orbit tracing for a given particle energy, pitch, and location utilizes the Adams-Bashforth-Moulton (ABM) method [58] (as it was found that the classical Runge-Kutta method (RK4) failed to conserve energy to sustain gyromotion). Example orbits highlight the differences between co- and counter-injection. Initial particle parameters are

chosen to represent a 25 keV beam neutral ionizing shortly after entering the plasma. The beam injection geometry and point of ionization are shown in Figure 4.9, and give an initial position of $R_0 = 1.64$ m, $Z_0 = 0.11$ m. Counter-injection mode is achieved in MST by reversing the direction of the plasma current. Given an initial velocity determined by the beam injection geometry, this gives an initial pitch (p) of $p_{co} = -0.64$ and $p_{ctr} = -0.9$. A third orbit was computed using the same initial position but using a radial velocity to mimic radial neutral beam injection. The orbits are shown in Figure 4.10 and clearly depict the influence of the initial inward or outward bending of an ion orbit based on its injection geometry.

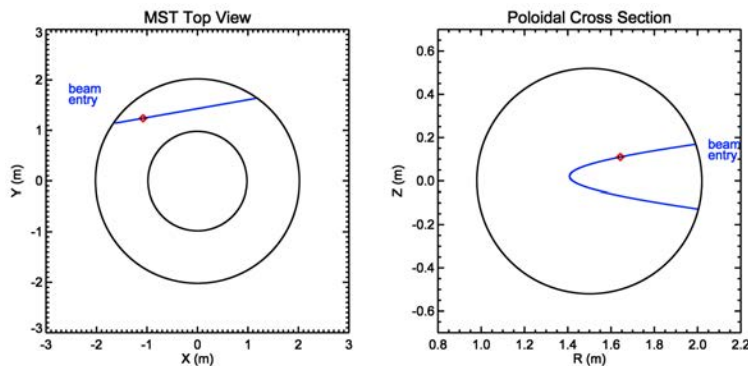


Fig. 4.9: NBI beam center as viewed from above MST (left) and as a poloidal cross section (right). Beam injection entry and particle ionization location are shown.

Fast-ion confinement spans a wide range in MST, from near thermal-like diffusive timescales in counter-injection or QSH to near classical in co-injection. The beam-blip method used for these studies was done intentionally in order to keep the fast-ion population a small perturbation on the bulk. Due to the good confinement during normal NBI operation, a large population of fast-ions develops in the core. Eventually a critical threshold is reached, and a sufficient population of fast-ions has developed that resonantly interacts with and destabilizes an Alfvén wave. The wave drives rapid transport of the ions, lowering the drive until the mode decays. The picture developed through the use of the q_f parameter has been shown to be quite useful in understanding the varying confinement times of fast-ions in MST and plays a key role in determining the particles that resonate with the Alfvén wave.

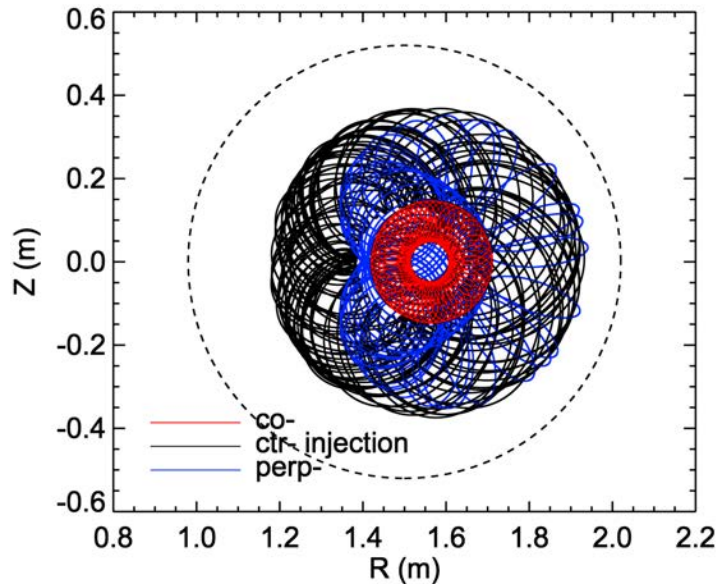


Fig. 4.10: Fast-ion orbits following co-, counter-, and perpendicular-injection from the same initial position. Velocities for co- and counter-injection are determined by NBI beam geometries.

4.4 EPM Growth Conditions

In order for an Alfvén continuum mode to grow, there must be a source of free energy, a resonance condition must be satisfied to transfer particle energy to the wave, and the drive must exceed any damping effects. The strength of the drive is related to the gradient in the distribution function providing the free energy.

Energy is transferred to the wave when the total energy of the ion population decreases by a flattening of some existing gradient (see Figure 4.11). A common example is that of Landau damping. Particles with a speed slightly less than the resonant velocity gain energy while those with slightly larger speed lose energy. Most distributions are monotonically decreasing with speed, meaning more particles gain energy than lose, resulting in wave damping. The introduction of a high energy population creates a “bump-on-tail” velocity distribution. The low-velocity side of the bump will have the reverse effect and transfer energy to the wave in a process called Inverse Landau damping. While this creates the conditions for drive, the distribution tends to quickly evolve to become monotonically decreasing with energy ($\partial f/\partial W < 0$), causing wave damping.

A spatially peaked profile contains free energy to drive Alfvénic perturbations. Consider

the canonical toroidal angular momentum

$$P_\phi = mRv_\phi - q_i\psi \quad (4.7)$$

where $\psi = RA_\phi$. P_ϕ decreases with increasing ψ , so an EP profile that is peaked on axis has $\partial f/\partial\psi < 0$, but $\partial f/\partial P_\phi > 0$. Moreover, as the energy increases with toroidal kinetic energy $W_{i,\phi} = P_\phi^2/(2m_i)$, the peaked distribution will have $\gamma \propto \partial f/\partial P_\phi^2 \propto \partial f/\partial W > 0$. The particles lose energy to the wave, and the condition is satisfied for wave growth. Although

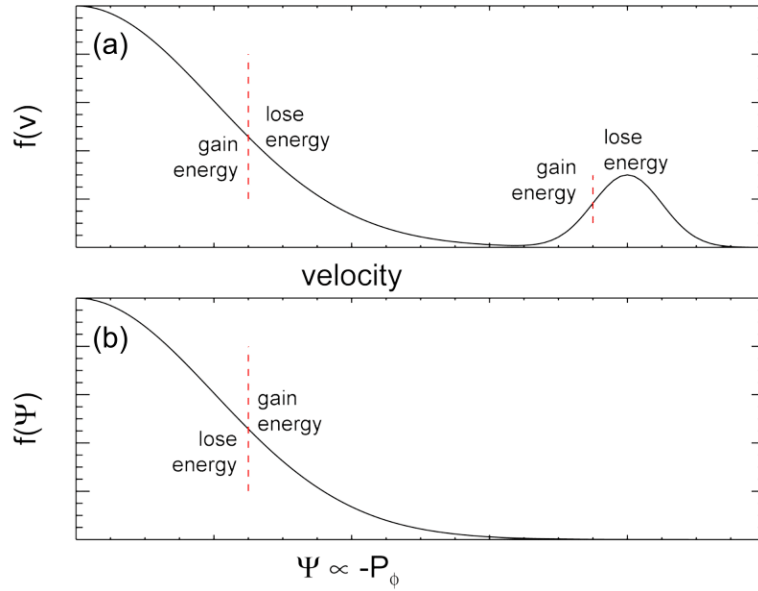


Fig. 4.11: (a) Landau (and Inverse) damping on a velocity distribution showing wave damping and (transient) wave drive. (b) Axially peaked EP distribution function results in wave drive due to gradient in the toroidal angular momentum.

this provides the picture for what drives an EPM, it remains unclear which fast-ion profile (whether density, pressure, or beta) should be identified when seeking a critical gradient for mode destabilization. This question will be revisited in Section 5.3 after the experimental data has been introduced.

The last necessary condition for mode growth is that the particles must couple to the mode allowing for energy transfer. The orbital motion of a particle must align in such a way so as to “kick” the mode. Mathematically we require $\oint \mathbf{v} \cdot \tilde{\mathbf{E}} \neq 0$ over several orbit cycles. For the tokamak, where drift components are dominantly poloidal and vertical, this results

in the resonance condition [59]

$$f = nf_\phi - (m + l)f_\theta \quad (4.8)$$

where f is the mode frequency, f_ϕ and f_θ the toroidal and poloidal fast-ion transit frequencies respectively, and l is an integer related to the poloidal decomposition of the fast-ion guiding center drift velocity. In the RFP, a strong B_θ leads to a substantial drift in the toroidal direction. A strict solution for Equation 4.8 with NBI sourced ion orbits cannot be found. A numerical approach to identifying wave-particle resonance is used.

For this study, a number of NBI ion orbits were modeled. An EPM with appropriate wave-number was simulated with perturbed \tilde{E}_θ , \tilde{E}_ϕ by a simple assumed mode structure. A radial magnetic perturbation \tilde{b}_r is modeled with a Gaussian amplitude profile centered at a chosen minor radius with a small $\sigma = 1$ cm half width

$$\tilde{b}_{EPM} = A(r) \sin(n\phi + \Delta\phi) \sin(m\theta + \Delta\theta) \quad (4.9)$$

where $A(r) = e^{-r^2/2\sigma^2}$ is the amplitude and n, m are respectively the toroidal and poloidal mode numbers of the EPM. As this study was only interested in finding resonances between particles and the waves and not optimized power transfer, initial phase offsets were ignored ($\Delta\phi = \Delta\theta = 0$). The fluctuating perturbed \tilde{E}_ϕ and \tilde{E}_θ components are then computed as follows

$$\nabla \times \tilde{B} = \mu_0 \epsilon_0 \frac{\partial \tilde{E}}{\partial t} \quad (4.10)$$

$$\Rightarrow \tilde{E}_\phi \propto -\frac{\partial \tilde{B}_r}{\partial \theta} = A(r) \sin(n\phi) \cos(m\theta) \quad (4.11)$$

$$\Rightarrow \tilde{E}_\theta \propto \frac{\partial \tilde{B}_r}{\partial \phi} = A(r) \cos(n\phi) \sin(m\theta) \quad (4.12)$$

The actual mode structure of an EPM is not well known in the RFP, but this simple model was sufficient to show resonance with NBI ions at the observed EPM frequency. Figure 4.12 is a summary of the wave-particle resonance investigation. A series of orbits sourced along the NBI centerline are selected, as depicted in 4.12a. For each orbit, a set of EPMS are studied for possible power transfer by scanning the radial location and frequency of the

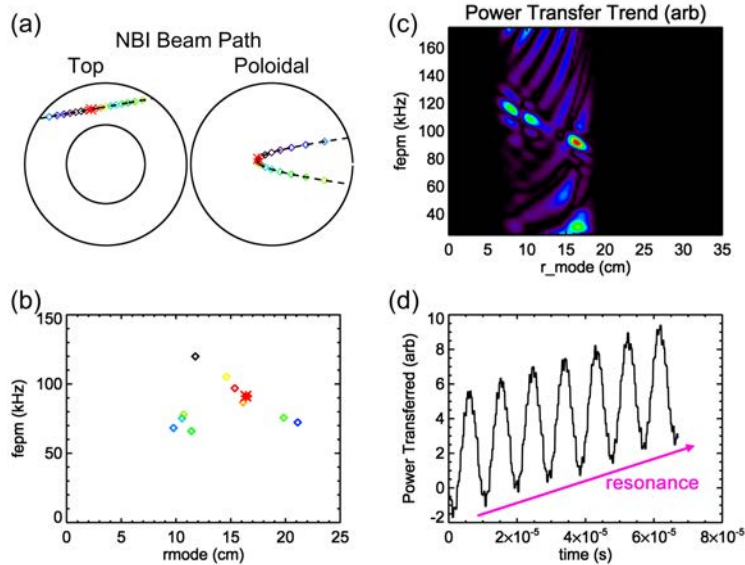


Fig. 4.12: Orbits modeled from various ionization sites along the NBI geometry (a) show resonance with a 60-80 kHz EPM around mid-radius (b). Scanning the EPM frequency and radial location results in “hot spots” of resonance (c) where net energy transferred to the wave grows in time (d).

mode, an example of which is shown in 4.12c for the orbit marked by the red asterisk. A sharp resonance in (r,f) space appears where the total power transferred increases with time (4.12d). For a number of the orbits modeled, a sharp resonance roughly in agreement with experimental observations (in radius and frequency) is observed and plotted in 4.12b.

4.5 Evidence for EPM-limited fast-ion beta

Alfvénic activity is accompanied by a redistribution of the driving ions and often radial transport. TRANSP modeling [12] herein neglects the nonlinear feedback on the distribution and expectedly over-predicts fast ion content in the presence of EPMs. While AE activity can be avoided in certain cases, the EPM will then destabilize at higher fast-ion pressure (recall the experiments at DIII-D to suppress the TAE in Section 2.5). The EPM stability threshold therefore represents the limiting factor in fast-ion confinement. By moving the reversal surface to the wall and controlling tearing mode activity in this work we have sought a clean set of experimental conditions in which to investigate and measure the critical fast-ion pressure.

NBI-heated discharges with EPM activity exhibit an apparent saturation in core fast-ion content. The mass difference between hydrogen and deuterium lead to substantially varied orbits and correspondingly altered interaction with the Alfvén activity. H-induced modes (as previously observed in mixed-fuel beam power scan studies [38]) do not resonantly drive transport of deuterium. Shown in Figure 4.13, a deuterium neutral beam scan was performed into 300 kA $F = 0$ plasmas. Following beam turn-on, the neutron rate increases with total fast-ion content. After a few milliseconds, a sufficient population has grown in the core, and EPM activity is observed at which point the neutron flux rolls over to a quasi-steady state implying a saturation in fast-ion content. For comparison, the predicted TRANSP neutron flux is included for a 40 A beam which steadily increases for the duration of NBI. The observed steady flux level with ongoing particle sourcing is consistent with a critical gradient being reached which drives fast-ion transport.

Two mechanisms are thought to produce the behavior observed. Fast ions are sourced primarily into MST's core via NBI. After a sufficient population has developed, a gradient drives an Alfvén continuum mode unstable, causing fast-ion transport. While evidence exists to suggest the fast ions are not lost directly, the fast ions may be moved out in radius where the $n = 5$ magnetic island causes larger perturbations to the particle orbit and fast-ion island overlap may cause stochasticity and loss of the particle.

4.6 Summary

Fast ions in MST can be well confined despite the presence of magnetic stochasticity. Co- and counter-injected ions exhibit rotational transforms significantly radially shifted from the associated magnetic perturbation. The core presents an area of very low transport especially for co-injected ions due to the absence of the magnetic island associated with the fast-ion mode numbers. Good confinement leads to the growth of a large population of fast-ions in the core that eventually approach the marginal stability threshold and excite EPM activity. A gradient in spatial fast-ion profile provides a source of free energy to drive the mode, and orbit resonance with the mode is satisfied for a sufficient fraction of NBI sourced ions. In both mixed- and deuterium-fuel NBI beam power scans, saturating behavior is seen on diagnostic

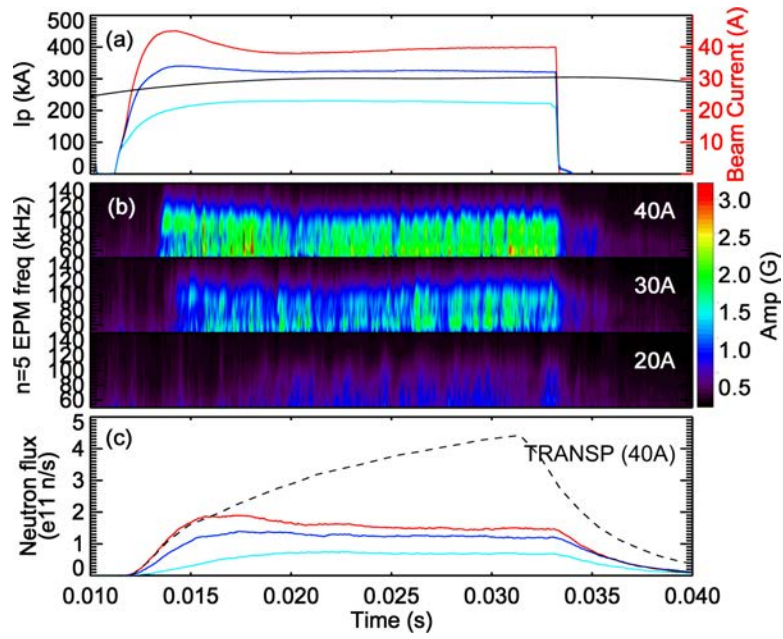


Fig. 4.13: Full deuterium beam shows EPM signal saturation. (a) 40, 30, and 20 A NBI into 300 kA plasmas results in (b) $n = 5$ EPM activity, with mode onset delayed at lower beam power. After onset of EPM activity, however, (c) neutron flux saturates, breaking with TRANSP predictions (dashed line).

signals indicating a limit in fast-ion content at marginal stability has been reached.

5. FAST ION BETA MEASUREMENTS IN MST

Complex nonlinear interaction between the EPM and the driving fast-ion population generates a fast-ion profile near marginal stability. The measurement of the fast-ion density (and pressure) profiles reveals the critical β_f gradient. We define $\beta_f = 2\mu_0 P_f / B^2$ is the fast-ion pressure P_f normalized to the magnetic field pressure. We note that although the fast-ion and magnetic pressures are both functions of radius, in order to be consistent with the existing literature we adopt the convention and report volume-averaged fast-ion beta as $\langle \beta_f \rangle = 2\mu_0 \langle P_f \rangle / B^2(a)$, where the volume average fast-ion pressure is normalized to the edge magnetic field value. The collection of fusion neutron diagnostics, and in particular the collimated neutron detector, along with information on the energy distribution to calculate the fusion reactivity, are used to measure the fast-ion density and pressure profiles. This is the first such measurement in an RFP device, and due to the strong magnetic shear shows a critical β_f larger than observed in tokamaks. Prior investigation of EPM activity in MST revealed simultaneous EPM and AE activity through multiple n -numbered modes. The plasma conditions herein exhibited almost exclusively EPM activity, making them conducive for a clean measurement of the critical gradient.

Section 5.1 details the experimental viewing geometries, plasma conditions, and the comprehensive analysis of the raw data for each viewing chord. The method of inversion from chord-integrated neutron flux to spatial fast-ion density profile is described in Section 5.2. These results, their implications, and avenues for future work are discussed in Section 5.3.

5.1 *Experimental Data*

2,130 discharges taken over 17 experimental run days compose the data presented here. Two datasets were created with plasma parameters shown in Table 5.1. The viewing chord

geometries for each dataset is shown in Figure 5.1 and summarized in Table 5.2. A large portion of the discharges were taken at the 300 kA plasma settings to improve the counting statistics allowing modest time resolution of the fast-ion density profile during the discharge. A sufficient number of discharges were collected at the 500 kA settings to provide a comparison in fast-ion profile between the two operating regimes (varied magnetic field strength). In addition to each chord data, a large background dataset was also taken at each set of plasma conditions. The differencing technique discussed in Section 3.4.3 was used to obtain a net count rate as a function of time for each viewing chord.

	Ip (kA)	F	$n_e(e13\text{ cm}^{-3})$	PMT bias (V)	# of discharges
Dataset 1	300	0	0.9-1.0	600	1602
Dataset 2	500	0	0.9-1.0	800	528

Tab. 5.1: Dataset parameters

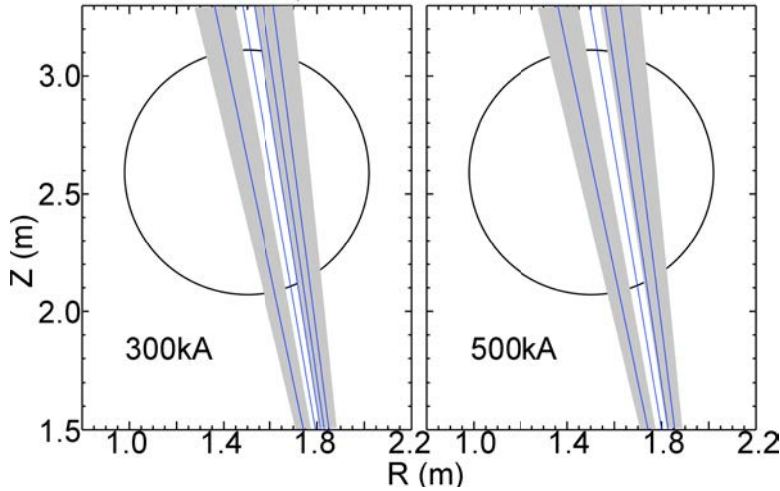


Fig. 5.1: Viewing chord geometries for 300 kA (left) and 500 kA (right) dataset. Blue lines depict CiNDe line-of-sight and gray sectors represent the extent of the viewing volume.

A measure of the fast-ion redistribution due to a burst of EPM activity necessitates mapping the fusion neutron count rate as a function of time in a small window around the averaged EPM (analogous to “sawtooth-ensembling” techniques commonly employed in studying RFP physics [60]). As bursts are a very nuanced manifestation of an instability arising from the interaction between a changing fast-ion distribution and a resonant magnetic mode, their appearance in a spectrogram can vary considerably. This makes reliable

300 kA		500 kA	
chord	minimum impact parameter (cm)	chord	minimum impact parameter (cm)
0	0	0	0
1	3.5	1	5
2	7.0	2	10
3	10.5	3	15
4	14		

Tab. 5.2: Chord geometries

computerized identification very difficult and the more labor-intensive process of manual identification necessary.

A temporal analysis of the neutron count rate and magnetic activity (tearing and EPM) is performed for each sampled line-of-sight of the collimated detector. Shown in Figure 5.2 is the data analysis for the core-viewing chord of the 300 kA dataset. Figure 5.2a shows a histogram of CiNDe pulse count-rate and global neutron signal ensembled over the dataset discharges, showing good agreement until the end of CiNDe’s data time-series at 30 ms. The ensembled $n = 5$ tearing mode amplitude (5.2b) highlights an interesting interplay between fast ions and the core-most resonant tearing mode. A large $n = 5$ tearing amplitude reduces fast ion confinement, while a large concentration of fast ions tends to suppress the core tearing activity. Subtle changes in the averaged fusion neutron flux are mirrored in the tearing amplitude. The plasma is dynamically evolving during the early NBI period, reaching a marginally stable state later in time.

A histogram of burst times (5.2c) reveals another interesting phenomenon. An initial period of rather chaotic looking EPM activity is followed by a quiescent period, eventually giving way to a nice periodic set of bursts later in the NBI discharge. This is most likely due to dynamically evolving plasma properties giving way to a quasi-steady. The quasi-steady state late in the discharge allows for regular uninterrupted burst cycles to occur.

An ensemble around the identified burst times is shown for CiNDe pulses and for the global neutron detector in Figure 5.2d. Perhaps surprisingly¹, there is not a measurable

¹ Earlier measurements with fast hydrogen revealed a drop in the (pitch-sensitive) ANPA measurement during mode activity, implying a redistribution of fast ions that (up to now) has been attributed to a flattening of the fast-ion spatial profile

change from before to after the EPM. In fact, panel (d) of 5.2-5.10 (each individual viewing chord for the two datasets) shows no change in neutron rate before versus after a burst of EPM activity. More discussion appears below.

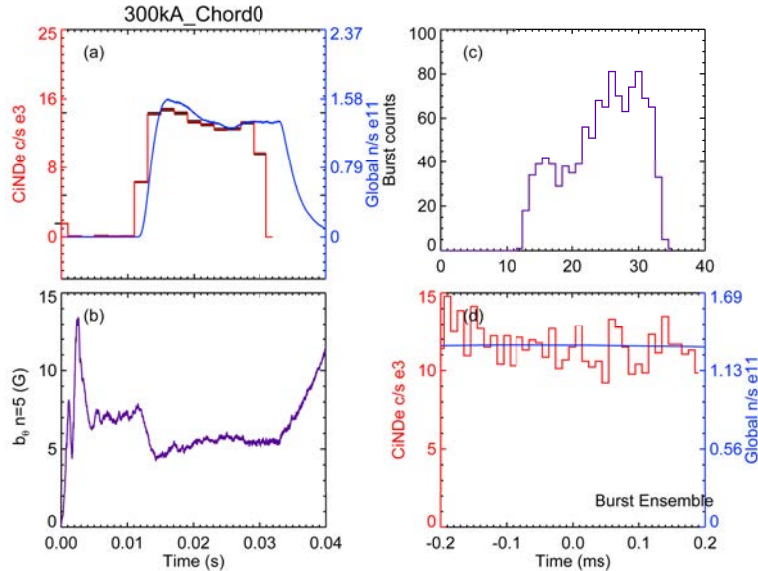


Fig. 5.2: Data analysis for core-viewing chord (0 cm impact parameter) for 300 kA dataset. Comparing CiNDe count rate to global neutron rate (a) and core-most tearing mode amplitude (b). Burst times plotted in (c) are ensembled for CiNDe and global neutron data in (d).

5.2 Data Inversion Method

The spatially resolved chord integrated fusion neutron count rates are inverted to measure the fast-ion density profile. Each chord has a pulse count rate on the order of $15,000 \text{ s}^{-1}$. The uncertainty is determined by averaging the time-dependent data on each viewing chord (represented by histograms in Figures 5.2-5.10a) and computing the standard error of the mean for each time bin. Larger time bins provide better statistics at the expense of temporal resolution. The plots presented here represent an attempt to strike a balance between these two effects. For each chord the background count rate is removed from the open-bore count rate. To accurately compare the open- and closed-bore datasets, they were normalized to the ensembled global neutron detector signal. The comparison then shows the clear signal increase when the bore plug is removed as depicted in Figure 5.11. The background is removed from the signal by taking the difference of these two normalized time series.

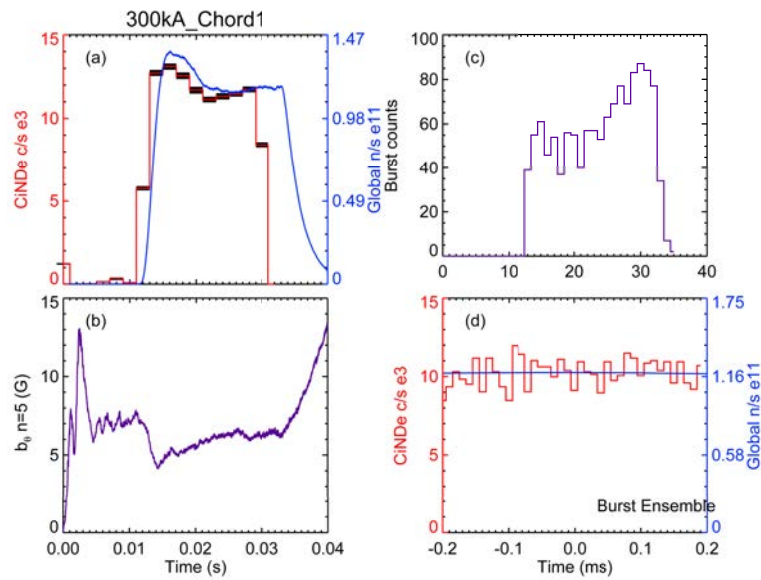


Fig. 5.3: Chord 1 (3.5 cm impact parameter) analysis for 300 kA dataset

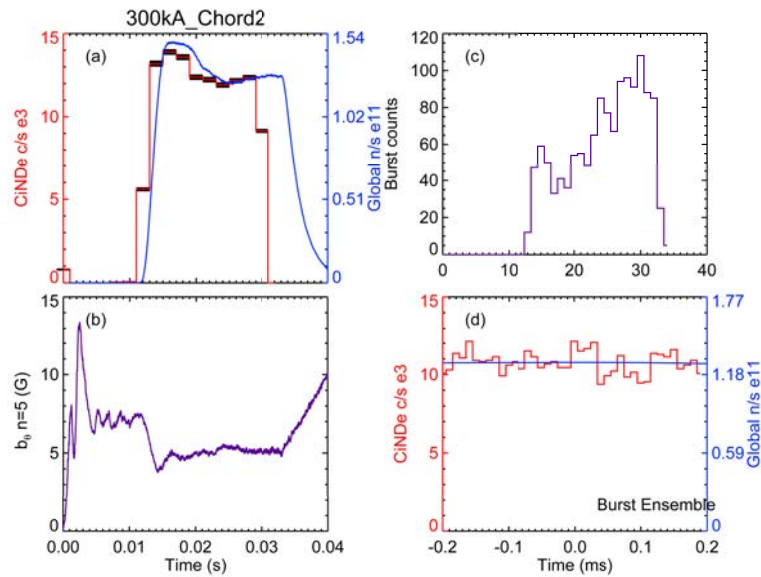


Fig. 5.4: Chord 2 (7 cm impact parameter) analysis for 300 kA dataset

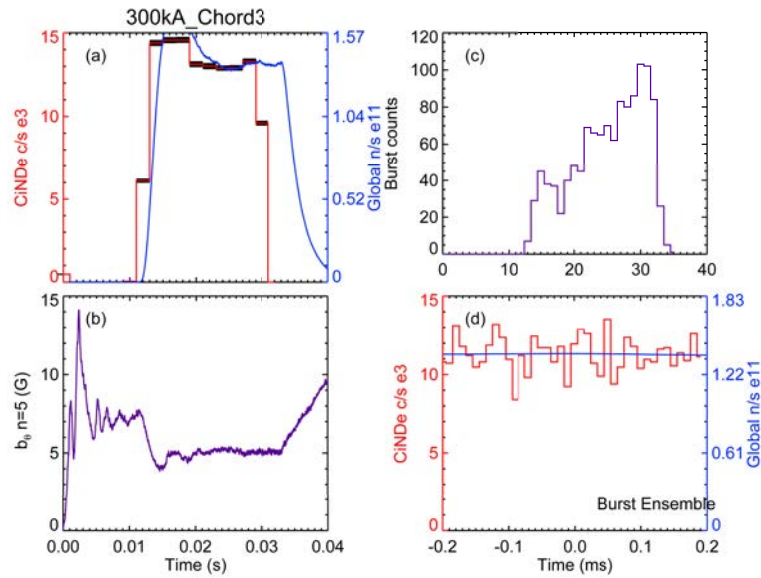


Fig. 5.5: Chord 3 (10.5 cm impact parameter) analysis for 300 kA dataset

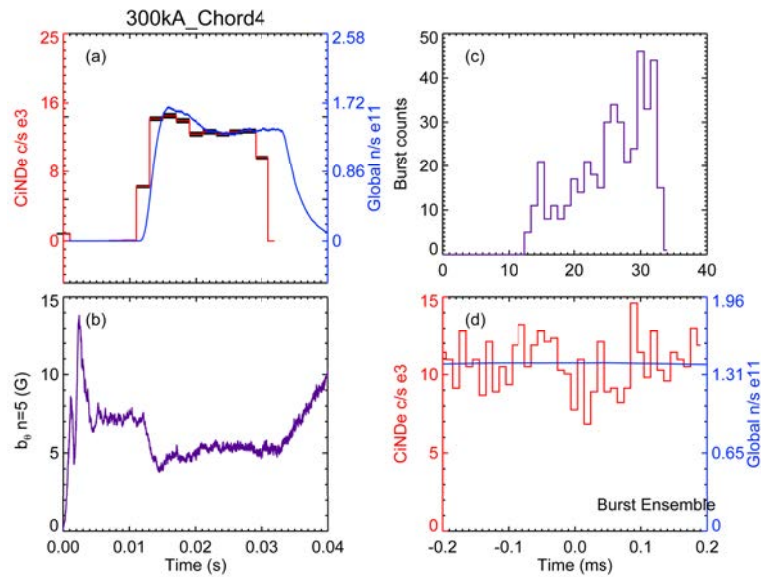


Fig. 5.6: Chord 4 (14 cm impact parameter) analysis for 300 kA dataset

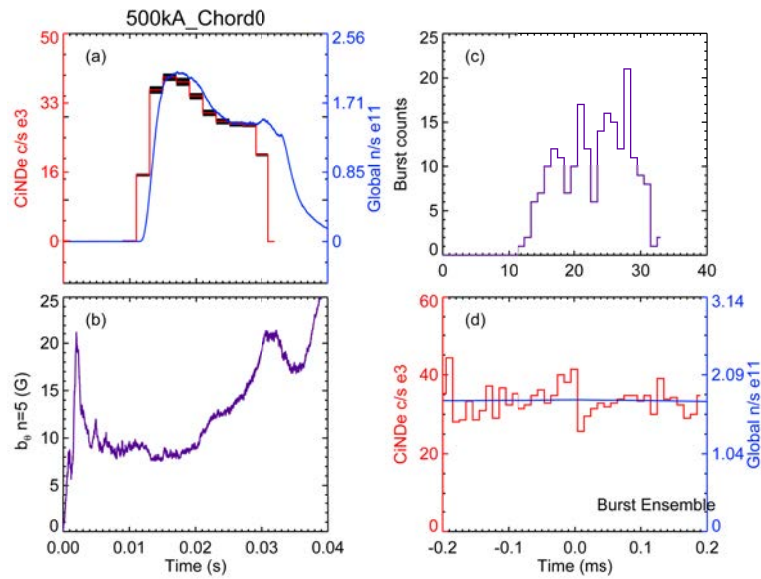


Fig. 5.7: Data analysis for core-viewing chord (0 cm impact parameter) for 500 kA dataset. Comparing CiNDe count rate to global neutron rate (a) and core-most tearing mode amplitude (b). Burst times plotted in (c) are ensembled for CiNDe and global neutron data in (d).

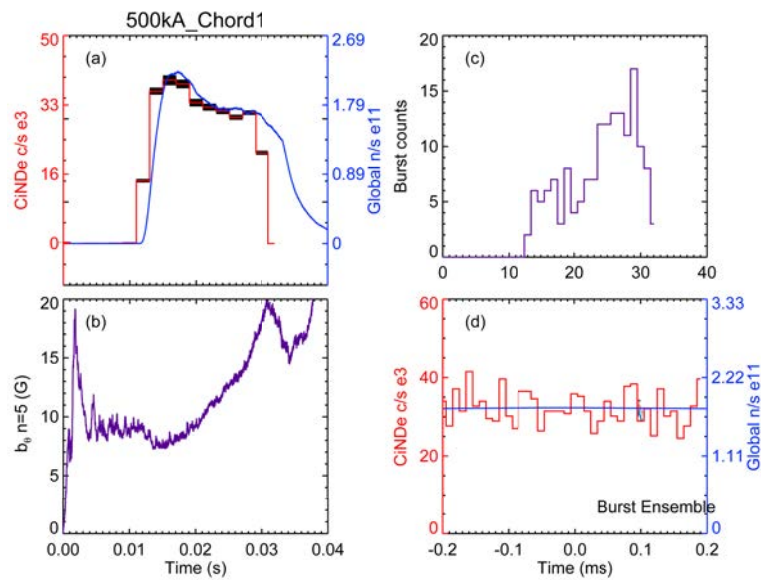


Fig. 5.8: Chord 1 (5 cm impact parameter) analysis for 500 kA dataset

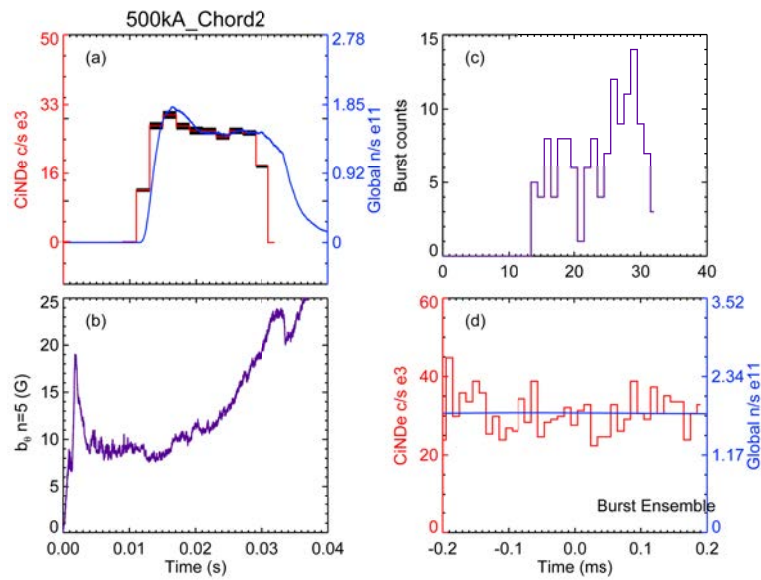


Fig. 5.9: Chord 2 (10 cm impact parameter) analysis for 500 kA dataset

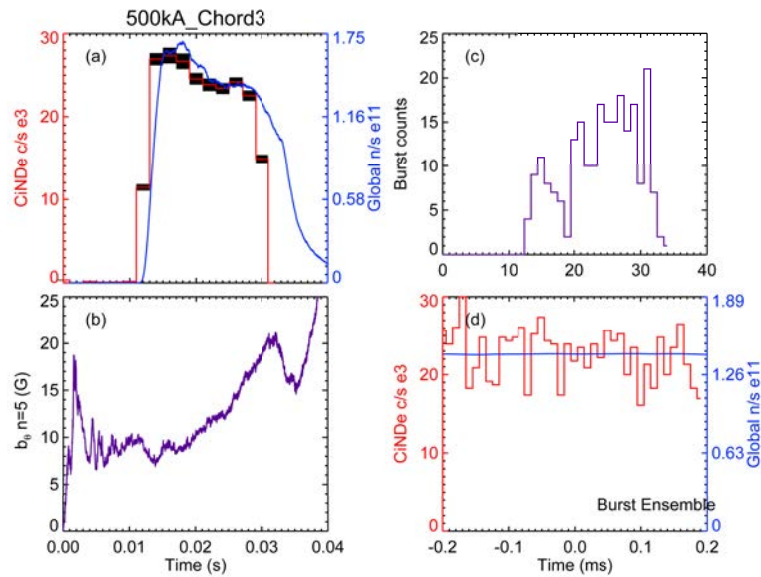


Fig. 5.10: Chord 3 (15 cm impact parameter) analysis for 500 kA dataset

The net count rate is then recovered by multiplying by the global neutron detector signal ensembled for all datasets. It should be noted that this final step is currently unnecessary as CiNDe remains uncalibrated and only the relative count rate between chords is important. The resulting net count rates for all chords are shown in Figure 5.12. Despite substantial

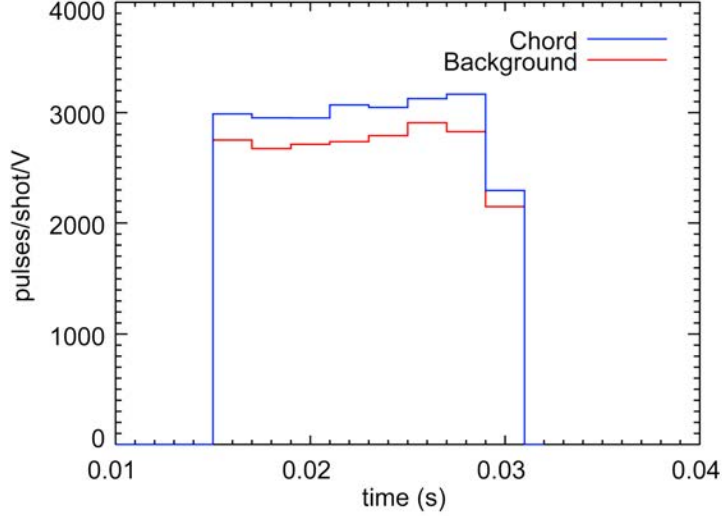


Fig. 5.11: CiNDe pulse count rates for core-viewing chord and background for the 300 kA dataset. Both signals are normalized to their respective global neutron detector signals to account for slightly varying plasma conditions.

uncertainty, it is clear that the neutron emission drops rapidly with increasing distance from the core, which is consistent with the expected core-localized fast-ion population.

Two large time bins are chosen for analysis. Given the dynamic evolution early as seen in the decrease in $n = 5$ tearing mode activity, we consider an early time (13-20 ms) and a late time (20-30 ms) in the discharges, the latter presumably representing a state of marginal stability. A second magnetic field strength is investigated by repeating the measurements in higher plasma current discharges (500 kA compared to 300 kA).

Measure of the fast pressure (beta) and density requires determining the fast-ion distribution function $f_f(r, E)$ with

$$n_f(r) = \int f_f(r, E) dE \quad (5.1)$$

$$P_f(r) = \int E f_f(r, E) dE \quad (5.2)$$

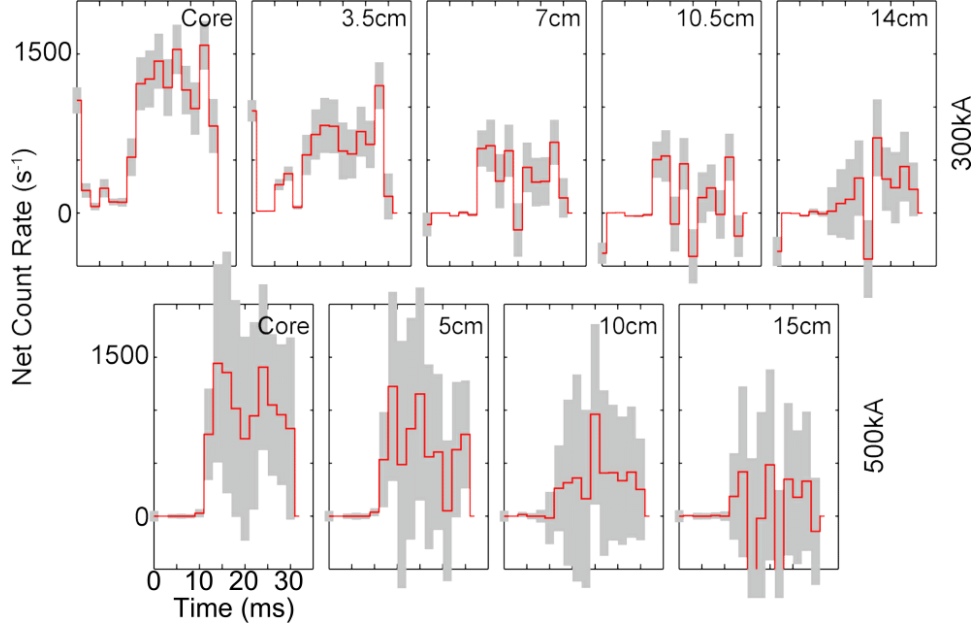


Fig. 5.12: Net count rates for the five (four) chords for the 300 kA (500 kA) dataset. A clear reduction in neutron emissivity is seen with increasing distance from the core, becoming effectively zero at ~ 15 cm.

We proceed with two assumptions: First, the distribution function is separable into spatial and energy dependence.

$$f_f(r, E) = f_f(r)f_{NPA}(E) \quad (5.3)$$

This is consistent with TRANSP modeling where the average fast-ion energy is nearly constant in radius (Figure 5.13). The energy dependence $f_{NPA}(E)$ is measured by neutral particle analysis on MST and by definition of relative calibration $\int f_{NPA}(E) dE = 1$. Figure 5.14 shows the energy resolution of the fast-ion distribution in the 300 and 500 kA plasma conditions. The measured relative distribution is comparable to the classical slowing distribution in TRANSP (Figure 5.15). Both the full- and half-energy component are visible, but what TRANSP models as a large population near the injection energy is measured experimentally to be much flatter down to lower energies.

The second assumption is that a two-parameter fit describes the spatial dependence sufficiently well. The distribution is then measured by inversion of chord-integrated fusion neutron emissivity and a comparison to the total neutron emissivity.

The detailed mapping between fast pressure and neutron emissivity begins by modeling

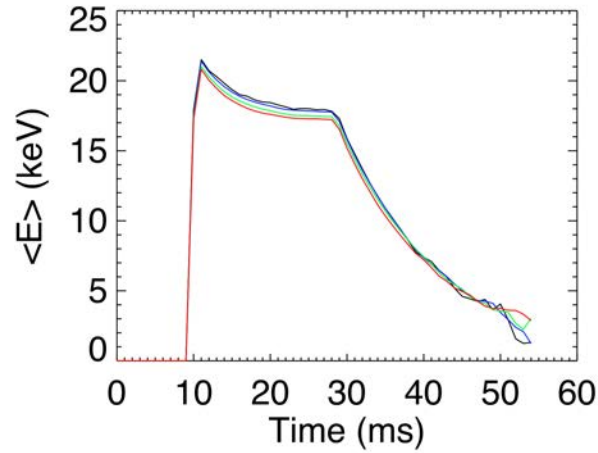


Fig. 5.13: TRANSP average fast-ion energy vs time at four radii from $r = 0-0.2$ m shows near constancy with radius.

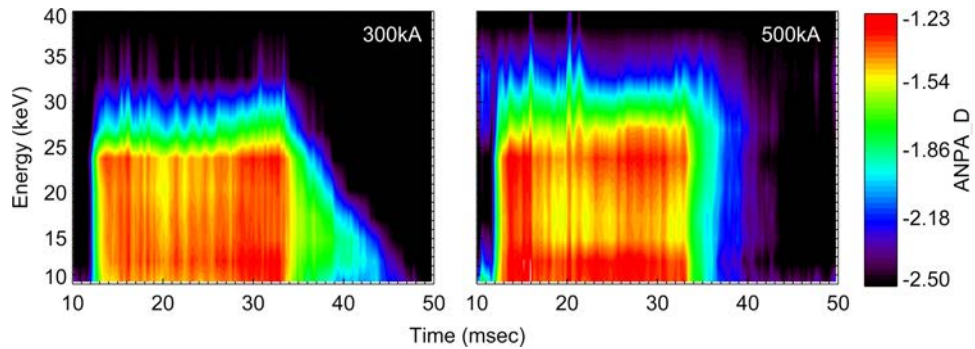


Fig. 5.14: ANPA spectrogram for 300 and 500 kA datasets. Injection near 25 keV connects through a broad profile to the lower energy channels.

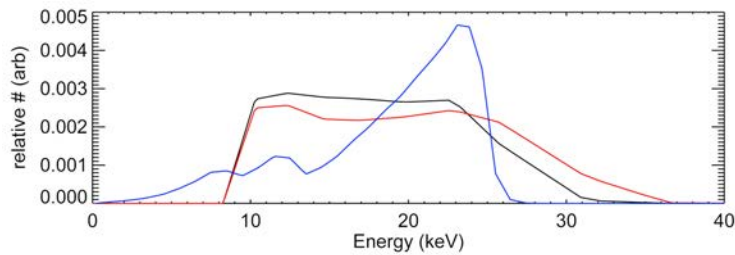


Fig. 5.15: ANPA fast-ion energy distributions for 300 (black) and 500 kA (red) plasmas, and comparison to TRANSP modeling at 300 kA (blue).

a Gaussian fast-ion beta profile (the assertion of a Gaussian shape will be relaxed later, with comments), defined by an amplitude and width (y_0, σ). The pressure and density profiles are found using equations 5.1, 5.2 above

$$P_{mag}(r) = \frac{B(r)^2}{2\mu_0} \quad (5.4)$$

$$P_f(r) = \beta_f(r)P_{mag}(r) \quad (5.5)$$

$$f_f(r, E) = \beta_f(r)P_{mag}(r) \frac{f_f(E)}{\int E f_f(E) dE} \quad (5.6)$$

The MST plasma is modeled as discrete volume elements and a uniform flux for each element is computed

$$\Gamma_i = \int f_f(r_i, E) n_i \sigma v_f(E) dE \Delta V_i \quad (5.7)$$

where the integration is over energy within each volume element. The ion density is estimated from the electron density measurements and the fusion reactivity σv is tabulated. The total predicted flux is given by summing over the MST volume, while the chord-integrated flux is given by

$$\Gamma_{chord} = \sum_i \frac{\Delta \Gamma_i}{4\pi r_i^2} \quad (5.8)$$

where the index i reflects only those volume elements within the CiNDe viewing volume and r_i is the distance from the volume element to the detector. The fit parameters are scaled so that the modeled emissivity matches the measured (calibrated) global neutron flux, resulting in a calibrated chord-integrated emissivity prediction. A 2D parameter scan is carried out in order to optimize the two-parameter β_f model. Shown in Figure 5.16 is the optimization done for the 300 kA dataset, “early” in time on the left and “late” on the right. There is a clear minimum in the y_0, σ parameter space and the agreement between modeled and measured data is good. Each viewing chord effectively adds an equation, and 4 or 5 chords are used to create an over-specified problem. The fast pressure (beta) and density profiles are computed with parameters and uncertainties determined from a least squares analysis.

A sensitivity analysis was performed in order to assess how the choice of profile shape influences the results. We compare three different shapes- Gaussian, linear, and flat- defined by an amplitude y_0 and width σ as shown in Figure 5.17. The optimizations of these two

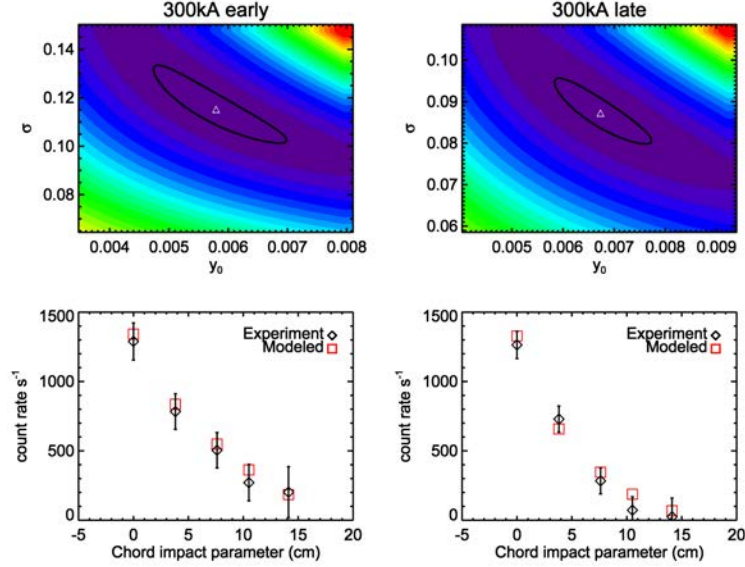


Fig. 5.16: Gaussian profile parameter optimization for the 300 kA dataset. A clear minimization exists in $y_0 - \sigma$ parameter space and results in good agreement between the predicted and experimentally measured count rates.

parameters for each profile shape for the late portion of the 300 kA dataset are shown in Figures 5.16(right) and 5.18.

The “flat” profile produces an infinite gradient at some radius and cannot be expected to find a critical destabilizing gradient. It is included for gaining a sense of the sensitivity to profile shape only. While it matches the data amusingly well, the χ^2 space has a less well-defined minimum. The linear and Gaussian profile models are both more physical in the search for a limiting β_f gradient. The linear fit uses the critical gradient on the entire profile, and the Gaussian offers a smooth derivative through the origin. In reality it is more likely that the profile is Gaussian, as we expect a smooth function in space.

The best fit for each model produces the β_f in 5.19. It is worthwhile to note that they give similar results (particularly in the volume-averaged β_f value²), and we proceed with the analysis assuming Gaussian profiles.

The optimization and comparison of modeled to measured data for 500 kA are shown in Figure 5.20, with the results used to compute the fast-ion density and pressure profiles below.

² The volume averaged beta value is computed as the volume averaged fast-ion pressure normalized to the edge magnetic pressure. This gives $\langle \beta_f \rangle = 2.20, 2.19,$ and 2.17 for the Gaussian, linear, and flat profiles respectively.

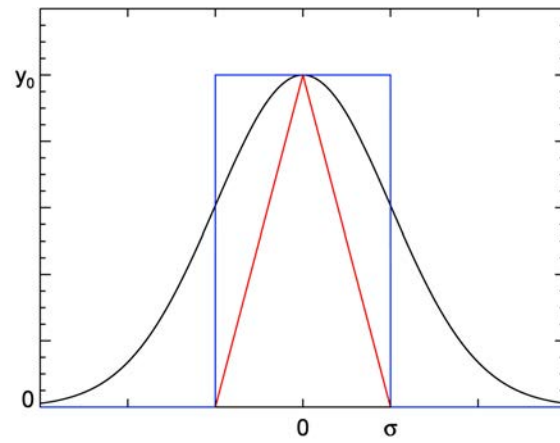


Fig. 5.17: Three profile shapes considered to determine sensitivity of results.

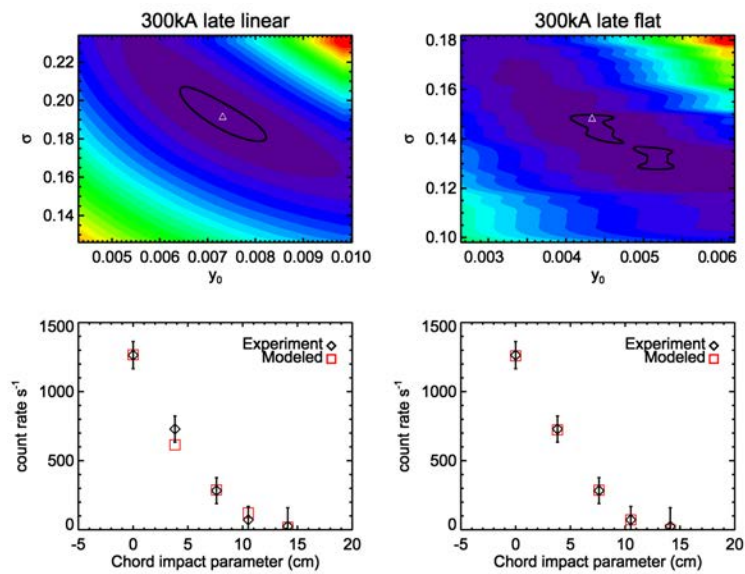


Fig. 5.18: Optimization for the 300 kA late dataset linear and flat profiles.

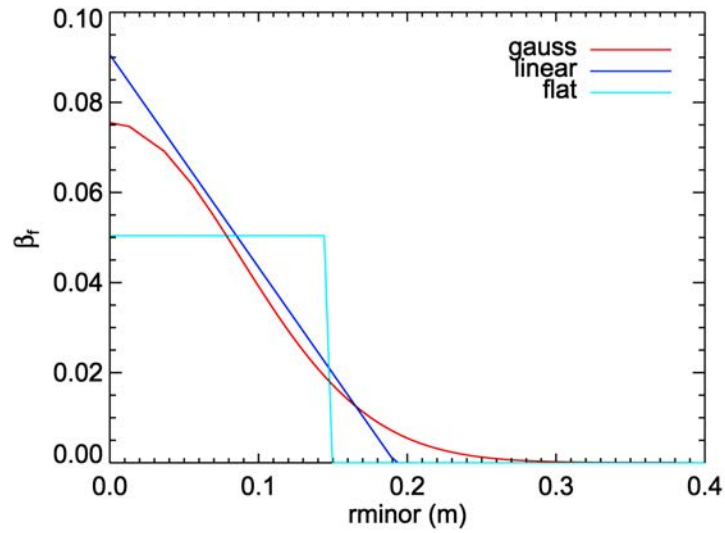


Fig. 5.19: Comparison of the resulting β_f for the 300 kA late dataset following parameter optimization for the three tested profiles shown in Figure 5.17.

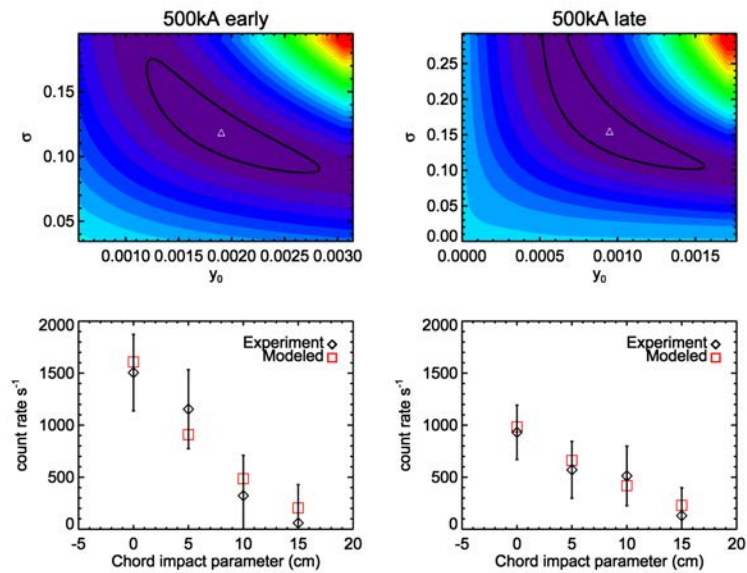


Fig. 5.20: Gaussian profile parameter optimization for the 500 kA dataset.

5.3 Fast-ion Profiles

The profiles reconstructed from the two datasets are presented in Figures 5.21-5.23. The amplitude of the core tearing mode plays an important role in determining EPM dynamics. At 300 kA, NBI considerably reduces the $n = 5$ tearing mode amplitude. At 500 kA this effect is gone. Instead an overall increase in time of the tearing mode amplitude is observed, due to numerous transitions into QSH within the ensembled set of discharges. The effect of this is twofold. First, fast-ion confinement in the QSH state drops dramatically from the otherwise near classical confinement of NBI ions, which will result in a lower overall fast-ion content. Secondly, the width of the fast-ion islands is set by the strength of the tearing mode amplitude of corresponding mode number. So as the $n = 5$ tearing mode amplitude grows, so does the $n = 5$ fast-ion island. Thus small radial displacements of a fast-ion have a larger likelihood of placing it on a stochastic orbit. Observing Figures 5.21-5.22, the tearing mode amplitude stays flat (and reduced) in the 300 kA case and the profile peaks later in time into a state of marginal EPM stability. In the 500 kA case however, the tearing mode amplitude grows during the discharge, resulting in a broader and lower profile later in time.

There is also a considerable difference in the EPM activity between the two datasets. The ensembled EPM activity shows mode splitting in the 300 kA case which has been observed before [61], something not present in the 500 kA case. The cause of the mode splitting is not fully understood, but a possible explanation may lie with the wave-particle resonance studies in Section 4.4. Previous studies of the $n = 5$ EPM coupling to an $n = 4$ and $n = -1$ mode have shown increased fast-ion transport when multiple modes are active [62]. Shown in Figure 5.24 is the ensembled $n = 5$ and $n = 4$ activity for both datasets. It is clear that in the present data, only a small fraction of the bursts are associated with triplet activity. The lack of triplet activity in these datasets presents a substantially different dynamic than previous studies; a careful investigation of fusion neutron flux by D-driven triplets is a future experiment.

The relevant quantities from Figure 5.23 are summarized in Table 5.3.

There is a striking difference in the β_f profile between 300 and 500 kA. It was perhaps expected that the beta profiles would show a similar shape, implying one value of a critical

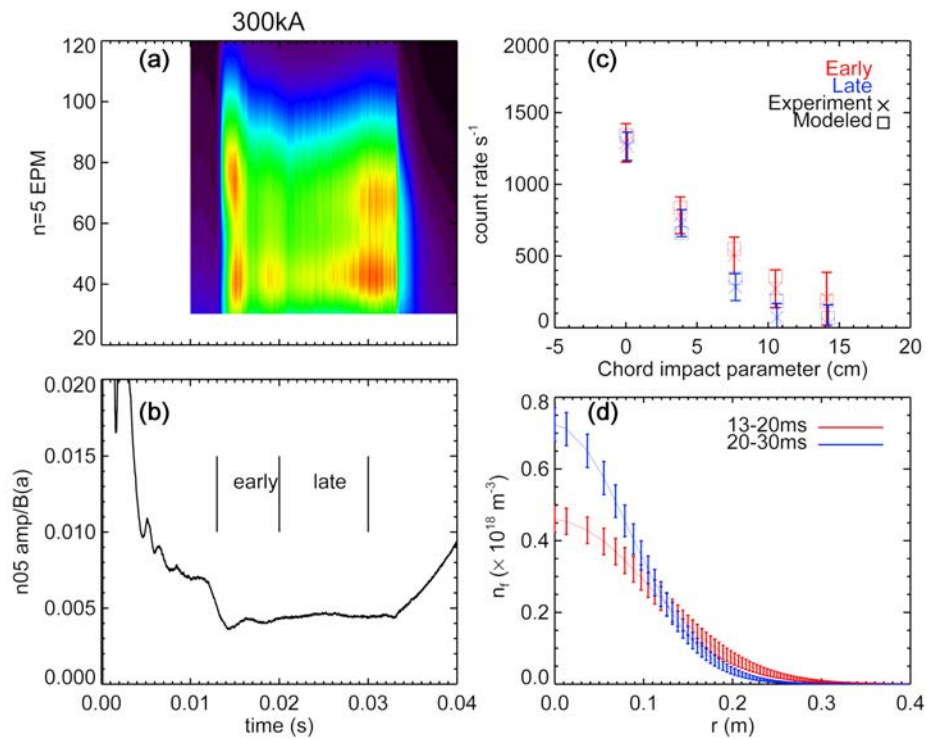


Fig. 5.21: 300kA Dataset averages of $n = 5$ EPM activity (a) and core-tearing activity (b). Optimization of profile parameters to match experimental values (c) results in n_f profiles shown in (d) early and late in the discharge.

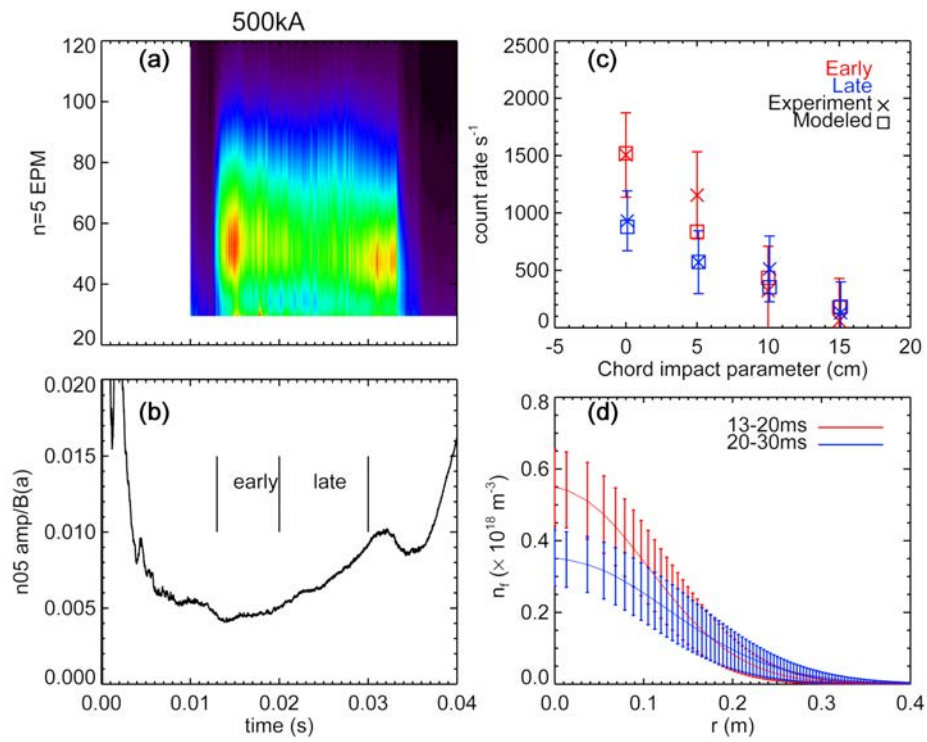


Fig. 5.22: 500kA Dataset averages of $n = 5$ EPM activity (a) and core-tearing activity (b). Optimization of profile parameters to match experimental values (c) results in n_f profiles shown in (d) early and late in the discharge.

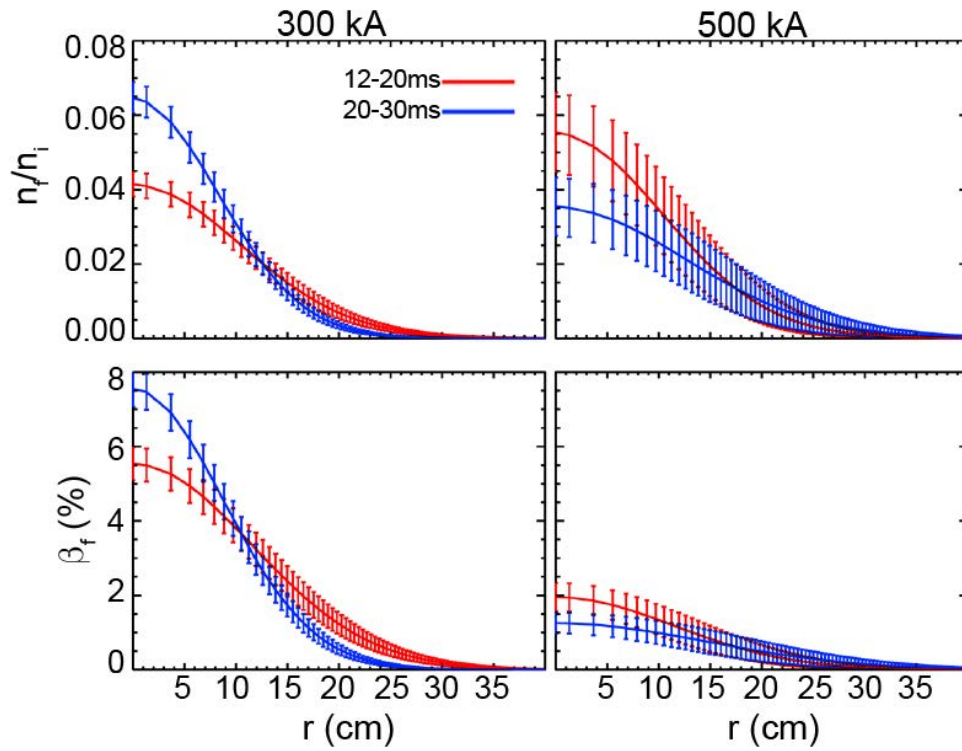


Fig. 5.23: Reconstructed fast-ion profiles, normalized to the bulk ion density n_f/n_i (top) and β_f (bottom) profiles for the two datasets early and late in the discharge.

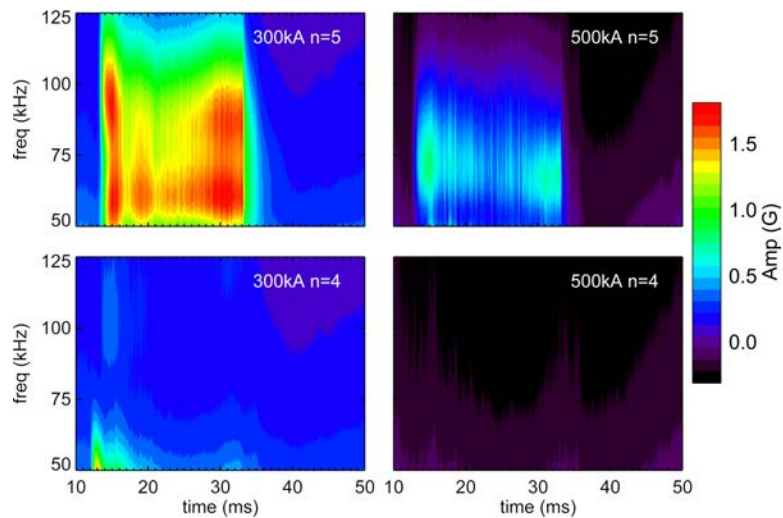


Fig. 5.24: A side-by-side comparison of the ensemble $n = 5$ and $n = 4$ activity for both datasets shows a predominance of $n = 5$ activity.

	$\beta(0)(\%)$	$\langle\beta_f\rangle(\%)$	$\nabla\beta_f(\%/cm)$	$\nabla n_f(e16/cm^4)$	$\nabla(n_f/n_i)(\%/cm)$
300 kA early	5.53 ± 0.44	2.52 ± 0.43	0.29 ± 0.007	2.65 ± 0.09	$.24 \pm 0.01$
300 kA late	7.55 ± 0.48	2.2 ± 0.30	0.52 ± 0.013	5.27 ± 0.14	0.47 ± 0.01
500 kA early	1.86 ± 0.36	1.08 ± 0.47	0.10 ± 0.005	3.20 ± 0.24	0.32 ± 0.02
500 kA late	1.16 ± 0.26	0.94 ± 0.48	0.05 ± 0.001	1.70 ± 0.12	0.20 ± 0.70

Tab. 5.3: Profile gradients

$\nabla\beta_f$ needed to drive an EPM. The picture remains more complicated, as there are too many differences between the two cases to draw a simple comparison. The background tearing activity, the effective drop of beam speed from super- to sub-Alfvénic with increased B , and the drop in deviation of q_f from q_{mag} (Figure 4.8) all contribute to a reduced fast-ion drive for Alfvénic modes.

The $n = 5$ tearing mode amplitude is larger in 500 kA plasmas. As a result, the magnetic island that develops at the rational surface may act to push the steepest part of the fast-ion gradient out in radius, creating a central region of relatively flat fast-ion density. This would manifest as the broader and lower density profiles. By moving the gradient further out in radius, other effects may become important (such as charge-exchange with the neutral population, or stochastic fast-ion orbits brought on by fast-ion island overlap) that reduce the fast-ion content, sapping the free-energy source needed to drive the EPMS. More simply, confinement of fast ions may be reduced with larger tearing mode amplitude. A larger tearing mode amplitude in the 500 kA case may reduce the fast-ion confinement time leading to weaker EPM drive.

Ensembling together the bursts identified from the two datasets (Figure 5.25) further supports this picture. The duration of the burst differs in the two cases. 300 kA plasmas exhibit stronger drive (due to a more strongly peaked fast-ion profile). With weaker drive through a broader fast-ion profile, reduced damping is required to explain the rapid growth. The observed frequency is similar in both cases. The Alfvén continua representative of the plasmas studied here (Figure 5.26) then imply the mode is most likely at smaller radius where the q-profile is flatter.

As a final thought on the interaction between the fast-ion population and EPM excitation, consider the energy of the beam ions. Relative to the magnetic energy density of the plasma,

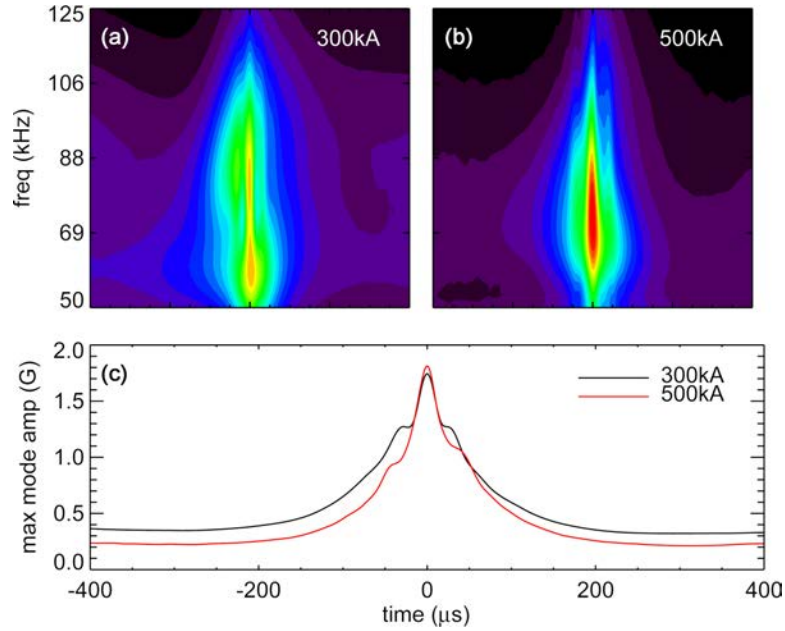


Fig. 5.25: Burst ensemble for (a) 300 kA and (b) 500 kA dataset. Mode amplitude versus time (c) shows more abrupt bursting behavior at higher current.

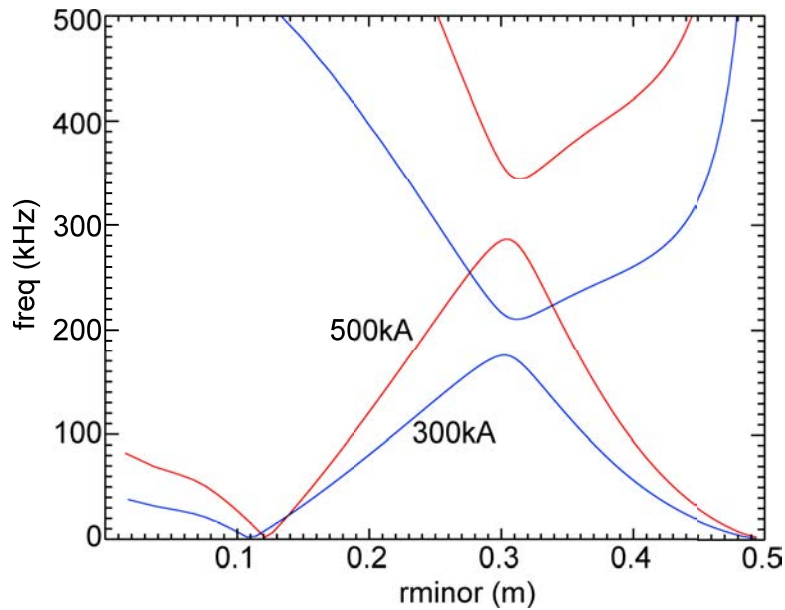


Fig. 5.26: Representative Alfvén continua of the two datasets.

the beam ion energy is much lower in the 500 kA case. In fact, what were super-Alfvénic ions in 300 kA are sub-Alfvénic, from which we would expect weaker drive of Alfvénic modes. Furthermore, having a reduced relative energy causes the displacement of q_f from magnetic q to be smaller, resulting in larger fast-ion islands and increased stochasticity of the orbits. Only in the 300 kA case was a marginally stable state achieved.

The two datasets amassed for this research were an effort to investigate differences in the fast-ion dynamics at varied magnetic field strengths, in part to help identify the source of drive for the fast ions (mentioned in Section 4.4). The fact that only one measure of the fast-ion beta in a marginally stable state was achieved restricts our ability to determine the profile responsible for EPM drive. Fast-ion beta profiles are reported here as it is what appears in the theoretical predictions [14, 19]. Furthermore, the discussion of a critical gradient in fast-ion beta is largely synonymous with a discussion of a critical gradient in fast ion pressure or density, for two reasons. First, given the peaked, core-localized profile measured here, the fast-ion pressure scale length is much shorter than the magnetic field scale length (at mid-radius $(\nabla P_f/P_f)^{-1} \approx 2$ cm, $(\nabla B/B)^{-1} \approx 25$ cm see Figure 5.27) so that

$$\left(\frac{\nabla\beta_f}{\beta_f}\right)^{-1} = \left(\frac{\nabla P_f}{P_f} - \frac{\nabla P_{mag}}{P_{mag}}\right)^{-1} \approx \left(\frac{\nabla P_f}{P_f}\right)^{-1} \quad (5.9)$$

$$\nabla\beta_f \propto \nabla P_f \quad (5.10)$$

Thus while the P_f term dominates over P_{mag} as in the conditions studied here, a critical gradient in the fast-ion pressure corresponds to a critical gradient in the fast-ion beta. Second, here we have used ANPA data for the energy distribution of the fast ions and assumed this to be constant in radius (which is supported by TRANSP predictions). Since $P_f(r) = \int n_f(r, E) dE = \langle E \rangle n_f(r)$ it then follows that

$$\nabla P_f \propto \nabla n_f \quad (5.11)$$

This correlation holds so long as variations in radius of the fast-ion energy remain small. Further experimentation at varied plasma conditions that exhibit marginal stability may elucidate the correlation between EPM activity and the gradients in β_f , P_f , and n_f , but

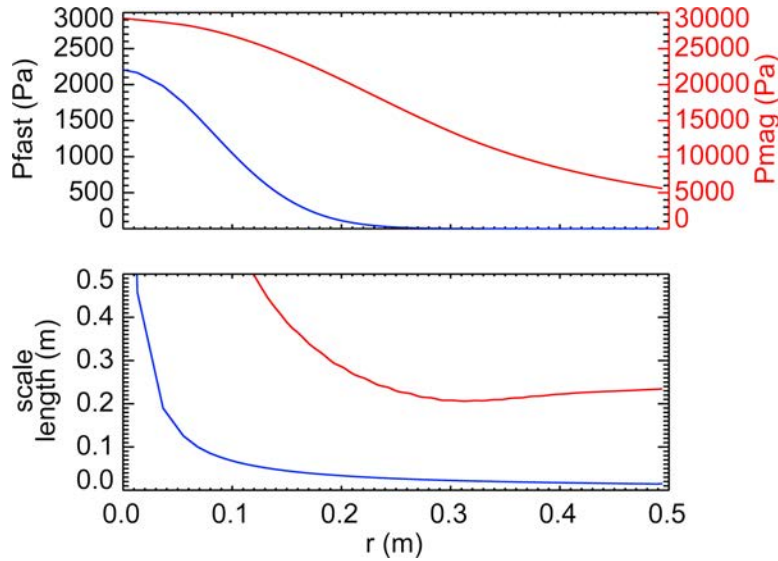


Fig. 5.27: Fast-ion (red) and magnetic (blue) pressure profiles and corresponding scale lengths.

here a critical β_f is reported with the preceding comments in mind.

A comparison with TRANSP shows a modest deficit, where TRANSP classical modeling predicts $\beta_f(0) \sim 10\%$ and the measured value is $\beta_f(0) \sim 7.5\%$. This reduction is consistent with fast-ion transport driven by EPM activity unaccounted for in the modeling. Such a small reduction from the classical confinement prediction implies relatively weak transport of the fast ions. This is consistent with the earlier analysis which showed no drop in neutron signal across a burst, and with previous research into the mode triplet which showed enhanced transport with AE activity [61].

We close the chapter by revisiting the deuterium beam power scan (Figure 5.29a,b,c). At lower beam current, the neutron flux saturates at a lower level. While this may seem in contradiction with the claim that all three states are at marginal stability to the EPM, it is consistent with the picture developed here. EPMS are driven by resonant beam-energy ions which then cause a preferential loss of those high energy ions. At lower beam current, the fast-ion pressure builds more slowly. As the fast ions have more time to slow classically before an EPM, there will be a larger population that will not be resonant with the EPM driven by higher energy ions. This results in a lower average fast-ion energy at lower beam current. A second effect is depicted in Figure 5.29d,e. The overlap of fast-ion islands effectively creates a location (near mid-radius) beyond which fast ions experience substantial radial

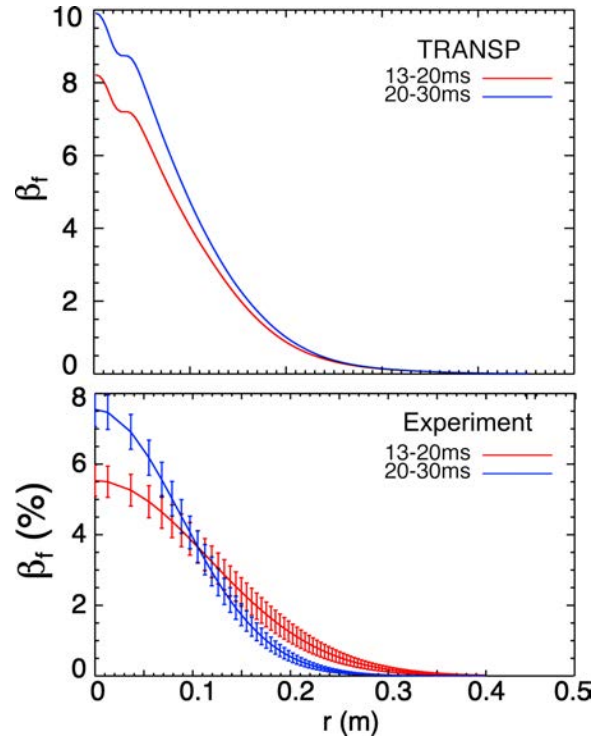


Fig. 5.28: Comparison of modeled (TRANSP) and experimental β_f profiles. A reduction in core β_f is consistent with EPM activity driving fast-ion transport.

guiding center velocity perturbations. Here they are diffusive and can be characterized by some finite confinement time [2]. In Figure 5.29e, the square symbol marks the diffusive boundary, where the value is set by $dN_f/dt = S - N_f/\tau$ and S, τ are the fast-ion source rate due to NBI and the diffusive timescale respectively. A higher source rate would then set a larger n_f “edge” value at this radius. The profile inward is then limited by bursting activity on a critical gradient producing lower values of $n_f(0)$ (and neutron flux) at lower beam current, consistent with the experiment. While the reduction in tearing mode amplitude is effectively the same in the 40 and 30 A beam current cases, at 20 A this effect is reduced. The larger tearing mode amplitude at lower current increases the fast-ion island widths, pushing the diffusive boundary layer inward, leading to a further reduction in the fast-ion density at low beam current.

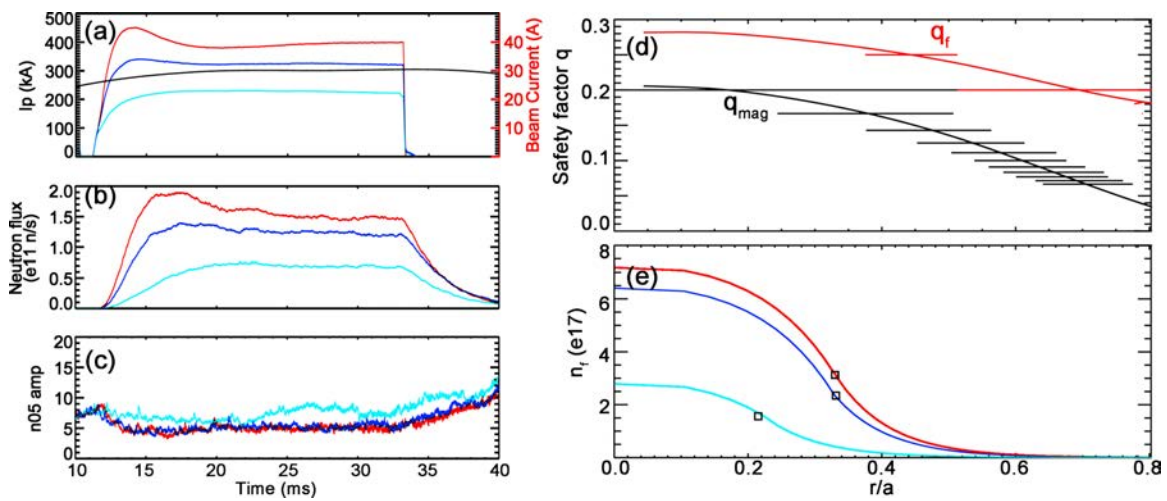


Fig. 5.29: The deuterium beam power scan revisited from Section 4.5. Various beam currents (a) result in different saturation levels of the neutron flux (b). The ensembled $n = 5$ tearing mode activity also shows a reduced effect on the tearing mode reduction at lower beam current (c). q_{mag} (black) and q_f (red) with approximate island widths (d) sets the diffusive boundary at which fast-ion islands overlap. Modeling a diffusive region outside this radius and a gradient limited profile inside this radius leads to varied n_f profiles (e).

6. CONCLUSION

6.1 Summary

High concentrations of energetic particles in a magnetically confined device are limited by EPM activity. As an unavoidable consequence of increasing particle pressure, the stability threshold of the EPM represents the upper limit of fast-ion content. Alfvén eigenmodes are commonly observed, and an isotropic slowing distribution is likely to have resonant orbits for all kinds of modes, some of which may be avoided. Such avoidance simply allows the fast-ion population to grow until a critical gradient is reached at which point an EPM transports resonant particles and flattens the fast-ion profile.

To scientifically study the EPM and its stability limit, a set of plasma conditions were found where tearing mode and fast-ion orbit losses were controlled and a single (or multiple but non-overlapping) Alfvén waves were present. The lack of multiple active modes shows that the measurement made at marginal stability late in the 300 kA dataset represents a good measure of the EPM stability threshold.

This data represents the first fast-ion profiles measured in an RFP. Prior to this work, knowledge of the fast-ion profile was limited to predictions made by classical TRANSP calculations. These results were presumed valid only until the onset of EPM activity. The fast-ion distribution during mode activity is measured in this work by an improved neutron diagnostic suite. The chord-integrated CiNDe measurements normalized against the absolutely calibrated global neutron detectors provide the data necessary for inversion to a resulting density and beta profile. In order to assess the evolution of the profile as well as the driving mechanism for the EPMS, we compare profiles reconstructed early and late in the NBI discharge as well as between plasmas with differing $|B|$.

MST's 1 MW NBI sources fast-ions into the core where they exhibit nearly classical

confinement times. Interaction with the plasma broadens this profile somewhat in both pitch and radius, but a large core-localized high pitch population remains, creating the free-energy source to drive EPM activity. The destabilization threshold is determined by the strength of the EP drive, the continuum damping rate, and resonant orbit requirements. When the mode is destabilized, fast-ions resonantly interact with an Alfvén wave, losing energy in the process. The depletion of energy and interaction with the magnetic perturbation they helped create causes rapid nonlinear evolution of the fast-ion profile.

When operating with NBI in lower current discharges, MST routinely reaches marginally stable EPM states where the fast-ion source rate is matched by the periodic loss of fast-ions through EPM bursts. The results of this work show that marginal stability is reached in plasma conditions considered, at a critical gradient of $\nabla\beta_f = 0.5\%/cm$. The drive is sensitive to variations in the core-most tearing mode amplitude. At lower I_p neutral beam injection reduces the amplitude of the core-most mode, aiding in the development of a large peaked fast-ion profile in the core. The larger tearing mode amplitude at higher I_p pushes the fast-ion profile further out in radius increasing loss effects due to charge-exchange and fast-ion orbit stochasticity. The relatively flat fast-ion profile in the core reduces EPM drive, resulting in only weak mode activity.

6.2 Future Work

6.2.1 Fusion Proton Detector

The detection of fusion protons is in many ways the experimental complement to this research. The 3.01 MeV D-D fusion protons are only weakly influenced by MST's magnetic field and quickly exits the plasma in an almost straight line. It is therefore possible to map the fusion profile in MST by measuring fusion proton emission along multiple lines of sight. However, protons do not pass through the vacuum vessel like neutrons readily do but instead bombard the aluminum wall and emit a spectrum of high energy photons. It is therefore necessary for this diagnostic to use a vacuum port, adding difficulty to the task of gathering data from multiple viewing chords across the plasma.

A fusion proton detector has been developed at Tri Alpha Energy and tested both on

the C2-U device [63] and recently on MST as well. In both cases the detector, operating in pulse counting mode, was shown to be effective at gathering proton data. At the time of writing, however, the detector was awaiting the manufacture of a collimating aperture which will define a viewing volume similar in size to CiNDe.

A multi-diagnostic approach to measuring the fast-ion distribution in MST is therefore possible, with increased data collection rates, by utilizing both CiNDe and the proton detector. The proton detector also presents a means to calibrate CiNDe as the proton-neutron emission rates are effectively the same.

6.2.2 *Pulse Shape Discrimination*

CiNDe’s neutron detector system was designed to include the ability to pulse-shape discriminate MST’s large gamma background, which are detected nearly as readily as neutrons in a scintillator. A neutron is detected by recoiling off of a proton which then travels a short distance through the scintillator depositing its energy by exciting the molecules around it. A gamma enters the scintillator and ionizes a molecule releasing an electron which is then responsible for exciting the fluorescent molecules. Both interactions produce pulses of similar amplitude, making differentiation between radiation types difficult. Despite the similar number of photons emitted for each radiation type, there is a small difference in the temporal photon emission resulting in a difference in pulse shape.

Due to the impurity properties of the scintillator, neutron interactions excite the fluorescent molecule into a triplet state at a higher rate than do gamma interactions [64]. The triplet state has a longer mean decay time than the singlet state which gives a neutron pulse a stronger “delayed fluorescence” component than a gamma pulse, though both are still dominated by “prompt” decay fluorescence. CiNDe’s scintillator is a BC-501A liquid scintillator in a 15.25×3.81 cm diameter cylindrical MAB-1 cell aluminum housing from Saint-Gobain Crystals. The interior has a reflective coating with a window on one end for optical coupling to a PMT. The mean decay times for prompt and delayed fluorescence are 32.3 and 270 ns with peak emission at $\lambda=425$ nm. This couples well with the R580 Hamamatsu PMT which has a 2.7 ns anode pulse rise time and is the same type used for the NMF/NHF detectors. The PMT anode is then connected to a Thorlabs TIA60 transimpedance amplifier featuring

a 5.5 ns rise time and a gain of $3.02 \times 10^4 V/A$. The resulting voltage pulse is then digitized at 500 MHz. The digitizer has a sample size of 2^{24} resulting in a maximum data length of ~ 33.5 ms.

Despite the speed of the electronics involved, enough noise was present on the signal to make pulse shape discrimination ineffective. After much investigation, a measurable difference in pulse shape was observed after carefully averaging together sets of *known* gamma pulses from a ^{137}Cs source (averaging done between pulses and not in time) and comparing them to the gamma/neutron pulse mixture of NBI data. However, no method has been found capable of sorting the gamma/neutron pulse mixture by radiation type based on a pulse-by-pulse basis. Increased shielding against electrical noise and other noise reduction techniques must be employed to make use of this technique.

More effective data collection will be realized by reducing background signal through pulse shape discrimination

6.2.3 *NBI Fueling Mixture*

Given the same qualitative mode behavior with deuterium and hydrogen beam fuel and the importance of mode-particle resonance for EPM activity, it is interesting to wonder at the effects of using mixed fuel (perhaps 50/50 hydrogen and deuterium) in order to push the total fast-ion beta to even greater limits. The fast-ion q profiles for each species are shifted different amounts from magnetic q, potentially reducing the effect one species' EPM on another. It remains to be seen if a two-species neutral beam might be capable of exciting multiple EPMS due to strong yet distinct sources of energetic particle drive.

6.2.4 *Investigation of Mode Structure*

Little is known about the EPM structure. Here we used a simplified model and found it sufficient to predict resonance with the observed mode activity. In the future, measurements of the perturbed electric fields will allow for a more rigorous approach to this analysis and a more complete understanding of the mode-particle resonances within MST.

BIBLIOGRAPHY

- [1] U.S. Energy Information Administration [Database]. eia.gov (Accessed March 2016).
- [2] Benjamin F. Hudson. *Fast Ion Confinement in The Reversed-Field Pinch*. PhD thesis, University of Wisconsin-Madison, 2006.
- [3] D. Liu, A.F. Almagri, J.K. Anderson, V.V. Belykh, B.E. Chapman, V.I. Davydenko, P. Deichuli, D.J. Den Hartog, S. Eilerman, G. Fiksel, C.B. Forest, A.A. Ivanov, M.D. Nornberg, S.V. Polosatkin, J.S. Sarff, N. Stupishin, and J. Waksman. Fast ion confinement studies in the MST reversed field pinch. *38th EPS Conference on Plasma Physics*, pages 3–6, 2011.
- [4] R.K. Pachauri and L.A. Meyer. *IPCC, 2014: Climate Change 2014: Synthesis Report. Contribution of Working Groups I, II and III to the Fifth Assessment Report of the Intergovernmental Panel on Climate Change*. 2014.
- [5] P. Martin and M.E. Puiatti. Overview of the RFX-mod fusion science programme. *Nuclear Fusion*, 53:104018, 2013.
- [6] P R Brunsell, H Bergs aker, M Cecconello, J R Drake, R M Gravestijn, a Hedqvist, and J-a Malmberg. Initial results from the rebuilt EXTRAP T2R RFP device. *Plasma Physics and Controlled Fusion*, 43(11):1457–1470, 2001.
- [7] S. Masamune, A. Sanpei, R. Ikezoe, T. Onchi, K.I. Murata, K. Oki, H. Shimazu, T. Yamashita, and H. Himura. Characterization of initial low-aspect ratio RFP plasmas in RELAX. *Journal of the Physical Society of Japan*, 76(12):1–4, 2007.
- [8] W. Liu, W. Mao, H. Li, J. Xie, T. Lan, A. Liu, S. Wan, H. Wang, J. Zheng, X. Wen, H. Zhou, W. You, C. Li, W. Bai, C. Tu, M. Tan, B. Luo, C. Fu, F. Huang, B. Xiao, Z. Luo, B. Shen, P. Fu, L. Yang, Y. Song, Q. Yang, J. Zheng, H. Xu, P. Zhang, C. Xiao, and W. Ding. Progress of the Keda Torus eXperiment Project in China: design and mission. *Plasma Physics and Controlled Fusion*, 56(9):094009, 2014.
- [9] S. Eilerman, J.K. Anderson, J.A. Reusch, D. Liu, G. Fiksel, S. Polosatkin, and V. Belykh. Time-resolved ion energy distribution measurements using an advanced neutral particle analyzer on the MST reversed-field pinch. *Review of Scientific Instruments*, 83(10):10D302, oct 2012.
- [10] J.A. Reusch, J.K. Anderson, V. Belykh, S. Eilerman, D. Liu, G. Fiksel, and S. Polosatkin. Calibration of an advanced neutral particle analyzer for the Madison Symmetric Torus reversed-field pinch. *Review of Scientific Instruments*, 83(10):10D704, oct 2012.

- [11] M.M. Menon. Neutral beam heating applications and development. *Proceedings of the IEEE*, 69(8):1012–1029, 1981.
- [12] R.J. Goldston, D.C. McCune, H.H. Towner, S.L. Davis, R.J. Hawryluk, and G.L. Schmidt. New techniques for calculating heat and particle source rates due to neutral beam injection in axisymmetric tokamaks. *Journal of Computational Physics*, 43(1):61–78, sep 1981.
- [13] W.W. Heidbrink. Basic physics of Alfvén instabilities driven by energetic particles in toroidally confined plasmas. *Physics of Plasmas*, 15(5):055501, 2008.
- [14] G.-Y. Fu and J. W. Van Dam. Excitation of the toroidicity-induced shear Alfvén eigenmode by fusion alpha particles in an ignited tokamak, 1989.
- [15] K. McGuire and R. Goldston. Study of high-beta magnetohydrodynamic modes and fast-ion losses in PDX. *Physical Review Letters*, 50(12):891–895, 1983.
- [16] R.B. White. Theory of mode-induced beam particle loss in tokamaks. *Physics of Fluids*, 26(10):2958–2965, 1983.
- [17] L. Chen, R.B. White, and M.N. Rosenbluth. Excitation of internal kink modes by trapped energetic beam ions. *Physical Review Letters*, 52(13):1122–1125, 1984.
- [18] W.W. Heidbrink, K. Bol, D. Buchenauer, R. Fonck, G. Gammel, K. Ida, R. Kaita, S. Kaye, H. Kugel, B. LeBlanc, W. Morris, M. Okabayashi, E. Powell, S. Sesnic, and H. Takahashi. Tangential neutral-beam-driven instabilities in the Princeton Beta Experiment. *Physical Review Letters*, 57(7):835–838, 1986.
- [19] L. Chen. Theory of magnetohydrodynamic instabilities excited by energetic particles in tokamaks. *Physics of Plasmas*, 1(5):1519, 1994.
- [20] S Briguglio, C Kar, F Romanelli, G Vlad, and F Zonca. Linear and nonlinear evolution of alpha-particle driven gap modes. *Plasma Physics and Controlled Fusion*, 37(11A):A279–A290, 1995.
- [21] R.A. Santoro and L. Chen. Gyrokinetic-magnetohydrodynamic hybrid simulation of the transition from toroidal Alfvén eigenmodes to kinetic ballooning modes in tokamaks. *Physics of Plasmas*, 3(6):2349, 1996.
- [22] C.Z. Cheng, N.N. Gorelenkov, and C.T. Hsu. Fast Particle Destabilization of TAE Modes. *Nuclear Fusion*, 35(12):1–28, 1995.
- [23] W.W. Heidbrink. Beam-driven chirping instability in DIII-D. *Plasma Physics and Controlled Fusion*, 37(9):937–949, 1995.
- [24] F. Zonca and L. Chen. Destabilization of energetic particle modes by localized particle sources. *Physics of Plasmas*, 7(11):4600–4608, 2000.

- [25] K. Shinohara, Y. Kusama, M. Takechi, A. Morioka, M. Ishikawa, N. Oyama, K. Tobita, T. Ozeki, S. Takeji, S. Moriyama, T. Fujita, T. Oikawa, T. Suzuki, T. Nishitani, T. Kondoh, S. Lee, M. Kuriyama, G.J. Kramer, N.N. Gorelenkov, R. Nazikian, C.Z. Cheng, and G.Y. Fu. Alfvén eigenmodes driven by Alfvénic beam ions in JT-60U. *Nuclear Fusion*, 41(5):603–612, 2001.
- [26] Y. Kusama, G.J. Kramer, H. Kimura, M. Saigusa, T. Ozeki, K. Tobita, T. Oikawa, K. Shinohara, T. Kondoh, M. Moriyama, F.V. Tchernychev, M. Nemoto, A. Morioka, M. Iwase, N. Isei, T. Fujita, S. Takeji, M. Kuriyama, R. Nazikian, G.Y. Fu, K.W. Hill, and C.Z. Cheng. Characteristics of Alfvén eigenmodes, burst modes and chirping modes in the Alfvén frequency range driven by negative ion based neutral beam injection in JT-60U. *Nuclear Fusion*, 39(11Y):1837–1843, 2002.
- [27] A. Weller, M. Anton, J. Geiger, M. Hirsch, R. Jaenicke, A. Werner, C. Nuhrenberg, E. Sallander, and D.A. Spong. Survey of magnetohydrodynamic instabilities in the advanced stellarator Wendelstein 7-AS. *Physics of Plasmas*, 8(3):931, 2001.
- [28] E. Fredrickson, L. Chen, and R. White. Bounce precession fishbones in the national spherical torus experiment. *Nuclear Fusion*, 43(10):1258–1264, 2003.
- [29] E.D. Fredrickson, R.E. Bell, D.S. Darrow, G.Y. Fu, N.N. Gorelenkov, B.P. LeBlanc, S.S. Medley, J.E. Menard, H. Park, A.L. Roquemore, W.W. Heidbrink, S.A. Sabbagh, D. Stutman, K. Tritz, N.A. Crocker, S. Kubota, W. Peebles, K.C. Lee, and F.M. Levinton. Collective fast ion instability-induced losses in National Spherical Tokamak Experiment. *Physics of Plasmas*, 13(5):0–9, 2006.
- [30] G.J. Kramer. Suppressing Alfvén eigenmodes by q-profile engineering to improve fast-ion confinement. In *APS-DPP*, 2016.
- [31] K. Wong, R. Fonck, S. Paul, D. Roberts, E. Fredrickson, R. Nazikian, H. Park, M. Bell, N. Bretz, R. Budny, S. Cohen, G. Hammett, F. Jobs, D. Meade, S. Medley, D. Mueller, Y. Nagayama, D. Owens, and E. Synakowski. Excitation of toroidal Alfvén eigenmodes in TFTR. *Physical Review Letters*, 66(14):1874–1877, 1991.
- [32] W.W. Heidbrink, E.J. Strait, E. Doyle, G. Sager, and R.T. Snider. An investigation of beam driven Alfvén instabilities in the DIII-D tokamak. *Nuclear Fusion*, 31(9):1635–1648, 2011.
- [33] E.J. Strait, W.W. Heidbrink, A.D. Turnbull, M.S. Chu, and H.H. Duong. Stability of neutral beam driven TAE modes in DIII-D. *Nuclear Fusion*, 33(12):1849–1870, 1993.
- [34] W.W. Heidbrink, E.J. Strait, M.S. Chu, and A.D. Turnbull. Observation of beta-induced Alfvén eigenmodes in the DIII-D tokamak. *Physical Review Letters*, 71(6):855–858, 1993.
- [35] H.L. Berk, B.N. Breizman, and H. Ye. Scenarios for the nonlinear evolution of alpha-particle-induced Alfvén wave instability. *Physical Review Letters*, 68(24):3563–3566, 1992.

- [36] G. Regnoli, H. Bergsaker, E. Tennfors, F. Zonca, E. Martines, G. Serianni, M. Spolaore, N. Vianello, M. Cecconello, V. Antoni, R. Cavazzana, and J.A. Malmberg. Observations of toroidicity-induced Alfvén eigenmodes in a reversed field pinch plasma. *Physics of Plasmas*, 12(4):1–10, 2005.
- [37] S. Spagnolo, M. Zuin, F. Auriemma, R. Cavazzana, E. Martines, M. Spolaore, and N. Vianello. Alfvén eigenmodes in the RFX-mod reversed-field pinch plasma. *Nuclear Fusion*, 51(8):083038, 2011.
- [38] J.J. Koliner, C.B. Forest, J.S. Sarff, J.K. Anderson, D. Liu, M.D. Nornberg, J. Waksman, L. Lin, D.L. Brower, W.X. Ding, and D.A. Spong. Fast-particle-driven Alfvénic modes in a reversed field pinch. *Physical Review Letters*, 109(11):1–5, 2012.
- [39] A. Biancalani, L. Chen, F. Pegoraro, and F. Zonca. Continuous spectrum of shear Alfvén waves within magnetic islands. *Physical Review Letters*, 105(9):1–4, 2010.
- [40] C.R. Cook, C.C. Hegna, J.K. Anderson, K.J. McCollam, J. Boguski, R. Feng, J.J. Koliner, D.A. Spong, and S.P. Hirshman. Identification of island-induced Alfvén eigenmodes in a reversed field pinch. *Plasma Physics and Controlled Fusion*, 58(5):054004, 2016.
- [41] C.R. Cook. *Shear Alfvén Continua and Discrete Modes in the Presence of a Magnetic Island*. PhD thesis, University of Wisconsin-Madison, 2015.
- [42] W.W. Heidbrink, Jinchoon Kim, and R.J. Groebner. Comparison of experimental and theoretical fast ion slowing-down times in DIII-D. *Nuclear Fusion*, 28(10):1897–1901, 1988.
- [43] H.-S. Bosch and G.M. Hale. Improved formulas for fusion cross-sections and thermal reactivities. *Nuclear Fusion*, 33(12):1919–1919, 2002.
- [44] R.M. Magee. *Ion energization during tearing mode magnetic reconnection in a high temperature plasma*. PhD thesis, University of Wisconsin-Madison, 2011.
- [45] C.L. Fink, D.L. Smith, B.J. Micklich, and T.N. Massey. Gamma rays produced by 1.75- to 4-MeV proton bombardment of thick aluminum targets. *Nuclear Instruments and Methods in Physics Research Section A: Accelerators, Spectrometers, Detectors and Associated Equipment*, 505(1-2):5–8, 2003.
- [46] T.W. Crane and M.P. Baker. Neutron Detectors. In *Passive Nondestructive Assay of Nuclear Materials*, chapter 13, pages 379–406. 1991.
- [47] Los Alamos Scientific Laboratory (1979). MCNP: a general Monte Carlo code for neutron and photon transport. Los Alamos, N.M.: [Springfield, Va.]:Dept. of Energy, Los Alamos Scientific Laboratory; [for sale by the National Technical Information Service].
- [48] Evaluated Nuclear Data File (ENDF) [Database]. <https://www-nds.iaea.org/exfor/endl.htm> (Accessed June 2016).

- [49] P. Rinard. Neutron interactions with matter. *Passive Nondestructive Assay of Nuclear Materials*, 1991.
- [50] F. Scholkmann, J. Boss, and M. Wolf. An Efficient Algorithm for Automatic Peak Detection in Noisy Periodic and Quasi-Periodic Signals. *Algorithms*, 5(4):588–603, 2012.
- [51] G. Fiksel, B.F. Hudson, D.J. Den Hartog, R.M. Magee, R. O’Connell, S.C. Prager, A.D. Beklemishev, V.I. Davydenko, A.A. Ivanov, and Y.A. Tsidulko. Observation of weak impact of a stochastic magnetic field on fast-ion confinement. *Physical Review Letters*, 95(12):125001, sep 2005.
- [52] T. M. Biewer, C. B. Forest, J. K. Anderson, G. Fiksel, B. F. Hudson, S. C. Prager, J. S. Sarff, J. C. Wright, D. L. Brower, W. X. Ding, and S. D. Terry. Electron heat transport measured in a stochastic magnetic field. *Physical review letters*, 91(4):045004, 2003.
- [53] B.E. Chapman, A.F. Almagri, J.K. Anderson, T.M. Biewer, P.K. Chattopadhyay, C.S. Chiang, D. Craig, D.J. Den Hartog, G. Fiksel, C.B. Forest, A.K. Hansen, D. Holly, N.E. Lanier, R. O’Connell, S.C. Prager, J.C. Reardon, J.S. Sarff, M.D. Wyman, D.L. Brower, W.X. Ding, Y. Jiang, S.D. Terry, P. Franz, L. Marrelli, and P. Martin. High confinement plasmas in the Madison Symmetric Torus reversed-field pinch. *Physics of Plasmas*, 9(5):2061–2068, 2002.
- [54] J. Egedal. Drift orbit topology of fast ions in tokamaks. *Nuclear Fusion*, 40(9):1597, 2000.
- [55] J.L. Clark. Fast Ion Orbit Topology in the Reversed-Field Pinch. In *55th Annual Meeting of the APS Division of Plasma Physics*, 2013.
- [56] L. Marrelli, P. Martin, G. Spizzo, P. Franz, B.E. Chapman, D. Craig, J.S. Sarff, T.M. Biewer, S.C. Prager, and J.C. Reardon. Quasi-single helicity spectra in the Madison Symmetric Torus. *Physics of Plasmas*, 9(7):2868, 2002.
- [57] J.K. Anderson, W.J. Capecchi, S. Eilerman, J.J. Koliner, M.D. Nornberg, J.A. Reusch, J.S. Sarff, and L. Lin. Fast ion confinement in the three-dimensional helical reversed-field pinch. *Plasma Physics and Controlled Fusion*, 56(9):094006, sep 2014.
- [58] C.B. Markwardt (2002). DDEABM [Computer program]. Available at <http://cow.physics.wisc.edu/~craigm/idl/down/ddeabm.txt> (Accessed 20 October 2013).
- [59] F. Porcelli, R. Stankiewicz, W. Kerner, and H.L. Berk. Solution of the drift-kinetic equation for global plasma modes and finite particle orbit widths. *Physics of Plasmas*, 1(3):470, 1994.
- [60] J.T. Chapman. *Spectroscopic Measurement of the Mhd Dynamo*. PhD thesis, University of Wisconsin-Madison, 1998.

- [61] L. Lin, J.K. Anderson, D.L. Brower, W.J. Capecchi, W.X. Ding, S. Eilerman, C.B. Forest, J.J. Kollner, D. Liu, M.D. Nornberg, J.A. Reusch, and J.S. Sarff. Energetic-particle-driven instabilities and induced fast-ion transport in a reversed field pinch. *Physics of Plasmas*, 21(5):056104, may 2014.
- [62] L. Lin, W.X. Ding, D.L. Brower, J.J. Kollner, S. Eilerman, J.A. Reusch, J.K. Anderson, M.D. Nornberg, J.S. Sarff, J. Waksman, and D. Liu. Measurement of energetic-particle-driven core magnetic fluctuations and induced fast-ion transport. *Physics of Plasmas*, 20(3):030701, 2013.
- [63] R.M. Magee, R. Clary, S. Korepanov, A. Smirnov, E. Garate, K. Knapp, and A. Tkachev. Fusion proton diagnostic for the C-2 field reversed configuration. *Review of Scientific Instruments*, 85(11):11D851, 2014.
- [64] N. Zaitseva, A. Glenn, L. Carman, R. Hatarik, S. Hamel, M. Faust, B. Schabes, N. Cherepy, S. Payne, A. Glenn, R. Hatarik, S. Hamel, B. Rupert, M. Faust, B. Schabes, N. Cherepy, and S. Payne. Pulse shape discrimination in impure and mixed single-crystal organic scintillators. *IEEE Transactions on Nuclear Science*, 58(6 PART 2):3411–3420, 2011.

APPENDIX:
NEUTRON BALL CALIBRATION OF GLOBAL NEUTRON
DETECTORS

In order to determine the ASP2(e)/NRD BF_3 “neutron ball” calibration (counts/ μrem) it is placed in a 20 mRem/hr neutron field from a $^{238}\text{Pu-Be}$ source. Pulses are continuously counted until a statistically significant total is achieved. The resulting count rate is then compared to the dose rate input to determine the calibration constant. The device is then tested in various neutron field strengths to ensure linearity and tested with a ^{137}Cs source to ensure gamma rejection. For every pulse registered in the gas-filled detector the dose readout increases by $0.552 \mu\text{rem}$. This is significant since in normal MST operation or while using mixed fuel NBI, the neutron ball routinely measures $\leq 10 \mu\text{rem}$ for each discharge, meaning < 20 pulses were registered. Operating at such a low count rate demands ensembling over many similar discharges.

There are several key assumptions that affect the veracity of the cross-calibration of the detectors. The neutron ball was calibrated in a 20 mRem/hr neutron field, and because neutron cross sections change rapidly with energy it is worthwhile to consider the differences between the neutron fields produced by the calibration source and that of MST. A $^{238}\text{Pu-Be}$ source has an average neutron energy around 4.5 MeV, but has a very broad spectrum whereas MST presents an almost monoenergetic field of 2.45 MeV neutrons. While the dose scales linearly with energy, the detector itself responds differently to neutrons of varying energies. In fact, due to higher energy neutrons having both a lower probability of slowing on the polyethylene shielding and a lower detection efficiency in the gas-filled detector, the neutron ball would actually register a *lower* dose in a 14.1 MeV (D-T fusion) neutron field than in a 2.45 MeV (D-D fusion) field of the same neutron rate. For complete accuracy, the

actual energy distribution of the neutrons would need to be considered. Neutrons from MST are near the average energy of the calibration source, however, and calibration proceeds under the assumption that 2.45 MeV neutrons are representative of the $^{238}\text{Pu-Be}$ calibration neutrons.

The measure of radiation imparted to tissue is a measure of energy deposited per mass, commonly given in units of rads (*radiation absorbed dose*). Although the rad is a measure of a real physical quantity, the unit rem (*roentgen equivalent man*) was designed in an attempt to quantify the variable amount of biological damage done by different types of ionizing radiation. Although there is no universal conversion from rad to rem, they can be simply related through the relation $rem = rad \times Q$, where the value of Q is chosen based upon how damaging the radiation. Gamma rays, for example, are given a Q value of 1 whereas alpha particles have a Q of 20. Neutrons fall in between depending on their energy, with $Q = 10$ an appropriate choice for MST's neutron radiation. A 2.45 MeV neutron can now be converted into a dose in a straightforward way

$$1\text{neutron} = 2.45\text{ MeV} \times \frac{1\text{ rad}}{100 \frac{\text{erg}}{\text{g}}} \times 10 \frac{\text{rem}}{\text{rad}} \times \frac{1}{80\text{ kg}} \times \frac{1.602 \times 10^{-6}\text{ erg}}{\text{MeV}} \quad (.1)$$

$$1\ \mu\text{rem} = 2.04 \times 10^5\ \text{neutrons} \quad (.2)$$

where a mass of 80 kg was assumed for an average person. It is worthwhile to point out that with a calibration of $0.552\ \mu\text{rem}/\text{count}$, for each count made by the neutron ball it is “recording” around 10^5 neutrons. This absolutely calibrated total neutron count can be compared to the time integral of our fast flux detector signals over a wide range of total fluxes by varying NBI and plasma parameters.

A fit to the unsaturated data yields a scaling of $7.96\ \text{mVs}/\mu\text{rem}$. NMF and NHF show good linearity over the entire range of flux levels achievable in MST and yield scalings of $1.53\ \text{mVs}/\mu\text{rem}$ and $1.12\ \text{mVs}/\mu\text{rem}$ respectively. Utilizing the conversion factor from Eq. .2

we can then compute a calibration for each detector using

$$cf_{detector} = 2.04 \times 10^5 \frac{neutrons}{\mu rem} \times \frac{1}{dose\ scaling} \times \frac{1}{gf} \quad (.3)$$

where the dose scaling is that found from the neutron ball comparison, and where gf is the geometric factor giving the total fraction of neutron emission absorbed by the worker at the detector location, estimated to be the area of the worker divided by the surface area of MST times the attenuation factor due to the detector location, $gf = \frac{1}{30}0.3$ [44].